UCLouvain

École polytechnique de Louvain

Towards dynamic modelling of micro gas turbines

Model development and calibration to the Turbec T100

Author: **Antoine Laterre**
Supervisor: **Francesco Contino**
Readers: **Tony Arts, Aggelos Gaitanis**
Academic year 2020–2021
Master [120] in Electro-mechanical Engineering

ABSTRACT

Our energy system is shifting from conventional and centralised power generation to a more distributed and renewable architecture. To balance the intermittences involved with the transition to renewable energy sources, small-scale combined heat and power (CHP) units are expected to play an important role. Micro gas turbines (mGTs), which are generally considered as gas turbines with a power output smaller than $500kW$, are a promising technology for such application and present numerous advantages over their main competitor, the internal combustion engine (ICE). Some of their main assets are the low emissions levels, low maintenance requirements and high fuel flexibility. These have enabled them to attract a great deal of interest over the last two decades. The application of mGTs as compensators for intermittency forces them to satisfy transient and part-load flexible operations. Therefore, a full characterization of their dynamic behavior is required for the development of suited and efficient control systems. For that aim, the present Thesis proposes the complete development, from scratch, of a modular and flexible numerical tool, implemented in the `Python` open-source programming language, to simulate transients in mGTs. The model is calibrated with experimental results issued from the VUB Turbec T100 test rig and with additional data published in the literature. A first attempt of control system implementation is also achieved. The compressor, recuperator, turbine and shaft models are successfully validated. Key assets of this tool are the accurate model established for the turbomachinery performance maps, which highlighted a discordance between the manufacturer compressor map and its actual performances, and the low complexity highly efficient recuperator model, which perfectly reproduces the experimental results measured during transient maneuvers.

ACKNOWLEDGEMENTS

First of all, I would like to thank the supervising team who gave me the opportunity to work on the topic of micro gas turbines and who gave me their trust throughout this year.

Thanks to my supervisor, Prof. Francesco Contino, for the introduction to this subject and to the formalism of the research world, as well as for the advice given to my scientific communication.

I would also like to express my warm thanks to Aggelos Gaitanis, PhD candidate at the Thermodynamics and Fluid mechanics Laboratory (TFL) of the Institute of Mechanics, Materials and Civil Engineering (iMMC) at Université catholique de Louvain (UCLouvain), for all the time devoted to the supervision of my work. His advice was invaluable and I hope that our collaboration will have enriched his research.

I would also like to thank Prof. Tony Arts from the von Karman Institute for taking time out of his busy schedule to read and evaluate this thesis.

I would like to thank Prof. Ward De Paepe and the research team of Vrije Universiteit Brussel (VUB) for sharing with me the experimental results obtained on their test bench and their knowledge of micro gas turbines. The latter were invaluable for the validation of my model.

I would then like to express my sincere thanks to my family and friends for the encouragement I received during this project.

Thanks also to my dear mother and father for proofreading a document that is not always easy to digest for scientists of the living world. Your experience and advice helped me to better understand certain issues and to structure my communication more effectively. I hope that through this manuscript, you have been able to better understand how I have occupied my days and "blocus" for five years, even if you were already aware of a good part of my extracurricular activities. I hope you are proud of your achievement as parents.

I would also like to express my gratitude to my partner Noémie, for the unconditional support she offered me, for all her encouragement, as well as for the passive incitement via her previous achievements to challenge and to surpass myself. Thank you also for reviewing this manuscript with such care.

Finally, I would like to thank Mr. Carlo Cordaro, whom I was lucky enough to have as a high school maths teacher for three years and who passed on to me a real passion for maths and science. I could not finish my engineering studies without expressing my sincere thanks to him.

CONTENTS

Appendices

LIST OF FIGURES

LIST OF TABLES

NOMENCLATURE

Symbols

Δt	Numerical time step	$[s]$
δ_{rel}	Relative deviation/error	$[\%]$
$\dot{m}$	Mass flow rate	$[kg/s]$
ϵ	Effectiveness	$[-]$
η	Efficiency	$[-]$
ω	Angular velocity	$[rad/s]$
ϕ	Fuel/Air equivalence ratio	$[-]$
π	Pressure ratio	$[-]$
τ_{min}	Smallest characteristic time	$[s]$
A	Heat transfer area	$[m^2]$
C	Heat capacity rate	$[W/K]$
c	Velocity	$[m/s]$
C_r	Heat capacity ratio	$[-]$
c_w	Wall specific heat capacity	$[J/kgK]$
D_h	Hydraulic diameter	$[m]$
f	Fuel/Air ratio	$[-]$
h	Convective heat transfer coefficient	$[W/m^2K]$
h	Specific enthalpy	$[J/kg]$
I	Moment of inertia	$[kgm^2]$
k	Conductive heat transfer coefficient	$[W/mK]$
M	Mach number	$[-]$

m_w	Wall mass	$[kg]$
MM	Molar mass	$[kg/mol]$
N	Rotating speed	$[rpm]$
P	Power	$[W]$
p	Pressure	$[Pa]$
R^*	Specific gas constant	$[J/kgK]$
t_w	Wall thickness	$[m]$
U	Overall heat transfer coefficient	$[W/m^2K]$
u	Specific energy	$[J/kg]$

Sub- and superscripts

$*$	Total conditions
0	Atmospheric conditions
c	Cold
c	Compressor
cor	Corrected
e	Electric
h	Hot
is	Isentropic
min	Minimum
$norm$	Normalized
$pred$	Predicted
red	Reduced
$s.l.$	Surge limit
$samp$	Sampled
t	Turbine
th	Thermal

Abbreviations

NTU	Number of Transfer Units
TIT	Turbine Inlet Temperature
TOT	Turbine Outlet Temperature

ANN	Artificial Neural Networks
CFD	Computational Fluid Dynamics
CHP	Combined Heat and Power
DAE	Differential Algebraic Equation
EFmGT	Externally Fired micro Gas Turbine
EGR	Exhaust Gas Recirculation
ER	Expansion Ratio
FLOX	FLameless OXidation
GA	Genetic Algorithms
GT	Gas Turbine
HAT	Humid Air Turbine
HEX	Heat EXchanger
ICE	Internal Combustion Engine
IGV	Inlet Guide Vanes
iMMC	Institute of Mechanics, Materials and Civil Engineering
LHV	Lower Heating Value
mGT	micro Gas Turbine
mHAT	micro Humid Air Turbine
NARMAX	Non-linear Auto-Regressive Moving Average with eXogeneous input
RMSE	Root Mean Square Error
SI	International System of Units
SM	Surge Margin
SOFC/mGT	Solid Oxide fuel Cell micro Gas Turbine
syngas	Synthetic Gas
TFL	Thermodynamics and Fluid mechanics Laboratory
UCLouvain	Université catholique de Louvain
ULB	Université libre de Bruxelles
ULiège	Université de Liège
VUB	Vrije Universiteit Brussel

INTRODUCTION

For several years now, our energy system has started to undergo architectural modifications to shift from conventional and centralised power generation to a more distributed and renewable system [1, 2]. This reorganization is perceived by the research world as a required pathway to sustain an in depth penetration of intermittent energy sources, like wind and solar [3, 4].

During the transition period, fossil but programmable energy sources will balance the intermintences involved with the transition to renewable [1]. Therefore, the strive for a rational and highly efficient use of fossil energies will remain a key target to limit greenhouse gas and pollutant emissions [5]. In this context, small-scale and flexible combined generation of heat and power (CHP), achieving overall efficiency above 90%, is expected to play an important role [6].

Initially developed by the automotive industry in the late 1980s, and then picked-up for small-scale CHP applications [7,8], micro-gas turbines (mGT), which are generally considered as gas turbines (GT) with a power output lower than $500kW$ [9, 10], were expected to support the deployment of distributed generation power plants [11]. Indeed, their low emission levels, low maintenance costs and low vibration level make them serious candidates for such application [12].

However, after more than 20 years of existence now, mGTs have still not managed to fully embrace the CHP market opportunities, which are still largely dominated by their main competitor, the internal combustion engine (ICE) [2, 13]. This is mainly explained by their lower electrical efficiency ($\simeq$ 30% for mGTs, $\geq$ 35% for ICEs), which is a severe drawback that makes them non-profitable in periods of low heat demand, leading to eventual machine shutdowns [13, 14].

Nevertheless, with the increasingly more restrictive emission policies, and with the emergence of alternative fuels, such as biomass-derived and electro-fuels, mGTs have regained in interests. While ICEs remain limited by their high pollutant emissions and low fuel flexibility [2], mGTs show a promising development potential to handle the combustion of a wide range of fuels (i.e. solid, liquid and gaseous) with low emissions [4, 15]. Their application in new cycles, with an improved efficiency, like humid air cycles and closed Brayton cycles for solar applications, or in hybrid systems with solid oxide fuel cells, has also been of growing interest for the past 15 years [5, 6, 16].

Applications in novel cycles and with alternative fuelling significantly modify the system dynamics [5, 13]. Therefore, the development of a new competitive generation of mGTs, allowing for both load and fuelling increased flexibility, will require numerical simulations in order to study their transient behavior and develop suited control systems.

The present Thesis is part this framework. Its end goal is to develop a modular and flexible tool from scratch, implemented in the `Python` open-source programming language, to simulate transients in mGTs with different possible cycles layouts. The modularity requirement intends to allow for the application of some blocks in other contexts. This tool will also be calibrated to represent the Turbec T100 mGT and it will be validated against experimental results, which were provided by researchers from Vrije Universiteit Brussel (VUB).

Thesis scope and structure

Two doctoral projects related to mGTs started in 2020 at UCLouvain, and several Master Theses in this field will be launched in the forthcoming months. For this reason, the present document has been written with the strong motivation to serve as a baseline for future works and it is intended to be used as a roadbook for the continuity of dynamic models development in our research team.

This Thesis is structured as follows:

- **Chapter 1 - State of the art** proposes an in-depth review about the micro gas turbines technology. The background of its historical development is first introduced and some of the improvements towards the new generation of mGTs are then presented. Thereafter, the specifications of the Turbec T100 mGT system, which is used as a reference machine in this work, are provided. After, different modelling approaches for transient analyses are presented. Finally, the current works in our research team are briefly introduced.
- **Chapter 2 - Performance maps modelling** focuses on the modelling of the compressor and turbine performance maps. Fundamentals of performance maps are first introduced. Then, the common practices in performance maps modelling are reviewed. In the last part, a model is constructed to represent the T100 performance maps.
- **Chapter 3 - Physical model** develops the complete physical model that has been constructed during this work to represent the mGTs dynamic behavior. The methodology is first thoroughly discussed and each mGT component model, representing the mGT dominant phenomena, is then presented with a block approach. The global mGT model is finally summarized with a graphical illustration and with the mathematical formulation of the system of equations.
- **Chapter 4 - Numerical model** introduces the numerical environment that has been constructed in the `Python` programming language, and briefly discusses the numerical performances of the simulation tool.
- **Chapter 5 - Calibration, simulation results and discussion** first proposes a complete model calibration to represent the Turbec T100. Most of the constructed blocks are validated. Given that a dynamic model is first and foremost an off-design model, Chapter 5 then presents the steady state results obtained with the numerical tool for four different part load operating points, and discusses the deviations compared to experiments. Some dynamic results, illustrating the model sensibility, are then introduced. A comparison, showing the agreement in dynamic behavior between experiments and simulations, is also proposed. The discussions, model assets and shortcomings, as well as the suggested future improvements, are finally gathered in a clear high-level summary.

A final **Conclusion** summarizes the main findings of this work and addresses the future perspectives.

CHAPTER 1

STATE OF THE ART

This Chapter aims at briefly summarizing the past and current research conducted in the field of micro gas turbines and of dynamic models developed in this context. In the first place, Section 1.1 introduces the historical background and the emergence of micro gas turbines. The new challenges faced by this technology are also addressed and the current research in this field is presented. Thereafter, in Section 1.2, the Turbec T100, which is used as a reference machine in this work, is described in further details. Section 1.3 then reviews the different modelling approaches used in both static and dynamic models. Finally, current works conducted by the UCLouvain research team are summarized in Section 1.4.

1.1 Micro gas turbines

As it has been mentioned in the Introduction, micro gas turbines (mGTs) are small devices converting fuel (e.g. natural gas) into mechanical energy, which drives an electrical generator through a single shaft assembly. Nowadays, although no formal terminology exists, two criteria are usually required to qualify a gas turbine (GT) as "micro": (1) the electrical power output of the machine must range between 15 and $300kW_e$ [17] (often extended up to $500kW_e$ [3,9,10]) and (2) the machine needs to run at high rotational speed (i.e. between $50,000$ and $120,000rpm$ [18]). Nevertheless, earlier in the development of mGTs, some authors like Pilavachi [19] proposed a dissociation between the micro turbines ($< 150kW_e$) and the mini turbines ($< 1MW_e$). Pratt & Whitney had already followed this guideline when they qualified their $400kW$ unit as "mini turbine" [7]. Let us also precise that the second criterion used for the terminology is of minor importance compared to the nominal power requirement.

According to Duan et *al.* [18], mGTs appeared in the 1940s in multi-shaft configurations and with heavy gear boxes. Until the late 1980s, their application was essentially in aero-engines because of their high power to weight ratio, extreme reliability and low maintenance. Some of their derivatives are still used in other domains, such as in pipeline compressors, ships propulsion and electric utility generators. Nevertheless, the use of mGTs in electricity production had remained limited, despite their ultra-low emission levels. This could largely be attributed to their low efficiency (about 14%) compared to reciprocating engines (about $35 - 40\%$) [7,11].

The development of modern mGTs was initiated at the end of the 1980s by the automotive industry, interested in alternatives to reciprocating diesel and gasoline engines (internal combustion engines, ICE). This was driven by their advantages in terms of emissions and fuel flexibility compared to ICE [8].

With the emergence of high compactness and high effectiveness regenerators (compact heat exchangers, HEX, also named recuperators), accompanied by the development of high-speed pneumatic bearings, high-speed permanent magnet generators and power electronics conversion technologies, modern advanced mGT began a rapid development starting from the 1990s [18]. At this time, hybrid technologies for the incorporation of mGTs inside vehicles were not sufficiently mature and the technology was instead picked up for the decentralised power generation market [8]. *NoMac Energy* (nowadays the *Capstone Turbine Corporation*) was one of the pioneer is this domain [7].

Some of the main mGTs market actors and the basic information about their products are reported in Table 1.1. *Capstone*, *Ingersoll-Rand* and *Elliott* are established in the USA. *Bowman* and *Turbec* are established in the UK and Italy respectively [2]. *Mitis* is a Belgian spin-off of Université de Liège (ULiège) and of Université libre de Bruxelles (ULB), which develops, manufactures and sells micro-CHP (Combined Heat and Power) systems based on mGTs using flameless combustor [20].

Manufacturer	**Model**	**P [kWe]**	**N [rpm]**	**Eff. [%]**	**Ref.**
Bowman Power Systems	TG-45	45	$105,000$	22.2	[21]
Bowman Power Systems	TG-80RC	80	$68,000$	$27-28$	[2,7]
Capstone Turbine Corporation	C-30	30	$96,000$	26	[7,22]
Capstone Turbine Corporation	C-60	60	$85,000$	28	[2,7]
Elliott Energy Systems	TA-80R	80	$68,000$	28	[15]
Elliott Energy Systems	TA-100	105	$68,000$	29	[7]
Ingersoll-Rand Power Works	IR-70SM	70	$44,000$	28	[7]
Ingersoll-Rand Power Works	IR-250SM	250	/	31	[7]
Toyota Turbine Systems	TTS-50	50	/	/	[7]
Toyota Turbine Systems	TTS-300	350	/	/	[7]
Turbec AB	T100	100	$70,000$	30	[23]
Mitis (ULiège/ULB spin-off)	μ10	10	/	23	[20]

Table 1.1: Main actors of modern mGTs market and basic information on their products.

1.1.1 The thermodynamic cycle

Modern mGT systems, utilized in decentralized power generation, typically exploit recuperated Brayton cycles. In these cycles, represented in Fig. 1.1, fresh ambient air first undergoes a compression through a single-stage centrifugal compressor [24]. The compression ratio is usually low (i.e. approximately $3-5$ [2]) because of the single stage layout. Then, the compressed air is preheated before entering the combustion chamber thanks to a recuperator that recovers the heat from the exhaust gas. The recuperator is a key element of the mGT since it commonly almost doubles the efficiency compared to a simple Brayton cycle configuration [2]. Inside a lean pre-mix combustion chamber [25], the preheated compressed air is mixed with a fuel (normally in gaseous form). The highly diluted mixture (i.e. fuel/air ratio $f < 0.01$ for rich natural gas, corresponding to a fuel/air equivalence ratio $\phi < 0.15$ [26]) is ignited, and the generated flue gas leaves the combustion chamber at high temperature. However, the turbine inlet temperature (TIT) is far lower compared to large gas turbines (i.e. usually below 950^oC [2]) because cooling requirements (e.g. blade cooling) are both economically and technically difficult to achieve at the mGT scale [24]. The flue gas is thereafter expanded through a radial turbine. The temperature drop after expansion is generally not superior to 300^oC and the turbine outlet temperature (TOT) is usually limited to maximum 650^oC, in order to protect the recuperator.

The expanded gas finally crosses the recuperator hot leg to achieve the waste heat recovery. The exhaust gas temperature lies between 250^oC and 300^oC [2].

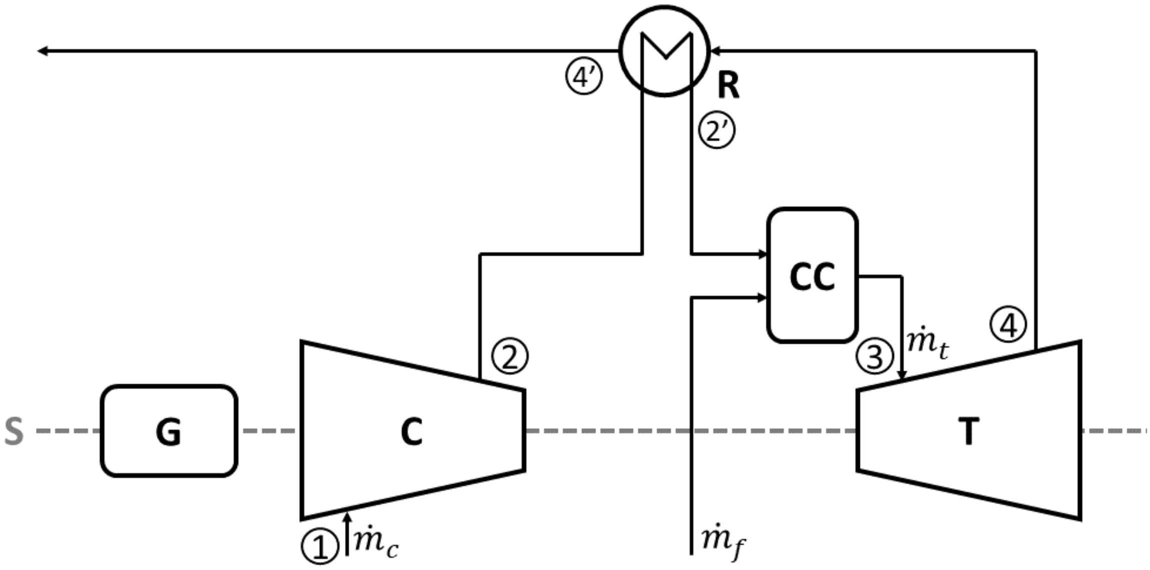

Figure 1.1: Recuperated Brayton cycle configuration. Index system: 1 = compressor (**C**) inlet, 2 = compressor outlet/recuperator (**R**) cold leg inlet, 2′ = recuperator cold leg outlet/combustion chamber (**CC**) inlet, 3 = combustion chamber outlet/turbine (**T**) inlet, 4 = turbine outlet/recuperator hot leg inlet, 4′ = recuperator hot leg outlet/exhaust. **G** and **S** stand for generator and shaft respectively.

When working in CHP configuration, an economizer is added at the recuperator outlet. The later generates hot water at about 70^oC [27]. However, in this work, the model is limited to a recuperated Brayton cycle only. The economizer will therefore neither be modelled, nor discussed anymore.

1.1.2 Towards the new generation of mGTs

As it has been said previously, mGTs present numerous advantages over ICE, their main competitor in the same power category. Among them, some are systematically reported in the literature [5, 6, 17, 28]. They can be listed as below:

- Very suitable candidate for **small-scale CHP**: because waste heat is essentially concentrated in the exhaust gas, and thanks to its relatively high temperature (between 250^oC and 300^oC [2]), mGT is an excellent candidate for small-scale combined heat and power. In ICE, instead, waste heat is split between the exhaust gas, the cooling water and the lubrication oil [6]. Small-scale CHP units based on mGTs typically achieve more than 80% total efficiency (30% electricity production, 50% heat production) [11];

- Low **pollutants** emissions: Turbec, the T100 manufacturer, announces emissions $[NO_x]$ $@15\%O_2 < 15ppm$ and $[CO]$ $@15\%O_2 < 15ppm$ at full load [27]. These performances were assessed by other authors for natural gas [1], but also for alternative biomass-derived low calorific fuels [25];

- **Fuel flexibility**: during the last decade, researchers have proven mGTs capability to run with a wide range of alternative fuels [4, 17, 25, 26, 29]. Because this represents one of the most important future perspective of mGTs, it will be discussed in further details later in this Section;

- Low **maintenance**, noise and vibrations: mGTs have less moving parts than ICE. Vibration and noise, as well as the necessary maintenance, are consequently limited. This confers them a high reliability. Their compact size also makes their installation simpler.

However, despite this large set of advantages, micro gas turbines have not managed yet to successfully penetrate the distributed co-generation market. The reasons are multiple, but an important one is that mGTs in CHP applications are essentially heat driven. In the period of low heat demand, their lower electrical efficiency ($\sim 30\%$) makes them less profitable than ICE ($\sim 35\%$), leading to a machine shutdown. For this reason, the ICE is currently largely dominating the small-scale CHP market [11].

Nevertheless, the above mentioned potential benefits of mGTs over ICE suggest that these machines could be further developed to meet the new market requirements while improving their electrical efficiency. Their ability to run with different fuels and with low pollutants emissions is a great asset to face the challenges of energy transition with renewable fuels [17, 25, 29]. Also, recent improvements made in the recuperator technology could potentially increase their electrical efficiency by 10% [2]. Furthermore, because of their flexible application in alternative and hybrid Brayton cycles, they are now perceived by researchers as serious candidates to sustain smart and flexible energy systems, despite their higher investments costs [5, 30]. In the rest of this Section, the future improvements and new opportunities to which mGTs will be subjected are briefly introduced.

Flexible combustion of alternative fuels

With the emergence of alternative fuels (i.e. biomass-derived, synthetic and blends), there is a need for new machines capable of running with them. While the discontinuous combustion engendered by reciprocating engines is real challenge for the integration of these fuels, the continuous combustion obtained with the gas turbine technology offers the possibility to use a large range of fuels (e.g. gaseous or liquid, with high or low calorific contents) [4]. During the last decade, both theoretical and experimental works were conducted to evaluate mGTs performances with alternative fuelling.

In 2005, Traverso et *al.* [15, 16] conducted theoretical and experimental researches on the control of externally fired mGTs (EFmGTs). Although "dirty fuels", such as coal and biomass, cannot all be considered as renewable fuels, EFmGTs allow to exploit them without the need of gasification. Their works aimed at limiting the fouling issues and thermal stresses on the exhaust side of the recuperator, that appear with the use of external combustion and dirty fuels. Nevertheless, the poor technical and economical performances of EFmGTs limited their diffusion, despite their ability to use renewable fuels, such as biomass.

More recent works of Calabria et *al.* [4, 29] investigated, with a computational fluid dynamics (CFD) approach, the combustion process in mGTs during part load operations while fuelled with synthetic gas (syngas) and hydrogen-methane blends, in comparison with natural gas. They focused on the evaluation of the combustion performances (i.e. in terms of efficiency and pollutants emissions) at part load, to address the potential issues of operations with increased flexibility in power output. They showed that low loads and low calorific fuels generate stability and emissions issues in the combustion process and suggested that attention should be paid to the combustion chamber design when increasing mGTs fuel and load flexibilities. They also proposed improved designs of combustion chambers and fuel injection systems to enable the use of liquid fuels.

Cameretti et *al.* [26] assessed theoretically the combustion features of a bio-fuelled mGT. They examined the combustor response when supplied with poor calorific values bio-fuels issued from anaerobic digestion, solid waste pyrolysis and biomass treatment. They proposed strategies, like alternate pilot injection location and sort of internal exhaust gas recirculation (EGR), to control the combustion efficiency and the pollutants formation. They also emphasized that the combustion of low calorific fuels was similar to part load operations of the mGT fed with natural gas.

Renzi et *al.* [17] rather evaluated, by the mean of numerical simulations, the global impact of low calorific value ($9MJ/kg$) biomass-derived syngas fuels on the operating conditions of a mGT. They showed that for a similar power output, the electrical efficiency was reduced, because of the working fluid composition variation involving an increase of the required heat. They also reported a 75% NO_x reduction and a slight CO increase in the exhaust gas compared to natural gas combustion.

In 2015, Zornek et *al.* [25] developed the first low calorific value combustion chamber ($3.5 - 5.0MJ/kg$) to experimentally validate theoretical results. The developed prototype was based on the concept of flameless oxidation (FLOX) and it was successfully tested inside a mGT. Fig. 1.2 represents the design of the combustion chamber. Their works demonstrated the ability of mGTs to run with low calorific fuels and specified the optimization potential.

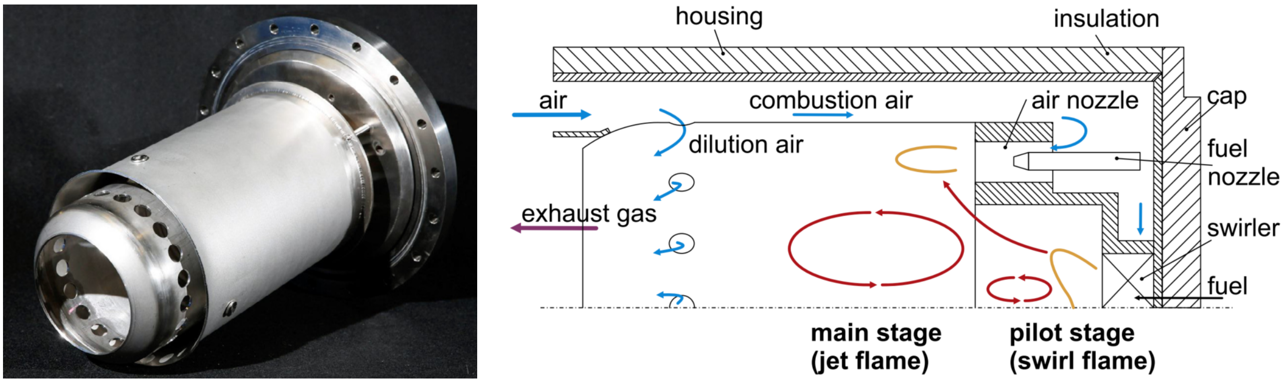

(a) Constructed combustor prototype

(b) 2D visualisation of the combustion scheme

Figure 1.2: Prototype of the FLOX combustor constructed in 2015 by Zornek et *al.* [25].

Improved recuperator performances for increased efficiency

As stated earlier in this Section, one of the challenges facing mGTs is to improve their electrical efficiency to make them economically profitable when they do not work in CHP mode. A route to do so is to increase their Carnot efficiency, by increasing their maximum temperature, as illustrated in Fig. 1.3. However, as it has been mentioned before, one of the restrictive factor for this aim is the limitation of the TOT required to protect the recuperator.

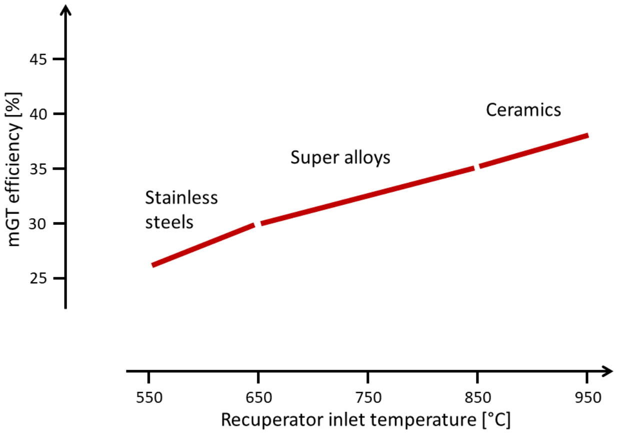

Figure 1.3: Effect of recuperator inlet temperature on efficiency. Adapted from [2].

A recent comprehensive review conducted by Xiao et *al.* [2] summarizes the requirements on recuperators to improve the current mGTs efficiency: (1) they must achieve a heat transfer effectiveness higher than 90% while (2) limiting the total relative pressure losses to 3% and (3) have a good resistance of oxidation and creep at high temperature ($> 650^oC$). Currently, most commercialized mGTs are equipped with primary-surface (type of HEX with bolted/welded/brazed plates) or with plate-fin (plate HEX with offset fins in the heat transfer area) recuperators made up with a stainless-steel matrix. Their maximum inlet temperature is therefore limited to 650^oC, in order to protect them against corrosion, oxidation and creep [2]. The use of alloys instead of pure stainless-steel is claimed by McDonald [31] to increase mGTs efficiency by at least 5%.

But ceramic recuperators outperform metallic ones in terms of high-temperature mechanical and corrosion properties. They raise mGTs efficiency to about 40%, as reported in Fig. 1.3. Although developed since the 1970s, considerable efforts are still required to develop mature, reliable and low-cost ceramic recuperators, according to [2]. The same authors also state that recuperators currently utilized in mGTs already comprise $25-30\%$ of the overall cost.

Novel applications and hybrid cycles

There is a growing interest for the application of mGTs in modified and hybrid Brayton cycles, that could be utilized in distributed generation [5, 6]. Among the cycles that have been studied during the last decade, one can list:

- the *Closed Brayton Cycle* in solar application [16];
- the *Inverted Brayton Cycle*, meeting power demands as low as $1kW_e$ [5, 6];
- the hybrid *Solid Oxide Fuel Cells/micro Gas Turbine* plant (SOFC/mGT), with potential to reach electrical efficiency lying between $65-70\%$ [5, 6, 32];
- and the *micro Humid Air Turbine* (mHAT), which, by recovering the remaining exhaust waste heat, could increment the electrical efficiency by more than 3% [1, 13, 33].

The mHAT has been studied by several authors and a prototype has been constructed at VUB, Belgium [14]. The simplicity of its implementation, based on a existing mGT, makes the concept very attractive to the end of boosting the electrical efficiency of small CHP units during periods of no heat demand. The first modification made on a typical recuperated mGT is the addition of a heat exchanger to recover the remaining waste heat from the exhaust gas. This heat is used to warm up water, later injected into the cycle to achieve the heat recovery, following the same principle as the Humid Air Turbine (HAT). Different concepts of humidification and injection locations (i.e. before or after compressor, directly inside combustion chamber, ...) have been investigated before selecting the inclusion of an air saturator at the compressor outlet [1, 9]. Figure 1.4 reports the layout of the mHAT prototype constructed at VUB. However, despite the potential of mHATs (i.e. more than 4% absolute increase in efficiency were experimentally observed), economical analyses, accounting for cogeneration policies, showed that the concept is currently not profitable (i.e. as well as the other small-scale CHP concepts evaluated for the comparison) [11].

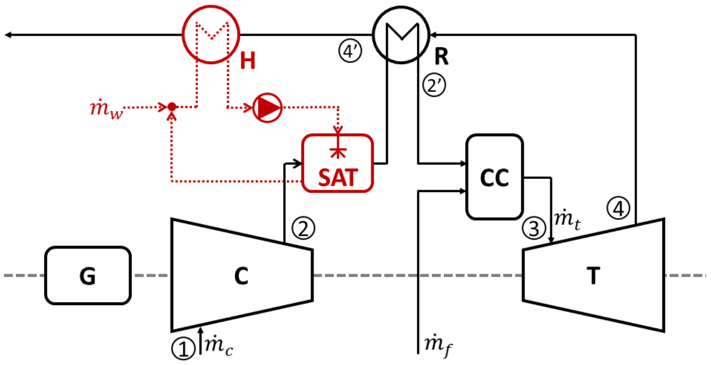

Figure 1.4: Layout of the mHAT prototype installed at VUB, adapted from [13]. New elements are the air saturator (**SAT**) and the water heater (**H**).

The other alternative and hybrid mGT cycles will not be further detailed here. Nevertheless, there is a general agreement in the literature on the need of more development, numerical and experimental investigations in this research field [6, 33]. Indeed, the development of mGT concepts, achieving both power and heat decoupling with a very high flexibility in terms of fuel and power demand tracking capabilities, will require the use of numerical simulation and diagnostic tools for cycle optimization and prediction of performance degradation [33, 34].

Steady state models are first required to analyse the potentials of innovative cycles and to predict off-design performances under different conditions. In a second development phase, dynamic models are of absolute necessity. Indeed, the dynamic behavior of new systems can change significantly compared to classical mGTs. Numerical simulation is therefore essential to study the dynamics of novel cycles and to develop suited control strategies [5].

1.2 The Turbec T100

This Master Thesis will use the Turbec T100 as reference machine for the development of a general mGT dynamic simulation tool. This is motivated by the proximity between the UCLouvain research team and the Thermodynamics and Fluid Mechanics Group from VUB, which has installed a mGT test rig based on a T100 machine. This Section will introduce this machine and review some previous works conducted on it by different research teams.

The T100, originally manufactured by Turbec SPA, now by Ansaldo Energia, is a $100kW_e$ mGT commercialized in both CHP and pure electric utility configuration. In CHP mode, its maximal thermal output is about $165kW_{th}$ [27]. The machine power train is represented in Fig. 1.5 [23]. The T100 is constructed around single stage centrifugal compressor and radial turbine. The latters are both connected to a water-cooled high-speed permanent magnet generator (also acting as a starter) with a single shaft assembly, as depicted in Fig. 1.6. The high frequency AC power from the generator is rectified and converted to grid frequency with a power electronics system (hidden behind the door in Fig. 1.5). The control system is fully automatic and monitors the *TOT* and power output. The T100 is equipped with a single CAN-type lean pre-mix combustion chamber, well visible on the bottom left-end side of Fig. 1.5. The fuel/air equivalence ratio is about

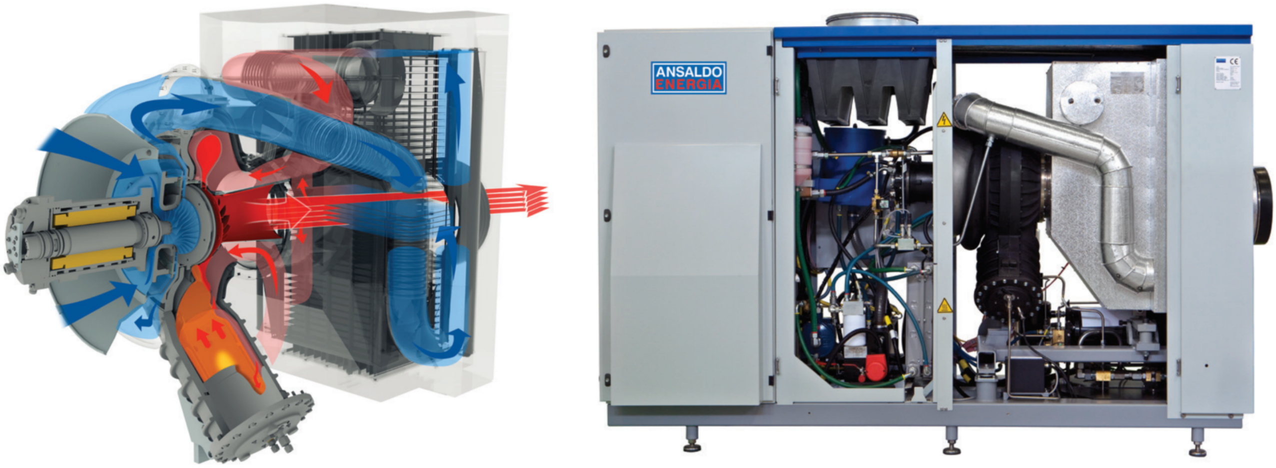

Figure 1.5: T100 power train. Sketch-up and picture from the manufacturer [23].

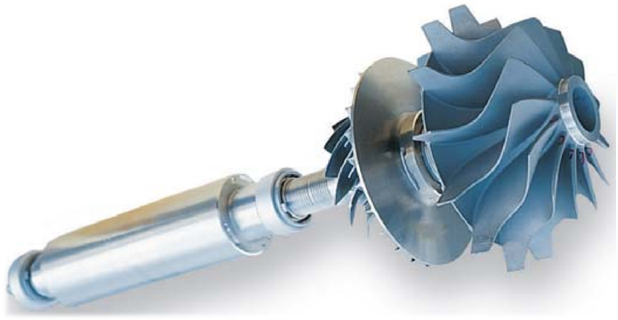

Figure 1.6: T100 single-shaft assembly. *Left to right*: rotor of high-speed generator, centrifugal compressor and radial turbine. From [35].

$\phi = 0.13$ at full load while running with rich natural gas (i.e. 92% CH_4 molar composition) [26]. The fuel inlet pressure is raised with an auxiliary compressor (or fuel booster) to about $6-7bar$. The mGT efficiency is improved with a large rear-mounted recuperator, also well visible in Fig. 1.5. This is a primary-surface mixed counter- and cross-flow type HEX, as it will be further explained in Section 3.5 [36, 37]. More representations of the T100 recuperator are provided in Fig. 1.7. The main nominal technical characteristics provided by the manufacturer are reported in Table 1.2 [23, 27].

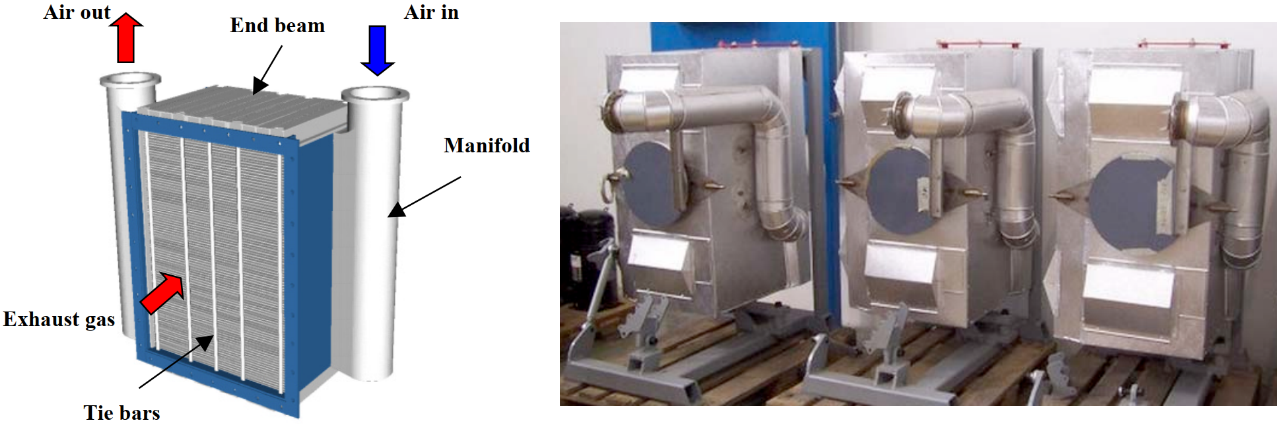

Figure 1.7: T100 recuperator. Sketch-up from [36] and picture of ready to be installed recuperators from [37] (courtesy of Turbec).

Characteristics	**Nominal value**
Pressure in combustion chamber	$4.5bar$
Turbine Inlet Temperature (TIT)	950^oC
Turbine Outlet Temperature (TOT)	645^oC
Rotational speed	$70,000rpm$
Fuel Lower Heating Value (LHV)	$38-56MJ/kg$
Fuel consumption	$333kW$
Fuel inlet pressure (booster)	$6-7bar$
Electrical power output	$100 \pm 3kW_e$
Electrical efficiency	$30 \pm 2\%$
Exhaust gas flow rate	$\simeq 0.79kg/s$
Exhaust gas temperature	$\simeq 270^oC$
Electrical generator (and starter)	Water-cooled high speed permanent magnet
NO_x emissions	$\leq 15ppm(v) \simeq 31mg/Nm^3$ @$15\%O_2$
CO emissions	$\leq 15ppm(v) \simeq 19mg/Nm^3$ @$15\%O_2$

Table 1.2: T100 nominal characteristics reported by the manufacturer [23, 27]

According to the manufacturer, 105 units had already been commercialized and had accumulated a total of 748, 885 operating hours in 2004. That year, 14 machines where used in laboratories for experimental purposes [35]. Indeed, after a literature review, it turns out that the T100 is often used as reference machine for the construction of numerical models and for the development of alternative cycles. Some of the research teams frequently encountered in literature during this work and utilizing the T100 are non-exhaustively listed in Appendix A, and their contribution is briefly introduced.

1.3 Modelling methods and approaches

As explained in Section 1.1.2, the development of a more flexible generation of mGTs (i.e. in terms of load and fuel), utilized in advanced cycles, will require numerical simulations.

While the improvement in fuel flexibility can first be achieved thanks to CFD approaches (e.g. for the development of new combustion modes and combustor designs) [25,26,29], the global impact of alternative cycles and fuelling on the interaction between new components and conventional turbomachinery must be computed with more generalist steady state and dynamic models. Indeed, with the inclusion of new components, such as air saturators in humidified cycles, ceramic heat exchangers or fuel cells in hybrid mGT plants, the systems dynamics undergo significant changes with increased operational requirements [5,6,21]. Therefore, flexible and modular tools, able to achieve both steady state and dynamic simulations, are extremely useful for the development of these new cycles [21]. The applications fields of these numerical models in gas turbine engines during development and operational phases can be summarized in three main categories, as follows:

- *Systems* ***identification*** and *theoretical assessment* of the *cycles dynamic behaviour*. Numerical tools are indeed a quick and cost-less way of verifying the theoretical value of certain operational parameters in the systems [21,38];

- *Design*, *development*, *optimization*, *testing* and *validation* of ***control systems*** [21,38,39]. Dynamic models enable to develop and test control strategies, aiming for instance at improving the response settling time while ensuring that its under and overshoots respect the safety and reliability constraints of the system components. Part of the control also consists in the establishment of start up and shut down procedures, that are critical maneuvers since the turbine is exposed to large changes in the operational parameters, which must stay within allowed operational boundaries. Numerical investigations therefore prevent the system from damages that could happen experimentally;

- *Condition* ***monitoring***, ***fault detection*** and *diagnostic*. Numerical clones play an important role in the efforts for gas turbine operators to shift from preventive to predictive maintenance, as well as for the detection and prediction of faults in the systems [38,39].

Furthermore, with the emergence of real-time simulation, allowing the coupling between control systems hardware with numerical tools instead of with the actual machines, these models should also respond to low computational complexity requirements [5,40,41]. This typical application is illustrated in Fig. 1.8.

To the aim of developing high accuracy dynamic models with a low complexity for mGTs, one can draw inspiration from the previous developments made in the frame of industrial and aero-derivative gas turbines. This Section will consequently present a large scope review of the different modelling approaches, not narrowing it to mGT models only.

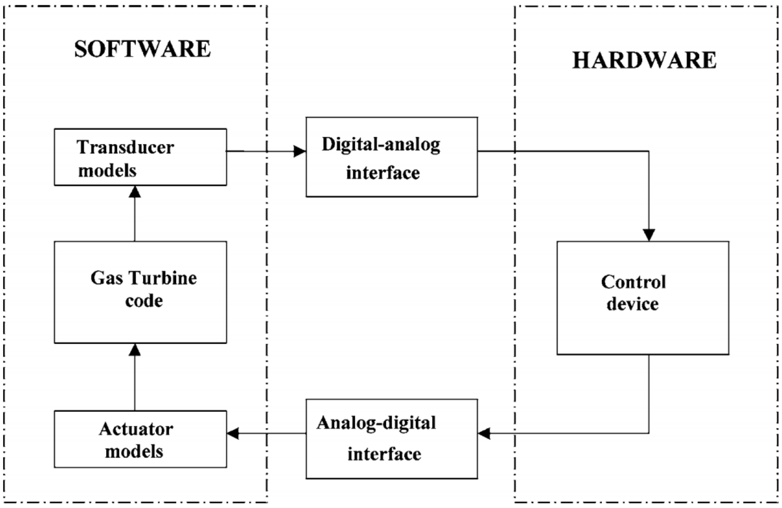

Figure 1.8: Real-time simulation software interfaced to hardware control devices. Taken from [40].

It is often proposed to classify these models with two different metrics: on one hand with the mathematical formulation (i.e. linear or non-linear) and on the other hand with their foundation type (i.e. data-driven or physics-based) [38]. Therefore, Section 1.3.1 reviews the modelling approaches based on their physical nature while Section 1.3.2 sorts them depending on their mathematical formulation. Some selection criteria are introduced in Section 1.3.3. There, the choice of the modelling method for the present work is also assessed.

1.3.1 Physical considerations

When the physical phenomena inside the system are well known, *physical* (or *white-box)* models are constructed with physical laws. Instead, if no or little information is available about the physics of the system, *data-driven* (or *black-box*) models are used. However, experiences show that a hybrid version of these approaches offers the best model performances, as it will be illustrated later in this Section.

Physical (white-box) models

White-box models are used when there is sufficient knowledge about the physics of the system [38, 39], and they rely on the physical laws behind its operation. Therefore, they allow for realistic simulations of its behaviour while giving access to numerous physical parameters (e.g. pressure, temperature, flow rates, streams composition, ...). These physical laws are the *constitutive equations* (i.e. time-independent relations), such as the compression and expansion isentropic models or the ideal gas law, and the *conservation equations* (i.e. time-dependent relations, differential equations) like the mass, momentum and energy conservation applied to the gas volumes and to the moving parts. The number of such equations typically varies from 5 to 15 [38]. These white-box models are also often referred as "thermodynamic models".

The complexity of physical models is directly connected to their temporal and spatial dependency. The temporal dependency is related to the number of differential equations while the spatial dependency indicates the number of partial derivatives in the differential equations. To limit this complexity, a common approach is to reduce the systems components to their inlet and outlet boundaries while assuming a uniform spatial distribution of the parameters at their inlet and outlet sections. With these simplifications, the models take a 0D form and their expression is mathematically reduced from partial to ordinary differential equations. Another advantage deriving from these simplifications is the models applicability to any system with an unknown geometry.

Starting from the 1980s, simplified physical models were introduced for the simulation of heavy-duty gas turbines, suitable for use in power systems dynamic studies. Rowen [42] was a pioneer in this domain. Hussain et Seifi [43] and de Mello et *al.* [44] proposed more accurate models, but their application remained limited in power systems simulation programs. In fact, models aiming at the processing of gas turbines operating conditions (i.e. for systems identification and controllers development) came later with the introduction of turbomachinery performance maps inside these models. Because these maps are mainly constructed from experimental values, the latter cannot be considered as purely physical anymore. This will be further discussed along in this Section.

Data-driven (black-box) models

Black-box models are used when no or very few information is available about the physics of the system. In contrast to white-box models, they use available empirical information (i.e. from

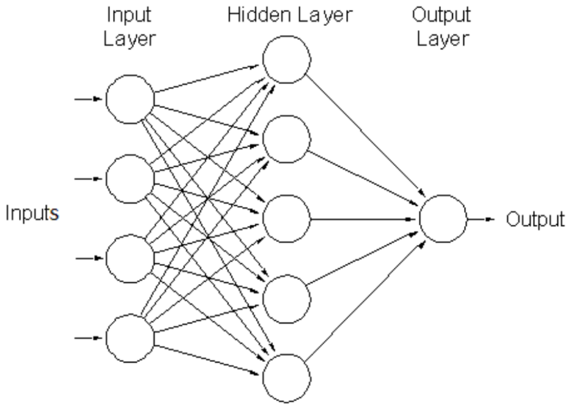

Figure 1.9: A simple structure of a typical Artificial Neural Network (ANN) with input, hidden and output layers. Taken from [39].

test bench characterization) and are determined by optimization methods, aiming at identifying the system [38, 39]. They construct non-physical relations between the systems variables based on empirical input and output performance data. Artificial Neural Networks (ANN), that are constructed through machine learning, are one of the most widespread method. Such structures, illustrated in Fig. 1.9, can capture complex non-linear gas turbine behaviors. Starting from 2001, Chiras et *al.* [45] estimated a NARMAX (non-linear auto-regressive moving average with exogeneous input) model for an aircraft engine. Jurado [46] proposed a few years later a NARX (non-linear auto-regressive exogenous) model for micro gas turbines and for an application in model predictive control. These intelligent models build upon previous and current values of the input and output series.

However, simpler approaches can be selected in black-box models. For instance, linear models, whose parameters can be estimated at the least squares sense, can be utilized. Nevertheless, these simpler models have a validity limited to near design operating point because gas turbines show highly non-linear behaviors [46].

Another very common application of data-driven models is the representation of turbomachinery performances, which are obtained experimentally at some discrete operating points, thereafter reproduced on performance maps and extended to the entire operating domain. This will be further discussed in Chapter 2.

Hybrid (grey-box) models

Grey-box models combine the advantages of white-box and black-box methods to maximize their accuracy. In mGT models, this hybridization is typically introduced by the implementation of performance maps. The use of empirical correlations, most often for the recuperator heat transfer performances or for pressure losses coefficients, also contributes to this hybridization.

Such models were for instance introduced by Blotenberg [47] (with a map approach for the high pressure turbine and a Stodola's model for the low power one) and Bettocchi et *al.* [48] for industrial gas turbines at the end of the 1990s. They essentially focused on the evaluation of the gas turbines speed and the generated power during transient. Later on, authors like Ailer et *al.* [49, 50] and Camporeale et *al.* [40, 51] started to investigate the dynamics of all thermodynamic quantities inside the system. In 2005, Traverso [21] introduced `TRANSEO`, a `MATLAB` and `Simulink` based modular and flexible tool for alternative micro gas turbines cycles, that allows for both steady state and dynamic simulations. This tool achieves computation with either one-dimensional Euler equations for fluid dynamics with the "dynamic model", either with non-dimensional equations with the "lumped volume" model. It automatically predicts the time step for integration based on the time scale of the relevant time-dependent phenomena. `TRANSEO` has recently been used by [11] with the "lumped volume" approach for dynamic simulations of a mHAT, showing relatively good agreement with the experimental data.

Nowadays, grey-box models have turned out as a generic approach for dynamic modelling of mGTs. Authors like Henke et *al.* [5] obtained, for instance, extremely satisfying results with it, even during start-up and shut-down procedures.

1.3.2 Mathematical formulation

The different dynamic models are opposed by their mathematical formulation. On one hand, linear models, for which all objective functions and constraints of the system are represented by linear equations [39], achieve very good performances in terms of numerical computation. This formulation indeed allows for relatively fast code execution. Also, linear formulation is helpful for the development of control systems, since the control theory usually assesses strategies using linear models [41].

One the other hand, non-linear models can capture the dynamics of complex and sensitive systems (such as gas turbines) with a superior accuracy [39]. Indeed, the latter have a highly non-linear behavior, which makes linear model irrelevant out of the near-design operating point region. However, non-linear models involves much larger computational complexity compared to linear formulations and are not always suited for the development of control systems. From these remarks, it turns out that there is a serious trade-off between models complexity and accuracy.

In order to reduce the non-linear models complexity while preserving their superior accuracy (e.g. for real-time applications [40]) and to obtain formulations suitable for the construction of control systems [41], linearization techniques have been introduced. The newly formed linearized models can describe the engine behavior around a set of steady state operating points with a good accuracy. Hadroug et *al.* [52] utilized the Taylor series for the linearization around equilibrium points of a non-linear model for a two-shafts gas turbine. Mehrpanahi et *al.* [53] used intelligent methods for the extraction of the linear transfer functions of three-shafts gas turbines based on non-linear models. All these authors showed that linearization techniques could successfully be applied to gas turbines with the aim of developing control systems.

1.3.3 Selection criteria and context decision

Criteria usually apply when selecting a modelling approach. They can be identified as below:

- *Modelling* ***objectives*** and *application*: the goal of this Thesis is to develop a modular and flexible tool for the simulation of transients in existing mGTs utilized in novel applications. Therefore, this tool should allow for the identification of new systems and contribute to the development of control systems;

- ***Accuracy*** and *provided information*: the model will be used for research and development purposes. It must consequently provide high-fidelity results for all the relevant parameters of the system (e.g. pressures, temperatures, flow rates, speed);

- ***Computational*** *considerations*: the model is not intended to be used in real-time simulation applications. However, the transients should be computed on a personal computer in an acceptable time frame (e.g. calculation to simulated time ratio limited to 10).

Based on the above considerations, it is decided for this work to construct a **grey-box non-linear model**, also referred as *thermodynamic model*.

During this literature survey, it has been observed that many thermodynamic models for (m)GTs were developed in the `MATLAB/Simulink` environment. At least 14 different models using this language were identified [3, 6, 12, 17, 18, 21, 22, 24, 40, 49, 54–57]. At VUB, `Aspen` has been intensively used for the study of mHAT [1, 9, 58, 59]. Henke et *al.*, who were interested in achieving very low computation time, implemented their model in `FORTRAN`. However, it is decided, for open-source reasons, to construct the present simulation tool in the `Python` programming language. This will be further discussed in Section 3.1.2 and Chapter 4.

1.4 Current works in the research team and thesis scope

Two doctoral research projects started about one year ago and are currently ongoing in the research team at UCLouvain. One focuses on CFD simulations of flameless combustion in micro gas turbine operating with alternative fuels. The second deals with operational flexibility of micro gas turbines (i.e. alternative thermodynamic cycles and fuels) towards integration in smart systems. Several Master Thesis projects related to these topics should also be launched in the coming months.

Therefore, one of the present Thesis goals is to provide an overview of the mGT research field for future works in the domain (e.g. alternative cycles, dynamic models). The concepts and tools developed within this work are consequently conceived with the perspective of forthcoming utilization and improvements.

CHAPTER 2

PERFORMANCE MAPS MODELLING

The performances of turbo-machines in off-design operating conditions are traditionally represented on so-called *performance maps* (or *characteristic maps*). These maps are usually established by the manufacturer and are constructed based on experimental analyses. They can also be obtained from high-fidelity CFD when the machine geometry is well known (e.g. by researchers when experimental analyses are not affordable) [60]. Because they are constructed from steady state variables, these maps are sometimes qualified as *static maps.* Performance maps provide a precious and vital information for the development of off-design models (e.g. transient models). However, because of their costly development, they often remain the manufacturer's property. Modelling these maps when they are partly known is therefore of crucial interest.

This Chapter first briefly reviews and summarizes the fundamentals of performance maps in Section 2.1. Section 2.2 then shortly presents widespread techniques for the modelling of these maps. Finally, the modelling of the T100 maps is described in Section 2.3.

2.1 Turbomachinery and performance maps

The parameters of interest when modelling turbo-machines are the inlet and outlet pressures and temperatures, as well as the angular speed and the mass flow rate through the components. Therefore, and without loss of generality, for both compressors and turbines, the performance maps relate the pressure ratio π and the mass flow rate $\dot{m}$ (or any similar metric, such as the corrected, normalized or reduced flow) to the rotating speed N (or any metric such as the corrected, normalized or reduced speed) via so called *iso-speed lines.* The reduced values are often referred as "corrected values". The units of the utilized metrics should therefore always be specified to avoid any confusion. Moreover, the isentropic efficiency η_{is} is also generally represented with different contours, called *iso-efficiency lines.* Because of the maps nature, given any two values out of N, $\dot{m}$ and π, the third and η_{is} can be obtained. However, when choosing the two variables to define the operating point, attention should be paid to make sure that they are not collinear otherwise they would not result a unique operating point [61].

The most common metrics utilized to express the mass flow and the rotating speed are the *corrected* (or *referred*) values, the *reduced* (or *quasi non-dimensional*) values and the *normalized* (or *non-dimensional*) values [62]. The corrected values are a mean of standardization used to represent the operating parameters of the machine in atmospheric conditions at Sea Level, on a Standard Day (e.g. $101.325[kPa]$, $288.15[K]$). The reduced values are derived from the actual inlet conditions only. The advantage of this definition is that it does not involve any reference value. The normalized values are often obtained from the normalization with the design operating point, but they are rarely presented on performance maps. Table 2.1 summarizes the definition of each variable.

Type	**Metric**	**Symbol**	**Definition**	**Units**
Absolute	Speed	N	$-$	$[rpm]$
Absolute	Mass flow	$\dot{m}$	$-$	$[kg \cdot s^{-1}]$
Corrected	Speed	N_{cor}	$N\sqrt{\frac{T_0}{T}}$	$[rpm]$
Corrected	Mass flow	$\dot{m}_{cor}$	$\dot{m}\frac{\sqrt{T/T_0}}{p/p_0}$	$[kg \cdot s^{-1}]$
Reduced	Speed	N_{red}	$\frac{N}{\sqrt{T}} = \frac{N_{cor}}{\sqrt{T_0}}$	$[rpm \cdot K^{-0.5}]$
Reduced	Mass flow	$\dot{m}_{red}$	$\dot{m}\frac{\sqrt{T}}{p} = \dot{m}_{cor}\frac{\sqrt{T_0}}{p_0}$	$[m \cdot s \cdot K^{0.5}]$
Normalized	Speed	N_{norm}	$\frac{N}{N_{ref}}$	$[-]$
Normalized	Mass flow	$\dot{m}_{norm}$	$\frac{\dot{m}}{\dot{m}_{ref}}$	$[-]$

Table 2.1: Definition of the standard metrics used in performance maps. p and T stand for total inlet pressure and temperature, subscripts 0 and ref are respectively for atmospheric conditions at Sea Level on a Standard Day and reference value (i.e. design value).

Since the accuracy of transient models is strongly dependent on off-design performances of turbo-machines, it is of interest to correctly extract and capture the information provided on their maps. However, though accurately sampling the curves depicted on the map is an easy task, the main limitation in this process comes from the limited number of provided operating points. Indeed, this information is obtained from costly test rigs and often remains the manufacturer's proprietary information [60, 63]. To overcome this constraint, researchers have developed several routes to calculate, extend (a partially known map can be extended towards unknown speeds regions by means of interpolation and extrapolation [63]) and represent the performance maps. Yet, a large range of manufacturer's data being at our disposal in this work, calculation and extension will not be further detailed. Some concepts of maps representation in analytical and numerical forms will be introduced in Section 2.2.

Figure 2.1 depicts the performance maps of the Turbec T100, as these were constructed by Caresana et *al.* [3]. They will be utilized later in this Section to illustrate some of the phenomena taking place in turbomachinery.

2.1.1 Compressor maps

This Section briefly describes the conditions in turbo-compressors and establishes the link between the phenomena and their representation on the maps.

Turbo-compressors are components in which the input work driving the shaft is used to increase the pressure of the input flow via aerodynamic forces. Therefore the compressor pressure ratio, also called compression ratio, is defined as

$$\pi_c = \frac{p_{c,out}}{p_{c,in}} , \tag{2.1}$$

with $p_{c,in}$ and $p_{c,out}$ are the inlet and outlet pressures respectively. At a given rotational speed, the compression ratio is a function of the input flow (i.e. mass flow rate, pressure and temperature). Nevertheless some limitation exists in the operating range and all mass flows

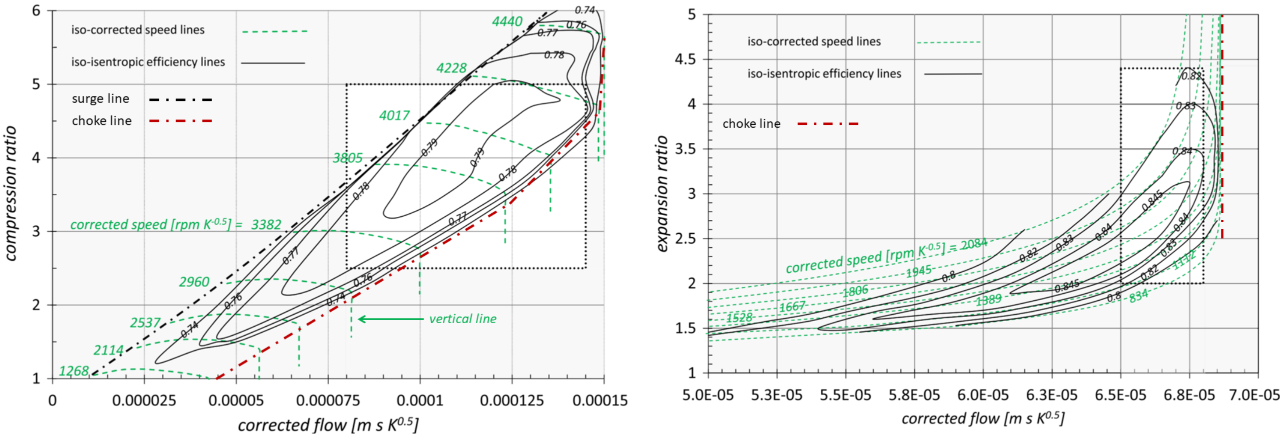

(a) Compressor

(b) Turbine

Figure 2.1: Performance maps of the T100 originally constructed by Caresana et *al.* [3] upon manufacturer's data. Note that the reduced flow utilized here is named under the "corrected flow" terminology.

cannot go through the machine.
The following enumerates some of the essential phenomena occurring in turbo-compressors.

Choking of the compressor

When the flow rate increases, since the equivalent hydraulic diameter of the machine remains constant, the flow velocity increases as well. If at some location inside the compressor the velocity becomes sonic (i.e. $M = 1$), the velocity and mass flow rate cannot increase anymore (provided that there is not any converging-diverging duct). The compressor is then considered to be choked. Nonetheless, in choking conditions, the compression ratio can still vary according to the rotating speed. Although it is locally sonic, the aerodynamic flow is maintained and it keeps increasing the pressure level proportionally with the air flow rate, itself related to the rotating speed.

The *choke line* (or *sonic line*) is the line connecting the points of iso-speed lines where the mass flow rate reaches its maximal values (i.e. the intersection between the curved and vertical parts of the iso-speed line). The vertical lines and choke line (red dash-dot line) of the T100 compressor are well visible in Fig. 2.1a.

Surging of the compressor

This phenomenon occurs when the flow rate becomes too low, leading to a complete breakdown of the aerodynamic flow and resulting in flow reversal. Surging also results in instabilities in the flow field and can be destructive for the machine. Surging origins are multiple, including stall (flow detachment when the angle of attack is above its critical value and occurring in off-design operations) and reduction of inlet mass flow rate (e.g. via inlet guide vanes, when any).

The *surge line* connects the points starting from which a surge cycle is initiated. These points correspond to the left end side of the iso-speed lines. The surge line is usually a straight line, such as illustrated for the T100 compressor in Fig. 2.1a (black dash-dot line).

The *surge margin* SM is a metric characterizing the distance from the surge limit ($s.l.$) for a given rotational speed. It can be defined as

$$SM = \frac{\pi_{c,s.l.}\dot{m}_c}{\pi_c\dot{m}_{c,s.l.}}\,, \tag{2.2}$$

where $\dot{m}_c$ and $\dot{m}_{c,s.l.}$ are the actual mass flow rate and the one at the surge limit corresponding to the given speed [13]. π_c and $\pi_{c,s.l.}$ are the actual and the surge limit compression ratios.

Isentropic efficiency

Even though some metrics such as polytropic efficiency exist in turbomachinery, most of the time the isentropic efficiency is only provided and used. It is defined as

$$\eta_{c,is} = \frac{h^*_{out,is} - h^*_{in}}{h^*_{out} - h^*_{in}} , \tag{2.3}$$

with h^*, the total enthalpy before and after compression, and in comparison with an isentropic process.

2.1.2 Turbine maps

In opposition to compressors, turbines use the pressure gradient between their inlet and outlet sections to generate work and drive the shaft. Therefore the turbine expansion ratio is defined as

$$\pi_t = \frac{p_{t,in}}{p_{t,out}} , \tag{2.4}$$

with the inlet and outlet pressures. At a given rotational speed, the expansion ratio is a function of the input flow (i.e. mass flow rate, pressure and temperature). Nevertheless, there also exists some limitation in the operating range and all mass flows cannot go through the machine. Similarly to turbo-compressors, there is an upper limit above which the mass flow rate cannot increase anymore (choking of the turbine). The sonic (or choke) line builds upon the connection of the choking points of each iso-speed line. This is well visible for the T100 on the right-end side of the map in Fig. 2.1b (red dash-dot line).

As for compressors, the isentropic efficiency is the most common metric used to characterize the relationship between the inlet and outlet enthalpies. It is defined as

$$\eta_{t,is} = \frac{h^*_{in} - h^*_{out}}{h^*_{in} - h^*_{out,is}} , \tag{2.5}$$

with h^*, the total enthalpy before and after expansion, and in comparison with an isentropic process.

2.2 Common practice in performance maps modelling

As previously stated, when experimentation is not affordable, the generation process of detailed maps can be split into three main fields: map calculation, map extension and map expression [63]. The first covers the determination of the machine performances from numerical flow calculation when the geometry is known. If the actual map is partially known, the second field includes the interpolation and extrapolation techniques used to extend the information to unknown speeds (e.g. low speed region). The third field gathers the methods used to express the maps when a sufficient amount of performance data is known for the machine (e.g. from previous investigations by manufacturers or researchers). It basically consists in the development of techniques used to represent analytically or numerically the maps.

As the T100 manufacturer's data are available for this work, this Section focuses only on the third field.

Reviews on map expression methods were conducted during the past decade with, as main purpose, the development of efficient and general methodologies to model the maps [60, 63, 64]. The resulting four categories are listed below and briefly described.

2.2.1 Auxiliary parameter method

This method was first introduced by Kurzke [65] with the β lines, exempt of any physical meaning. The underlying idea is to construct an auxiliary variable so that the tuple of variables (corrected speed and β) define completely any operating point [66]. An advantage of this technique is that it guarantees the uniqueness of the operating point for any couple of pressure ratio and mass flow rate [66]. Quasi-physics-based methods using auxiliary variables were also further introduced [60, 64] in order to extend the map model to sub-idle regions [67].

2.2.2 Scaling and shifting method

This method is one of the most popular. It relies on the scaling and shifting of a similar map to the actual one through optimization processes. It is especially used when very few operating points are known for the actual machine (e.g. one or two design points). Kong et *al.* [68] and Li et *al.* [69] are the main references for this technique and still improve it by coupling it to intelligent methods (described below) such as Genetic Algorithms (GA) [60]. This method provides a high accuracy near the known points. Nevertheless the actual map shape cannot be entirely predicted [63].

2.2.3 Fitting method

This method is used when enough operating data are available (i.e. sufficient number to represent the global map shape, typically three or four per iso-speed line, at minimum). A fitting pattern is tuned to capture the shape of the map (i.e. represented by the large data set) by optimizing the regression error. Thus, the fitting coefficient are set to minimize the model errors.

Different fitting patterns with either some or no physical meaning have been explored. Ailer et *al.* [49] used linear and parabolic patterns for both speed and efficiency lines. Moore-Greitzer [70] rather worked on cubic approximations for speed lines, although the emergence of oscillations, associated to the third order polynomials, limited the model accuracy. Drummond-Davidson [71] further improved this cubic pattern with the introduction of penalty functions aiming at a smoothing of the oscillations. The use of polynomials being limited by their natural oscillating behaviour, Tu-Chen [72] explored exponential patterns to get rid of this constraint. Misté-Benini [61, 66] rather combined an improved version of the auxiliary variable β developed by Kurzke [65] with fitting functions to construct an hybrid model.

Relatively recent publications of Tsoutsanis *al.* [60, 64] suggested that elliptical and super-elliptical curves were promising patterns for the fitting of compressors iso-speed and iso-efficiency lines. They also showed that exponential and polynomial curves could efficiently represent the turbine lines. Yang et *al.* [63] also worked on an improved version of elliptical curves with the introduction of scaling factors.

2.2.4 Intelligent method

The limitation of fitting methods is that the pattern intrinsically depends on the map shape. Depending on the machine nominal power and type (axial or radial), the shape of the curves (e.g. iso-speed curves) can range from almost horizontal to quasi vertical. It is therefore difficult to develop a general fitting function able to handle any type of map. Data-driven fitting methods using Artificial Neural Networks (ANN), such as proposed by Yu et *al.* [73] and Ghorbanian et *al.* [74], have arisen as promising methods proving good predictions of compressor map shapes. Although they essentially rely on machine learning techniques, these methods remain usually classified under the simple "intelligent" terminology in the literature [60, 63].

2.3 Modelling the T100 performance maps

In most dynamic models for mGT's, the pressure ratio and shaft rotating speed are used as input variables to obtain the mass flow rate through the component and its isentropic efficiency, further used to compute the temperature at the component outlet. However, some models use the rotating speed and mass flow to obtain the pressure ratio and isentropic efficiency. This is the case of di Gaeta et *al.* who developed a 0D steady state model iterating on the air flow rate to allow matching between rotating components [12]. Bracco et *al.* [55] also used this approach and constructed a semi-static model, forcing the mass and energy balances, and adding capacitance and inductance blocks to integrate the dynamic phenomena.

As it will be justified in Chapter 3, the model developed here uses the pressure ratio and rotating speed as input variables. The goal of this Section is thus to develop an expression method for both the compressor and the turbine maps, as written below:

$$\dot{m}_c = f(\pi_c, N) \qquad \eta_{is,c} = f(\pi_c, N) \tag{2.6}$$

$$\dot{m}_t = f(\pi_t, N) \qquad \eta_{is,t} = f(\pi_t, N) \tag{2.7}$$

Thanks to the significant number of performance data that were available and because of its simplicity, the fitting method was selected to express the maps. After a review of different fitting patterns (polynomials, exponential, elliptical and super-elliptical) and a comparison of their performances, a fitting function has been assigned to each of four variables to be expressed. The information provided on the manufacturer's maps being the reduced values, only the latter are used when expressing the maps. These maps were digitized and sampled with the *WebPlotDigitizer* applet [75]. The compressor map is captured with the following *elliptical patterns*:

$$\left(\frac{\dot{m}_{c,red}\cos\theta_{\pi_c} + \pi_c\sin\theta_{\pi_c}}{a_{\pi_c}}\right)^2 + \left(\frac{\dot{m}_{c,red}\sin\theta_{\pi_c} - \pi_c\cos\theta_{\pi_c}}{b_{\pi_c}}\right)^2 = 1\ , \tag{2.8}$$

$$\left(\frac{\eta_c\cos\theta_{\eta_c} + (\dot{m}_{c,red} - v_{\eta_c})\sin\theta_{\eta_c}}{a_{\eta_c}}\right)^2 + \left(\frac{\eta_c\sin\theta_{\eta_c} - (\dot{m}_{c,red} - v_{\eta_c})\cos\theta_{\eta_c}}{b_{\eta_c}}\right)^2 = 1\ , \tag{2.9}$$

where $\dot{m}_{c,red}$, π_c, η_c are the air flow rate, the compression ratio and the compressor isentropic efficiency respectively, and where a, b, θ and v are the fitting coefficients. The turbine map is expressed with the following *polynomial* and *exponential patterns*:

$$\dot{m}_t = a_{\pi_t}\pi_t^5 + b_{\pi_t}\pi_t^4 + c_{\pi_t}\pi_t^3 + d_{\pi_t}\pi_t^2 + e_{\pi_t}\pi_t + f_{\pi_t}\ , \tag{2.10}$$

$$\eta_t = a_{\eta_t} + b_{\eta_t}(1 - \exp(\pi_t^{c_{\eta_t}})) + d_{\eta_t}\pi_t\ , \tag{2.11}$$

where $\dot{m}_{t,red}$, π_t, η_t are the mass flow rate, the expansion ratio and the turbine isentropic efficiency respectively, and where a, b, c, d, e and f are the fitting coefficients. The choice of these fitting patterns is based on the a trade-off between complexity (i.e. number of degrees of freedom) and performance (i.e. typical fitting error reported in the literature). Other functions were tested but are not reported here because of the poor performances they offered compared to the selected patterns. This will be further justified in Section 2.3.3.

Once the fitting functions assigned, an optimization process at the least square sense was carried out with the sampled points in order to minimize the fitting error and obtain the optimum fitting coefficients for each reduced speed. This was achieved with the *curve_fit* function from the *scipy.optimize* class of the *SciPy v1.6.2* library [76] using the *Trust Region Reflective* algorithm (*trf*). From the experience gained during the map modelling, it should be noted that the fitting quality is highly sensitive to the lower and upper bounds assigned to the fitting coefficients.

An important concern about the uniqueness of the operating point should be raised here. While Yang et *al.* [63] and Tsoutsanis et *al.* [60, 64] worked on the expression of the GE-LM2500 maps (aero-derivative gas turbine), for which the uniqueness of the operating point is guaranteed at any speed and for any compression ratio, this requirement is not fulfilled for the T100. Looking at Fig. 2.1a, it turns out that for low speed regions, at a given speed, one compression ratio can lead to two reduced mass flow rates. Since the elliptical curves have to be computed numerically, a trick to overcome this issue is, when performing dynamic simulations, to set as initial guess a particular value for the mass flow rate (i.e. the value from the previous time step). This should, in principle, provide the one solution out of the two which is the closest from the actual one. Nevertheless, this has to be proved and will be further discussed Chapter 5.

In Eqs. (2.8), (2.9), (2.10), & (2.11), the fitting coefficients are functions of the rotating speed. Tsoutsanis et *al.* [60, 64] and Yang et *al.* [63] chose to express them as polynomials to develop a completely analytical model for the maps. However, due to their natural propensity to oscillate, polynomials can give to the coefficients a value leading to wrong performance expressions at some speeds. For this reason, piece-wise definitions of the coefficients via cubic-splines were used in this work. A linear piece-wise definition, although non-physical because of the generated discontinuities in the first derivative, could also be used for that aim. The obtained coefficients are plotted for a wide range of reduced speed in Appendix B. Figure 2.2 depicts the expression schemes used for the compressor and turbine maps.

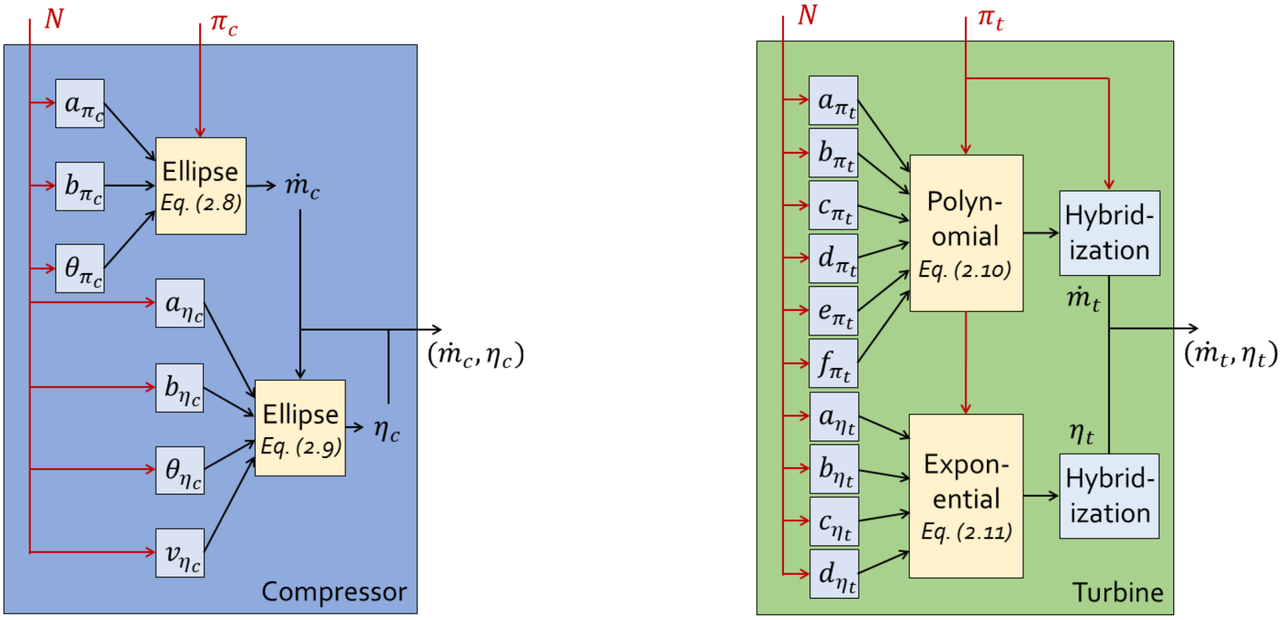

(a) Compressor map expression (b) Turbine map expression

Figure 2.2: Schemes utilized for the expression of performance maps. The reduced mass flow rate ($\dot{m}$) and the isentropic efficiency (η) are expressed as functions of the rotating speed (N) and of the pressure ratio (π). Graphical representation inspired from [60].

2.3.1 Constructed compressor map

The obtained compressor map is depicted in Fig. 2.3. The surge and choke lines are modelled as functions of the reduced speed with piece-wise definitions (cubic-splines). The vertical lines are obtained numerically when choking conditions are detected. The iso-reduced speed lines in the regions with non-uniqueness of the solution were obtained thanks to manipulations on the guess values.

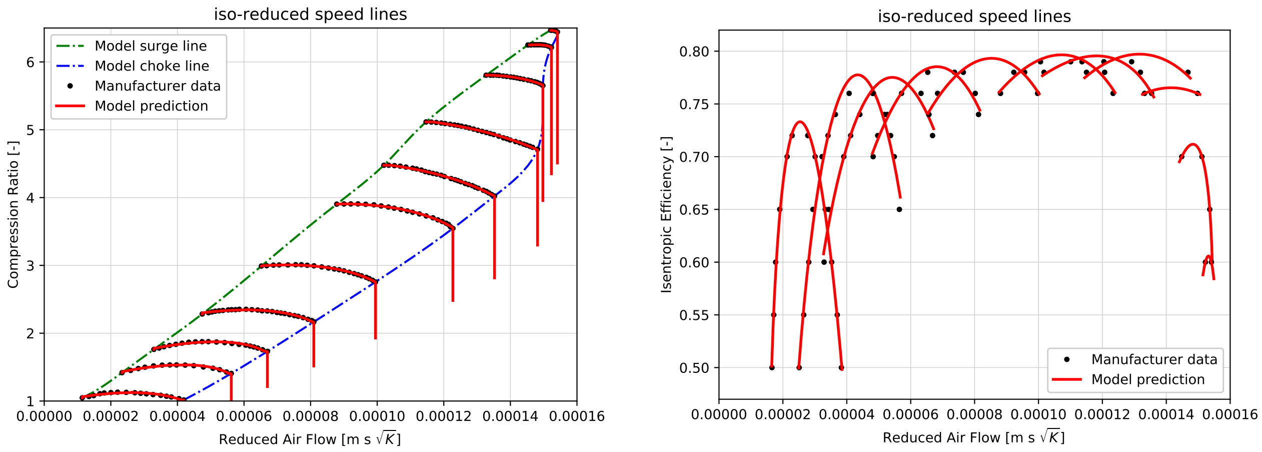

(a) Reduced mass flow

(b) Isentropic efficiency

Figure 2.3: Expression of the compressor reduced mass flow and isentropic efficiency.

The corresponding fitting error for the compressor mass flow rate and isentropic efficiency is plotted in Fig. 2.4. This root mean square error (RMSE) between the predicted (*pred*) and the

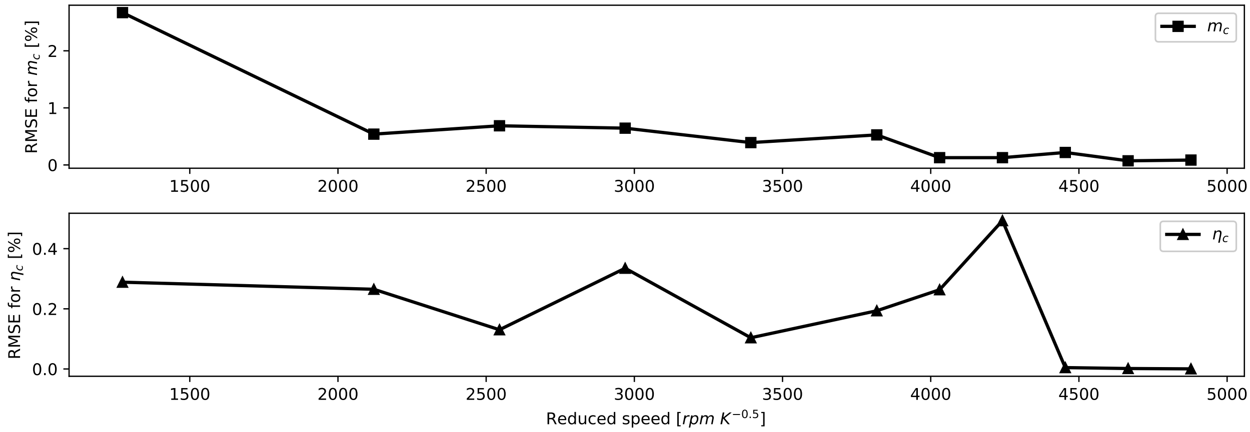

Figure 2.4: Fitting errors for the different sampled speeds of the compressor map. *Top*: RMSE for air flow rate. *Bottom*: RMSE for isentropic efficiency.

reference sampled (ref) points is defined as

$$RMSE = \sqrt{\frac{\sum_{i=1}^{n}\left(\frac{x_{i,ref}-x_{i,pred}}{x_{i,ref}}\right)^2}{n}}\,, \tag{2.12}$$

for each sampled iso-reduced speed line. Two observations can be drawn about this. First, looking at the mass flow, the RMSE is increasing for lower speeds. A simple explanation lies in the fact that a same absolute error on the reduced flow rate (e.g. $err. = 5e^{-6}[ms\sqrt{K}]$) leads to a higher (resp. lower) relative error for a lower (resp. higher) reference mass flow (e.g. 25% for $\dot{m}_{c,ref} = 2e^{-5}[ms\sqrt{K}]$ and 5% for $\dot{m}_{c,ref} = 10e^{-5}[ms\sqrt{K}]$). An additional explanation can be found in the shape of the sampled data at lower speeds: it is less likely to be accurately captured by an elliptical pattern than the higher speed samples. As a second observation, for the curves with very few sampled points (for both mass flow and efficiency), the error is smaller. This is particularly visible for the isentropic efficiency a the three last speeds: the two or three points are almost perfectly interpolated, leading to a quasi-zero error.

2.3.2 Constructed turbine map

Looking closer at the turbine map depicted in Fig. 2.5, it can be observed that the polynomial (Fig. 2.5a) and the exponential (Fig. 2.5c) lead to unrealistic extrapolations for certain ranges of speeds and expansion ratios. A hybridization was introduced to overcome this: at the bounds of the ranges of speeds and pressure ratios with a poor extrapolation, the predicted points are connected with straight lines. This operation is represented with the blocks "Hybridization" in Fig. 2.2b. The results of the hybridization process are plotted in Fig. 2.5b & 2.5d. As an undesired consequence, in the low speed region, the modelled isentropic efficiency is under-evaluated.

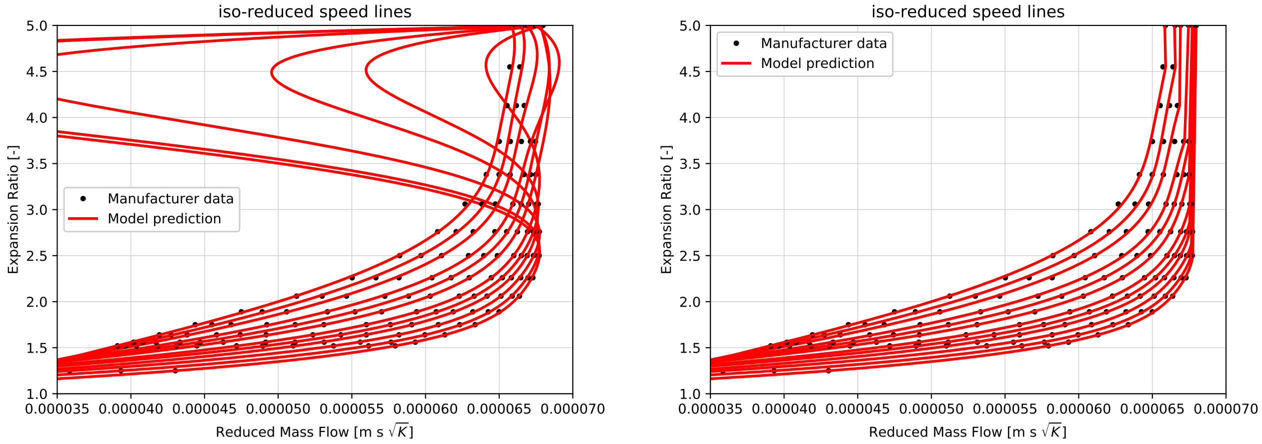

(a) Non-hybridized reduced mass flow (b) Hybridized reduced mass flow

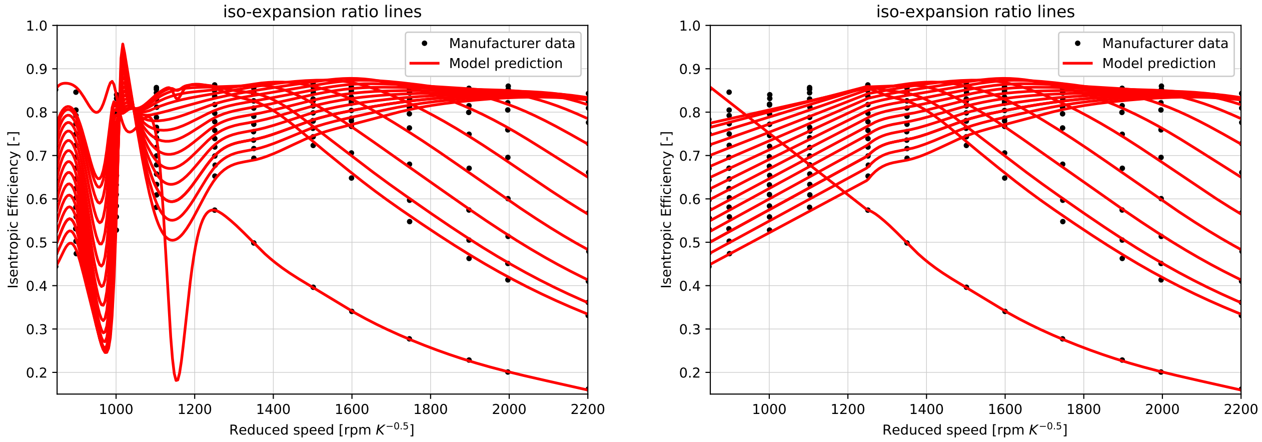

(c) Non-hybridized isentropic efficiency (d) Hybridized isentropic efficiency

Figure 2.5: Expression of the turbine reduced mass flow and isentropic efficiency before and after hybridization.

The corresponding fitting error for the turbine mass flow rate and isentropic efficiency is plotted in Fig. 2.6. The polynomial achieves an excellent fitting for the mass flow, resulting in an extremely low error compared to the other fits. However in the high speed region, specifically for expansion ratios (ER) ranging in $ER \in [3, 4.5]$, the model tends to slightly misevaluate the mass flow. In the choking region, the large thickness of the choke line is due to the distribution of the reference points at $ER = 5$ over a range of different mass flows. This is the result of a difficult and slightly inaccurate sampling of the manufacturer map. Concerning the turbine isentropic efficiency, the hybridization process with straight lines results in a higher error at low speeds, as expected.

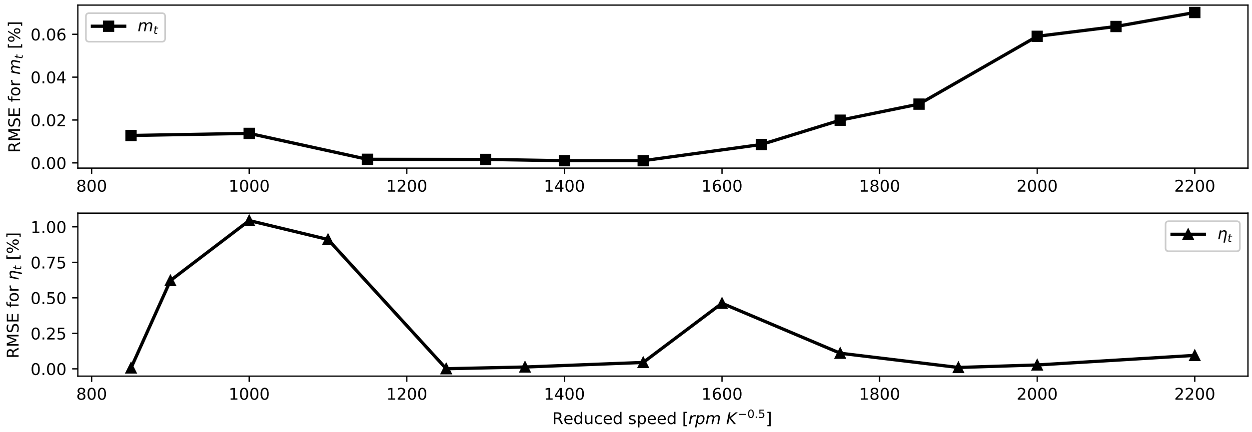

Figure 2.6: Fitting errors for the different sampled speeds of the turbine map. *Top*: RMSE for mass flow rate. *Bottom*: RMSE for isentropic efficiency.

2.3.3 Concluding remarks

The fitting procedure for the T100 maps is summarized in Table 2.2. The global accuracy of each fitting method is evaluated with the average fitting error ($RMSE_{av}$) defined as

$$RMSE_{av} = \sqrt{\frac{\sum_{j=1}^{N} RMSE_j^2}{N}}\ , \tag{2.13}$$

where N is the number of iso-speed lines.

Variable	**Pattern**	**Eq.**	**Map**	**Fig.**	**# coef.**	$RSME_{av}$ [%]
$\dot{m}_{c,red}$	Ellipse	(2.8)	π_c vs $\dot{m}_{c,red}$	2.3a	3	0.896
$\eta_{is,c}$	Ellipse	(2.9)	$\eta_{is,c}$ vs $\dot{m}_{c,red}$	2.3b	4	0.242
$\dot{m}_{t,red}$	Poly.	(2.10)	π_t vs $\dot{m}_{t,red}$	2.5b	6	0.034
$\eta_{is,c}$	Exp.	(2.11)	$\eta_{is,t}$ vs $N_{t,red}$	2.5d	4	0.459

Table 2.2: Summary and evaluation of map fitting methods.

As for a quick comparison, Tsoutsanis et *al.* [60] used similar methods for the GE-LM2500 compressor performance map. They obtained a 2.9% error for the mass flow (exact same fitting pattern) and a 0.41% error for the isentropic efficiency (one additional coefficient in the elliptical fitting pattern).

It turns out that an evident correlation exists between the number of coefficients utilized by the fitting patterns and the average fitting error. This suggests that the fitting quality could be further improved by increasing the number of coefficients of each fitting pattern. In fact, the initial idea in this work was, for the compressor maps, to use super-elliptical curves defined as

$$\left|\frac{(x-u)\cos\theta+(y-v)\sin\theta}{a}\right|^c+\left|\frac{(x-u)\sin\theta-(y-v)\cos\theta}{b}\right|^c=1\,, \tag{2.14}$$

which offer 6 degrees of freedom in total. Experience revealed that the optimization process with the *curve_fit* function and super-elliptical curves was a difficult task, requiring developer's efforts for the bounding of the 6 coefficients. Within the context of this thesis, aiming at the development and the validation of a dynamic simulation tool for mGT's, it has been decided to not further investigate the fitting techniques because of the current satisfactory results.

CHAPTER 3

PHYSICAL MODEL

In this Chapter, the model developed to simulate the dynamic behavior of micro gas turbines is presented. The modelling approach and assumptions are thoroughly discussed, and the governing equations for the global mGT system are presented. Although concentrating essentially on the physical aspects, some precautions related to the numerical model are also addressed. The latter have to do to with its implementation and with the global model complexity.

A model is intrinsically related to numerous assumptions, as well as to its numerical implementation. For this reason, Section 3.1 first presents the adopted modelling methodology. Sections 3.2 to 3.7 then describe the modelling of each mGT component and represent them with a *block* illustration (i.e. *black-box* representation). Section 3.8 finally summarizes the global mGT model. The subscripts utilized along this Chapter refer to the thermodynamic cycle represented in Fig. 1.1 (see Section 1.1.1).

3.1 Methodology

The development of off-design models starts with the identification of the systems dominant phenomena. In a mGT, these phenomena are represented with the thermodynamic cycle. One can list the compression (*compressor block*), the heat recovery (*recuperator block*), the combustion (*combustor block*) and the expansion (*turbine block*). Because of its high rotating speed and its role as connector between the main components, the dynamics of the shaft is also an important parameter for a mGT model (*shaft block*). Adding to that the control system (*controller block*), which plays a major role in the mGT regulation, a total of *six modules* necessary for the mGT modelling are identified.

This decomposition into different modules is an asset for the numerical tool modularity requirement. However, some physical considerations are still required before the model construction.

3.1.1 Physical considerations

The dominant phenomena taking place in a mGT were listed above. However, undesired phenomena, such as heat and pressure losses, also occur in the system. Therefore, the modelling of these phenomena inside each component will be discussed for the six modules that were identified.

Neglecting heat and pressure losses in additional components

Heat and pressure losses also arise at several other locations in the system (e.g. pressure loss at the air inlet filter, heat and pressure losses in the tubing), impacting the global machine behavior. Nevertheless, in order to limit the global model complexity, it is decided not to model them in this work. If it turns out that this simplification severely impacts the model accuracy, this will be addressed during the validation and improvements will be suggested.

Neglecting mass and energy accumulation in additional components

Some considerations related to the dynamic aspects of mass and energy accumulation also need to be discussed. Although neglecting pressure and heat losses in components such as pipes can be justified with magnitude order comparisons, the mass and thermal energy accumulation inside these components is physically non-negligible (e.g. the pipes volume is much larger than the compressor and turbine volumes, as reported by Fig. 1.5). One can therefore expect the absence of models for the components that do not directly take part to thermodynamic cycle to cause modelling inaccuracies during transients. However, this will also be discussed during the validation.

Total quantities and low Mach number assumption

Additional assumptions are brought on the physical quantities. In order to relax the model complexity, the difference between static and total values of the thermodynamic quantities is neglected. This assumption is supported for many mGTs by the fact that the flow velocities are kept below a Mach number of 0.3 to minimize pressure losses outside turbomachinery parts [5]. Also, the gases are considered as semi-ideal: they are supposed to have a variable specific heat capacity with the temperature and pressure and to follow to the ideal gas law.

Introduction of the thermodynamic tables

The thermodynamic and chemical tables utilized in this model should also be introduced at this stage. The developed tool has integrated an entire *module* where thermodynamic functions (e.g. specific energy, enthalpy, heat capacities, ...) are defined, allowing to account for the molar composition of the mixture in each stream. Their generic definition makes them convenient for being used everywhere in the model while the utilized reference tables can be switched easily from the *thermodynamic module*.

Currently, `thermo 0.2.6` [77] is used to obtain the mixtures specific gas constants (R^*) and molar masses (MM) while `CoolProp` [78] is used for all the other thermodynamics quantities. Humid air treatment was not implemented into the model. Assuming the presence of H_2O in ambient air therefore leads to a misevalutaion of the gas heat capacity, since the model takes water to be liquid in ambient conditions.

3.1.2 Numerical considerations

Among the power plants dynamics models proposed in the literature, many of them are constructed with graphical programming environments, specifically developed for the aim of modelling dynamic systems (e.g. in the `Simulink` environment based on the `MATLAB` language or in the `Dymola` environment using the `Modelica` language) [79]. Their interfaces with graphical block diagramming tools allow to structure the program very intuitively according to the thermodynamic cycles.

Some of the main advantages that come with these environments are the relaxation of the programmer's efforts for the model implementation, as well as the relative abstraction offered regarding the numerical solving schemes. Let us also note that the possibility to formulate the models both in temporal and frequency domains (i.e. transfer function) makes them particularly convenient for the implementation of control systems.

Mathematical formulation for `Python` implemenation

As stated in Chapter 1, it has been decided for this work to develop the current model in the `Python` open-source programming language. `Python` has a wide variety of multi-purposes libraries and frameworks, among which the *SciPy* ecosystem, which provides a large set of mathematical, scientific, and engineering numerical tools [76]. *SimuPy* is an even more specific framework, itself utilizing *SciPy*, for simulating interconnected dynamical system models, that has been developed starting from 2017 by Benjamin W. L. Margolis at the University of California[1] [81].

Despite *SimuPy* offers an appropriate framework for the development of dynamic models, its low maturity level and very limited use in the literature (so far limited to the author's publications, to our knowledge) played against it. Instead, a new framework was developed in the *SciPy* environment for this work, as explained in Chapter 4. The numerical solvers of *SciPy* (e.g. *fsolve*, *odeint*) can solve linear and non-linear systems of equations. Therefore, the physical model developed in the following Sections will define a set of state variables necessary to build a non-linear system of equations. The constructed model will consequently be expressed with the following state-space format,

$$\frac{dx(t)}{dt} = \begin{bmatrix} f_1(t, x(t), u(t), d(t)) \\ \dots \\ f_i(t, x(t), u(t), d(t)) \\ \dots \\ f_n(t, x(t), u(t), d(t)) \end{bmatrix}, \quad x(t) = \begin{bmatrix} x_1(t) \\ \dots \\ x_i(t) \\ \dots \\ x_n(t) \end{bmatrix}, \quad d(t) = \begin{bmatrix} p_{amb}(t) \\ T_{amb}(t) \\ P_{dem}(t) \end{bmatrix}, \quad u(t) = \begin{bmatrix} \dot{m}_f(t) & P_{load}(t) \end{bmatrix},$$

where $x(t)$ is the vector of state variables, $f(t, x(t), u(t), d(t))$ the non-linear state equations, $d(t)$ the vector of disturbance variables and $u(t)$ the vector of input variables. The choice of the disturbance and input variables, which are presented in the above system, will be justified throughout this Chapter.

3.2 Compressor block

The modelling of the compressor performances was presented in Chapter 2. The role of the compressor block, as part of the global mGT model, is to provide the compressed air temperature. The model must also handle the computation of the air flow rate at the compressor outlet. The power required to the drive compressor should also be computed inside this block, based on the two previous quantities.

The compressor black-box model and its input and output variables are represented in Fig. 3.1 and is explained within this Section.

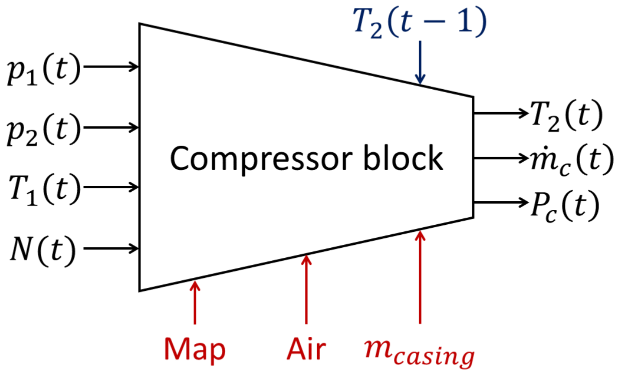

Figure 3.1: Compressor block input and output variables.

---

[1] current affiliation: Systems Analysis Office, NASA Ames Research Center [80]

3.2.1 Computation of the air flow rate

Because performance maps represent static conditions, a semi-steady state assumption must be introduced here to obtain the air flow rate. This assumption is that the fluid inertia can be neglected inside the compressor control volume. This is supported by the quite important fluid velocity and by the small compressor volume compared to the flow velocity.

With this assumption, the mass and energy conservation equations return to a steady-sate form. Therefore the air flow rate can be calculated using the quasi-steady assumption at each time step [5, 24, 51].

The compressor air flow rate is obtained for a given compressor angular speed (ω) and compression ratio (π_c) with a lecture of the map, as

$$\dot{m}_c = f_{map}(\pi_c, N_{red})\frac{p_1}{\sqrt{T_1}} = f(p_1, T_1, p_2, \omega)\ , \tag{3.1}$$

where N_{red} represents the reduced speed introduced in Table 2.1.

$$N_{red} = \frac{60\omega}{2\pi\sqrt{T_1}} \tag{3.2}$$

The decision of neglecting mismatches between the inlet and outlet mass flows (i.e. no mass accumulation inside the control volume) is also motivated by the relatively low compressor volume (V_c) compared to the volume of the discharge duct (V_{duct}) connected to the recuperator. Assuming $V_{duct} = 100 \cdot V_c$ (reasonable assumption w.r.t. Fig. 1.5), the mass conservation,

$$\frac{d\rho}{dt} = \frac{1}{V}(\dot{m}_{in} - \dot{m}_{out})\ , \tag{3.3}$$

gives a 100 times smaller time constant for the compressor outlet density. Adding a mass conservation equation for the compressor would consequently complexify the model without significantly improving its accuracy.

3.2.2 Compressor outlet temperature and power

The compressor is modelled as an adiabatic component. Therefore, no heat losses are taken into account in this work. This is motivated by the limited knowledge that we have about them and by their supposed relatively low importance compared to the error made on other variables (e.g. compressor isentropic efficiency and air flow rate obtained with the maps model).

Constitutive equations

Assuming air to be a perfect gas, and taking advantage of the isentropic model used to express the performance maps, the compressed air temperature ($T_{air,comp.}$) can be computed. First, the isentropic temperature is evaluated with

$$T^{is}_{air,comp.} = T_1 \pi_c^{\gamma_a}\ , \tag{3.4}$$

where π_c is the compression ratio and γ_a the isentropic exponent of air. Then, the definition of the compressor isentropic efficiency ($\eta_{c,is}$) is used to derive the compressed air specific enthalpy as below.

$$h_{air,comp.} = h_1 + \frac{h^{is}_{air,comp.} - h_1}{\eta_{c,is}} \tag{3.5}$$

Finally, $T_{air,comp.}$ is obtained with the thermodynamic table, as represented below.

$$T_{air,comp.} = f(h(p_2, T_{air,comp.})) \tag{3.6}$$

The latter must be computed iteratively in order to match the temperature to the corresponding specific enthalpy. The intermediate variables used in Eq. (3.4) & (3.5) are defined as

$$\eta_{c,is} = f_{map}(\pi_c, N_{red}) \qquad \gamma_a = \frac{\kappa_a - 1}{\kappa_a} \qquad \kappa_a = \frac{\overline{c}_{p,a}(T_1, T_{air,comp.})}{\overline{c}_{v,a}(T_1, T_{air,comp.})}\ , \tag{3.7}$$

where $\overline{c}$ is the average specific heat capacity. Because γ_a is a function of T_1 and $T_{air,comp.}$, iterations must be made between Eq. (3.4), (3.5) & (3.6) such that convergence is reached for $T_{air,comp.}$.

Model simplification

The increased complexity due to the iterative procedure is a serious concern, especially because the turbine block will require a similar expansion model.

With the aim of developing an efficient dynamic model for mGTs, a small degradation of the model accuracy could be tolerated, provided that it translates to a significant complexity reduction. One can therefore introduce a simplified model and compare its performances with the model using the isentropic efficiency definition, described above.

With the same assumption that air is a perfect gas, the compressed air temperature can obtained as

$$T_{air,comp.} = T_1 \left(1 + \frac{1}{\eta_{c,is}} \left(\pi_c^{\gamma_a} - 1\right)\right)\ , \tag{3.8}$$

with γ_a defined as

$$\gamma_a = \frac{\kappa_a - 1}{\kappa_a} \qquad \kappa_a = \frac{c_{p,a}(T_1)}{c_{v,a}(T_1)}\ , \tag{3.9}$$

where it is a function of the inlet temperature only. The same approach has been chosen by many authors [18, 49, 55, 82]. With this simplified model, no iteration is required, which makes it very competitive with the definition, despite its lower accuracy.

The error involved with such simplification was evaluated to about 10^oC for typical mGT compression ratios (i.e. $\pi_c = 4.5$). To compensate this relatively important deviation during dynamic simulations, the possibility of computing an average γ_a, based on the compressed air temperature from the previous time step, will be addressed in Section 5.2.2.

However, it should be emphasized that, for the model validation with experiments, the error made on the evaluation of the actual compressor isentropic efficiency and air inlet temperature can have a more significant impact than the one induced with this simplification on γ_a.

Integration of heat transfer and dynamic aspects

In order to account for the thermal capacitance of the compressor, the heat transfer between the compressed air and the compressor casing should be integrated to the model. For that purpose, it can be assumed that the compressor outlet temperature (T_2) is equal to a virtual casing temperature (T_{casing}). When applying the energy conservation to the casing (i.e. difference between input and output thermal energy within the compressed air stream), one obtains the evolution of T_2 over time as

$$\frac{dT_2}{dt} = \frac{\dot{m}_c(h(p_2, T_{air,comp.}) - h(p_2, T_2))}{m_{cas,comp.} c_{casing}}\ , \tag{3.10}$$

where $m_{cas,comp.}$ and c_{casing} represent the casing mass and specific heat capacity. These variables will be calibrated in Section 5.1.2. The advantage coming with this simplification on the compressor outlet and virtual casing temperatures is to get rid of any heat transfer coefficient.

However, it should be emphasized that this casing temperature is qualified as virtual because it does not correspond to any physical quantity (i.e. the casing temperature is not uniform in reality).

Power computation

With the air flow rate computed in the previous subsection and the compressed air temperature obtained here above, the mechanical power required to drive the compressor is defined with the specific enthalpy as below.

$$P_c = \dot{m}_c(h(p_2, T_{air,comp.}) - h(p_1, T_1)) \tag{3.11}$$

3.3 Combustor block

The combustor block is used to represent two phenomena. First, as suggested by its name, it models the combustion process where heat is released. Secondly, because of its relatively large volume compared to other components, it acts as a mass and energy accumulator for the streams.

Although evaluating pollutant emissions brings extremely interesting information, because of the modelling complexity this involves, the current dynamic model is not intended to do so.

Figure 3.2 illustrates the black-box model that is constructed for the combustion chamber in this Section.

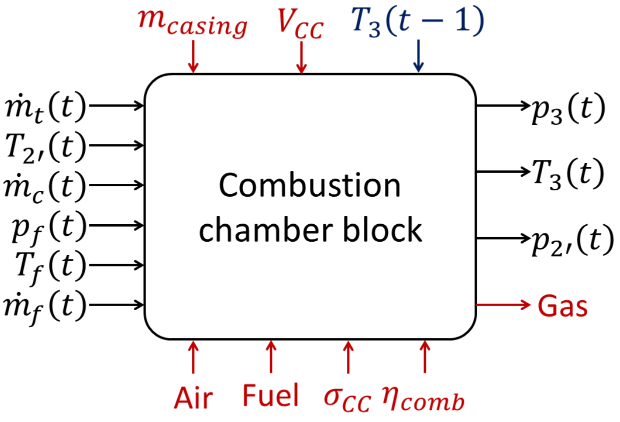

Figure 3.2: Combustion chamber block input and output variables.

3.3.1 Combustion process

The first goal of the combustion model is to predict the rate of heat released by the fuel ignition. Because they are non-negligible (i.e. often assumed to amount at about 5% of the total input heat [11]), the heat losses must be modelled as well in this block [6]. Secondly, the model should also predict the flue gas composition (i.e. limited to the dominant species), later needed to evaluate the stream specific heat capacities.

Phenomenology in reverse-flow CAN-type combustors

Combustions are complex phenomena coupling fluid mechanics and chemical kinetics concepts. Fortunately, CFD analyses bring precious information on the process. Works conducted by Calabria et *al.* [4, 29] and Cameretti et *al.* [26] provide, for example, advanced results in terms of combustion performances (i.e. combustion efficiency and pollutant formation).

Based on CFD analyses, Figure 3.3 was constructed to illustrate the typical combustion scheme in a reverse-flow CAN-type mGT combustor [29]. The air leaving the recuperator first enters the annulus between the inner and outer flame tubes where it is pre-heated thanks to a counter-flow heat transfer with the high-temperature flue gas of the inner flame tube. The combustion is initiated by a diffusive flame located at the fuel injection pilot line while the main process takes place inside the inner flame tube with premixed flames generated by the main injection line [29]. The fuel split (i.e. ratio of the main to the pilot fuel mass flow rate)

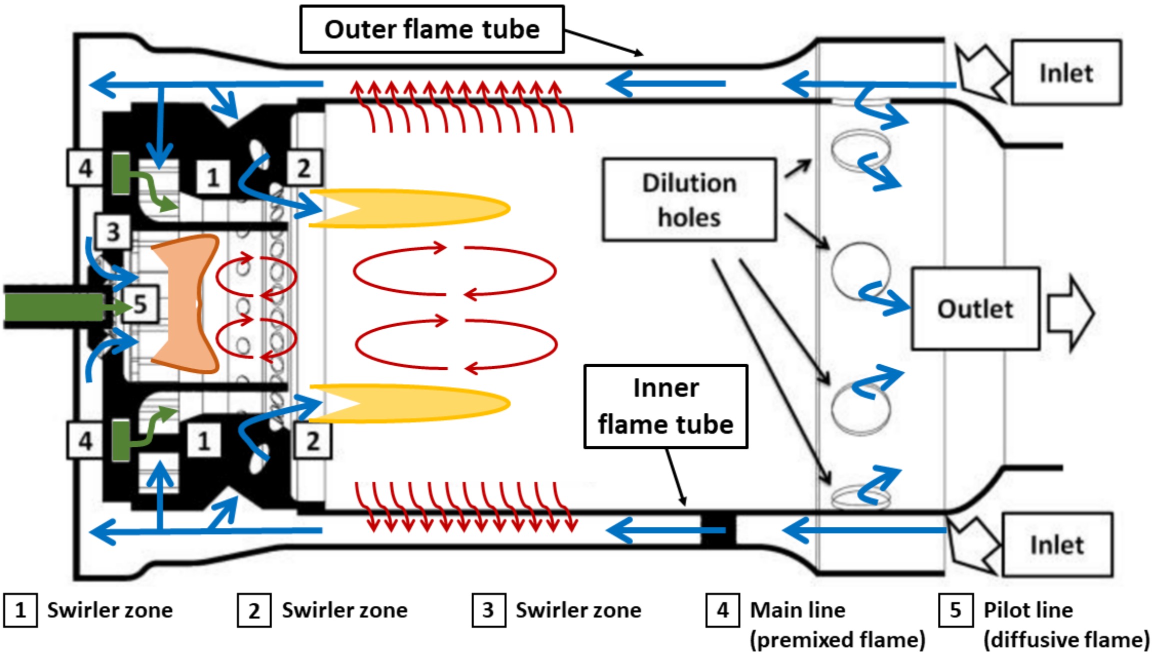

Figure 3.3: 2D visualization of a reverse-flow CAN-type mGT combustor originally constructed by [29]. Indications on mass and heat flows were derived from the CFD results obtained for the temperature and fluid velocity distributions with natural gas fuelling.

when the machine runs at full load is typically about 10 [83]. Dilution holes are used to reduce the average flue gas temperature to acceptable values for the turbine.

Selection of the combustion model

Despite the fact that models using simplified kinetics schemes[2] have already been applied in mGT steady state $1D$ models [17], the validity of the results they provide in $0D$ time-dependent models with regard to the complexity of the actual phenomena in a $3D$ combustor remains limited. Although a careful application of these kinetics models can increase their results accuracy[3], the limited positive impact of these models is counter-balanced by the increased complexity they involve. In fact, variables such as the residence time or the temperature profile remains very difficult to evaluate in dynamic models, hence limiting the kinetics schemes accuracy.

Therefore, a quasi-steady state single-step model assuming complete combustion of an homogeneous air/fuel mixture is selected here. The fuel oxidation in dry air (i.e. composed of N_2, O_2 and Ar only) is written as

$$\begin{aligned} nC_cH_h + n_{O_2}O_2 + n_{N_2}N_2 + n_{Ar}Ar \Longrightarrow \\ ncCO_2 + \left(\frac{nh}{2}\right)H_2O + \left(n_{O_2} - nc - \frac{nh}{4}\right)O_2 + n_{N_2}N_2 + n_{Ar}Ar \ , \end{aligned} \tag{3.12}$$

where C_cH_h represents any alkane present in the air/fuel mixture. Non-alkanes fuels (e.g. H_2) are here assumed to be non-reactive, and they are consequently treated as chemically inert species (i.e. like N_2 and Ar are). The present model can consequently be used to evaluated the flue gas composition obtained by the oxidation of fuels with dominating alkanes contents only.

---

[2] like the 8-steps mechanisms proposed by Novosselov et *al.* for natural gas [84]

[3] such as made by Renzi et *al.* with the `GRI-Mech 3.0` library to study the impact of syngas fuelling in a mHAT [17]

Quantification of the heat release

The rate of heat released by the combustion is evaluated with the fuel flow rate and its lower heating value (LHV). In order to account for combustion inefficiencies and heat losses, an efficiency parameter $\eta_{comb.}$ is introduced and the rate of heat release is modelled as

$$\dot{Q}_{comb.} = \eta_{comb.}\dot{m}_f LHV \ , \tag{3.13}$$

where $\dot{m}_f$ is the fuel flow rate.

3.3.2 Mass and energy conservation

Assuming that the volume occupied by the flue gas inside the combustor is constant, the control volume approach can be utilized to establish mass and energy conservation of the gas inside the combustion chamber. A complete description of this methodology is provided in Appendix C. In the case of the combustor, the boundary inlet and outlet conditions are represented in Fig. 3.4. The inlet conditions are (1) the mass flow rate, (2) the pressure and (3) the temperature, all utilized to compute the heat flow carried by both the incoming fuel and the preheated air. The outlet conditions are the pressure, temperature and flow rate, necessary to compute the flue gas heat flow. The heat losses are also taken into account in the outlet conditions. With this model, one assumes that the combustion process takes place inside the control volume. Because of the considerations presented in Appendix C, it is also assumed that the internal pressure is uniform, despite the actual inhomogeneity involved by the complex flow [51].

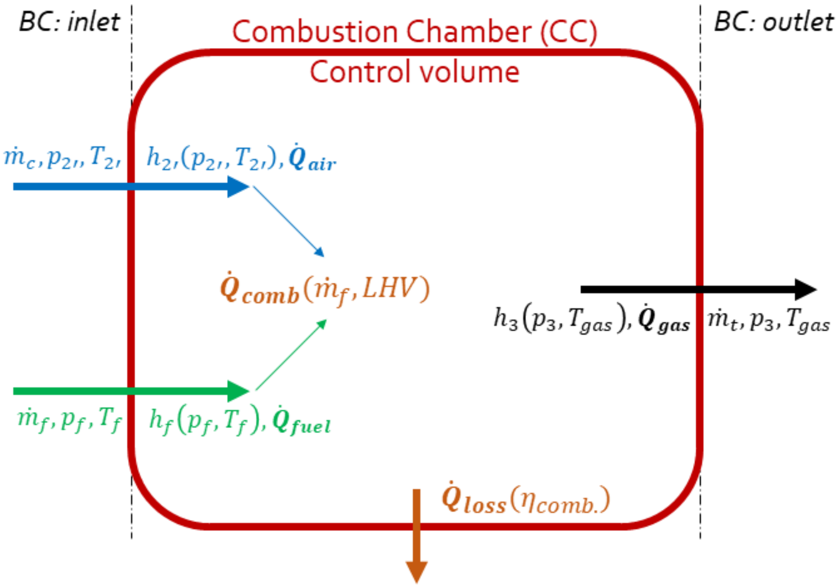

Figure 3.4: Illustration of the control volume and boundary conditions representing the combustion chamber.

Formulation of the mass and energy conservation equations

With the boundary conditions introduced in Fig. 3.4, the mass conservation equation applied to the combustor can be written as

$$\frac{d\rho_3}{dt} = \frac{1}{V_{comb}}(\dot{m}_c + \dot{m}_f - \dot{m}_t) \ , \tag{3.14}$$

where V_{comb} represents the combustion chamber volume (calibrated in Section 5.1.3) and ρ_3 the flue gas outlet density. The energy conservation equation is written as

$$\frac{du_3}{dt} = \frac{1}{\rho_3 V_{comb}}(\overbrace{\dot{m}_c h_{2'}}^{\dot{Q}_{air}} + \underbrace{\dot{m}_f(h_f + \eta_{comb.}LHV)}_{\dot{Q}_{fuel} + \dot{Q}_{comb} - \dot{Q}_{loss}} - \overbrace{\dot{m}_t h_3}^{\dot{Q}_{gas}} - u_3(\dot{m}_c + \dot{m}_f - \dot{m}_t)) \ , \tag{3.15}$$

where h is the specific enthalpy at the different boundaries (obtained with the corresponding pressures and temperatures) and u_3 the specific energy of the flue gas leaving the chamber.

The combustion inefficiencies and heat losses are taken into account with the efficiency $\eta_{comb.}$, that will be calibrated in Section 5.1.3.

Among the dynamic models proposed in the literature, some neglect the energy term $u_3(\dot{m}_c + \dot{m}_f - \dot{m}_t)$. Although this simplification has no impact on the steady sate results, it does not respect the exact dynamics of the energy conservation, as it has been highlighted by Henke et *al.* [5] and proven in Appendix C.

The pressure and temperature at the combustor outlet (i.e. intensive variables) can be extracted from the state variables ρ_3 and u_3 by solving the following system of equations,

$$\begin{cases} p_3 - \rho_3 R T_{gas} & = 0 \,, \\ u_3 - u_{database}(p_3, T_{gas}) & = 0 \,, \end{cases} \tag{3.16}$$

which uses the ideal gas law assumption for ρ_3 and the thermodynamic tables for u_3.

Heat transfer with the combustor casing and dynamic aspects

Similarly to the compressor, the thermal capacitance of the combustor casing can be taken into account by assuming that the turbine inlet temperature (T_3) is equal to a virtual casing temperature (T_{casing}). The energy conservation applied to the casing is written as

$$\frac{dT_3}{dt} = \frac{\dot{m}_t(h(p_3, T_{gas}) - h(p_3, T_3))}{m_{cas,comb.} c_{casing}} \,, \tag{3.17}$$

where $m_{cas,comb.}$ and c_{casing} represent the casing mass and specific heat capacity (also calibrated in Section 5.1.3).

Model for the pressure losses

Experimental analyses have shown that the combustor is the component across which the pressure losses are the strongest (i.e. usually evaluated to $5-6\%$ relative pressure losses) [6, 83].

Although the modelling of the actual physical phenomenon is rather difficult because of the complex reverse flow development, the pressure losses can be modelled with

$$p_3 = \sigma_{comb} p_{2'} \,, \tag{3.18}$$

where σ_{comb} is an artificial pressure losses coefficient that will be calibrated in Section 5.1.3.

Let us finally mention that the auxiliary compressor used to increase the fuel pressure level is not modelled here. However, its power consumption will be taken into account through the auxiliaries in Section 3.6.

3.4 Turbine block

The turbine model is very similar to that of the compressor and the turbine performances were also introduced in Chapter 2. This Section therefore only reports the model, since the discussion around it was made in Section 3.2.

The turbine black-box model and its input and output variables are represented in Fig. 3.5.

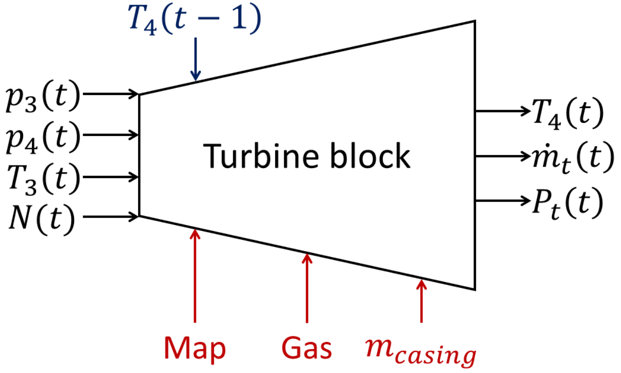

Figure 3.5: Turbine block input and output variables.

3.4.1 Computation of the flue gas flow rate

The flue gas flow rate is obtained for a given turbine angular speed (ω) and expansion ratio (π_t) with a lecture of the map, as

$$\dot{m}_t = f_{map}(\pi_t, N_{red})\frac{p_3}{\sqrt{T_3}} = f(p_3, T_3, p_4, \omega)\ , \tag{3.19}$$

where N_{red} represents the reduced speed introduced in Table 2.1.

$$N_{red} = \frac{60\omega}{2\pi\sqrt{T_3}} \tag{3.20}$$

3.4.2 Turbine outlet temperature and power

The turbine is modelled as an adiabatic component for the same reasons as for the compressor. Assuming that the flue gas is a perfect gas, the expanded flue gas temperature ($T_{gas,turb.}$) is obtained as

$$T_{gas,turb.} = T_3\Big(1 - \eta_{t,is}\Big(1 - \pi_t^{-\gamma_g}\Big)\Big)\ , \tag{3.21}$$

where $\eta_{t,is}$ and γ_g are defined as

$$\eta_{t,is} = f_{map}(\pi_t, N_{red}) \qquad \gamma_g = \frac{\kappa_g - 1}{\kappa_g} \qquad \kappa_g = \frac{c_{p,g}(T_3)}{c_{v,g}(T_3)} \tag{3.22}$$

The same reasoning as for the compressor holds for the turbine thermal capacitance. The evolution of the turbine outlet temperature (TOT or T_4) over time is given by

$$\frac{dT_4}{dt} = \frac{\dot{m}_t(h(p_4, T_{gas,turb.}) - h(p_4, T_4))}{m_{cas,turb.}c_{casing}}\ , \tag{3.23}$$

where $m_{cas,turb.}$ and c_{casing} are the casing mass and specific heat capacity (calibrated in Section 5.1). The mechanical power generated by the turbine is defined with the enthalpy as

$$P_t = \dot{m}_t(h(p_3, T_3) - h(p_4, T_{gas,turb.}))\ , \tag{3.24}$$

with $\dot{m}_t$ the flue gas flow rate computed in the previous section and $T_{gas,turb.}$ the expanded flue gas temperature obtained here above.

3.5 Recuperator block

The recuperator is an essential component to improve the mGT efficiency by preheating the compressed air thanks to heat recovery from the turbine exhaust gas. It typically increases the electrical efficiency from $16 - 20\%$ to about 30% [2]. Nevertheless, because of its massiveness and metallic nature, both associated to a high thermal capacitance, the lag in its temperature response during transients confers him the slowest dynamics of the system [85]. It is therefore of particular interest to accurately model it, because the lag it involves influences the mGT dynamic behavior [86].

This Section first resumes previous works conducted to characterize the T100 recuperator (used as reference for other mGT recuperators). That part is intended to familiarize the reader with the typical off-design performances of the component and to give an insight of the model requirements. An efficient model describing transients in recuperators with a low computational complexity is then presented. This model is thereafter discussed against other similar models reported in the literature.

3.5.1 Characterization of the T100 recuperator

As presented in Chapter 1, the T100 recuperator is a primary-surface recuperator with a cross-corrugated (CC) duct configuration (see Fig. 3.6a) and it is of mixed counter- and cross-flow type (see Fig. 3.6b). It is composed of 390 air cells in total (hydraulic diameter $D_h < 1.5[mm]$) and its matrix is made up of thin stainless-steel plates (thickness $< 0.15[mm]$) with good high temperature mechanical and corrosion properties, but limiting its maximum inlet temperature to 645^oC [2, 36]. Its compactness is over $1600[m^2/m^3]$ which makes it a "compact recuperator" [36].

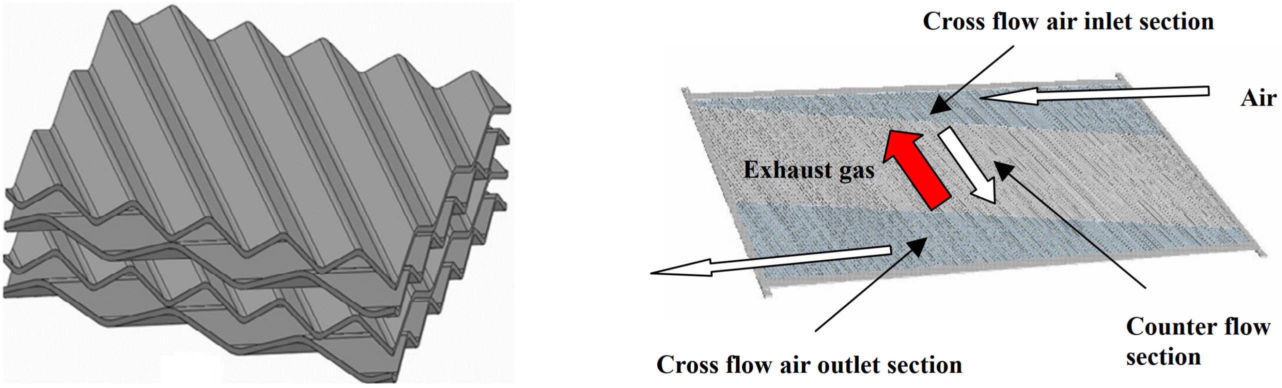

(a) Schematic of the cross-corrugated (CC) surface.

(b) Laser welded air cell with stamped primary heat transfer surface.

Figure 3.6: Surface and flow configurations of the T100 recuperator. Dimensions of air cells are 295x420x2.22$[mm]$. Figures are taken from [2] (*left*) and from [36] (*right*).

Since a recuperator is designed to maximize the heat transfer while limiting the pressure losses across it, the two metrics commonly used to characterize it are (1) the effectiveness (ϵ), defined as the ratio between the actual and the maximum heat transfer rate,

$$\epsilon = \frac{\dot{Q}}{\dot{Q}_{max}} = \frac{\dot{m}_c c_{p,c}(T_c^{out} - T_c^{in})}{(\dot{m}c_p)_{min}(T_h^{in} - T_c^{in})} = \frac{T_c^{out} - T_c^{in}}{T_h^{in} - T_c^{in}} , \tag{3.25}$$

and (2) the total relative pressure losses (δp), defined as

$$\delta p = \frac{\Delta p_c}{p_c^{in}} + \frac{\Delta p_h}{p_h^{in}} \tag{3.26}$$

Because it is related to the UA value and as it will be used to process experimental results, the number of transfer units (NTU) also needs to be introduced. The NTU,

$$NTU = \frac{UA}{(\dot{m}c_p)_{min}} = \frac{UA}{C_{min}} \ , \tag{3.27}$$

is defined as the ratio between the UA value and the minimum heat capacity rate (C_{min}). For a counter-flow heat exchanger, the relationship between ϵ and NTU is given by

$$\epsilon = \frac{1 - exp[-NTU(1 - C_r)]}{1 - C_r exp[-NTU(1 - C_r)]} \qquad NTU = \frac{1}{C_r - 1} ln\left(\frac{\epsilon - 1}{\epsilon C_r - 1}\right) , \tag{3.28}$$

where

$$C_r = \frac{C_{min}}{C_{max}} = \frac{(\dot{m}c_p)_{min}}{(\dot{m}c_p)_{max}} \tag{3.29}$$

Review of the T100 recuperator effectiveness and pressure losses

Lagerström and Xie [36] worked on the theoretical assessment of the performances of the RSAB recuperator (from Rekuperator Svenska AB, subsidiary company of the VOLVO Technology Transfer Corporation). The latter is designed for a $100kW$ mGT and is usually taken in the literature to be similar to that of the T100 [1, 2, 31, 37, 87]. For a large range of off-design steady state operating points, they concluded that the effectiveness was always superior to 89% whereas the total relative pressure losses were inferior to 4.5%.

Hohloch et *al.* [83] experimentally obtained an effectiveness ranging from 93.1% to 88.8% for electrical powers varying from $66kW$ to $94kW$. The measured maximum total relative pressure losses where about 5.24% (value deduced from the published results).

Ferrari et *al.* [37, 87] also performed experimental analyses of the recuperator in different operating conditions. For a range of power going from $20kW$ to $74.9kW$, they measured with an accuracy of 2% that the effectiveness was bounded between 88.3% and 91.7%. They also reported dynamic results of step responses to load increases from $+10kW$ to $+50kW$, when starting from $0kW$ operating conditions. In terms of transient performances, a time constant of $60s$ for the air outlet temperature was associated to the $+50kW$ step (initial rate of $+2.3K/s$) whereas the observed time constant was $48s$ when the step was $+30kW$ (initial rate of $+1.5K/s$).

Henke et *al.* [6], from the same research team as [83], obtained experimentally very similar results as [37] for the effectiveness.

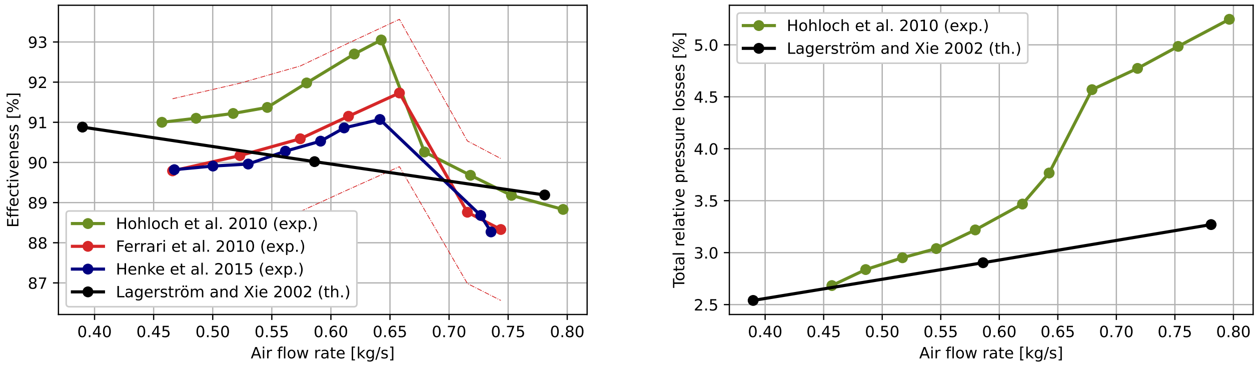

(a) Effectiveness

(b) Pressure losses

Figure 3.7: T100 recuperator performances adapted from the results reported by Lagerström and Xie [36], Hohloch et *al.* [83], Henke et *al.* [6] and Ferrari et *al.* [37]. The dash-dotted lines indicate the range of accuracy of the measurements.

Figure 3.7 reports the different performances deduced from the results published in literature for a range of operating conditions corresponding to about from $20kW$ to $100kW$. In Fig. 3.7a, experimental data illustrate the characteristic effectiveness of recuperators. Understanding the reason for this profile is crucial as mGTs efficiency is highly sensitive to the recuperator effectiveness. In fact, although this observation is widespread, few authors give an explanation to it.

Relation between phenomenology and effectiveness

McDonald [31] interprets the increasing trend of the effectiveness with the air flow rate through the direction of the heat flows inside the recuperator matrix. For very low air flows, the longitudinal conduction of heat in the metallic matrix tends to unify the wall temperature, therefore impacting the effectiveness. When the air flow increases, the heat flow becomes increasingly more normal to it, resulting in an improved effectiveness (i.e. no unification of the wall temperature). In high-compactness heat exchangers (e.g. mGT recuperators), this effect is visible on a wide range of air flows. In the T100 case, the threshold below which the effectiveness has this increasing trend with the air flow is at about $0.65kg/s$ (corresponding to about 80% of the design point air flow). Above this threshold, also corresponding to the maximal effectiveness, the latter starts decreasing.

Henke et *al.* [6] and Hohloch et *al.* [83] partly attribute this to the increasing spatial inhomogeneity of the TOT at the recuperator inlet. Compared to the TOT probed with T100 integrated sensor, the average temperature measured at multiple locations in the recuperator inlet section is about $3K$ higher at full load [6]. The resulting effectiveness, computed with the new average TOT, is 1.25% higher than the one measured with the T100 sensor. Still, although less steep, the decreasing profile remains observable for higher air flows, despite the new average TOT. From experimental analyses, Henke et *al.* [6] assume that recirculation zones at the recuperator hot inlet sections are the cause of the effectiveness deviation, because they would further increase the temperature spatial divergence.

Discussion on the pressure losses

Figure 3.7b stresses that there is no real agreement on the pressure losses in the literature. In fact, few analyses were proposed to evaluate them. Furthermore, [6] highlighted the fact that the relative pressure losses in the cold side of the recuperator were about 2.18% whereas they were evaluated to 3.48% in the duct connecting the compressor outlet to the recuperator. Therefore, this suggests that the model should be calibrated as whole in order to account for piping losses and to match the reference results. Figure 3.7b also reveals that the pressure losses are highly correlated to the air flow. This implies that the model should avoid considering the losses constant on the complete operating range.

Motivation for the above considerations

The above results have been presented on purpose to later compare and validate the model. They should give an insight of the expected results. Experimental data from the VUB will also be used for the model calibration.

3.5.2 Model description

The main metric used to characterize the recuperator performances is the effectiveness. The later can be measured experimentally. Through the intermediate of the NTU value, that can be evaluated thanks to its relationship with the effectiveness, the global UA value of the recuperator is obtained. However, attention should be paid to the fact that Eq. (3.28) holds for a counter-flow heat exchanger while the T100 recuperator is of mixed cross- and counter-flow type. Nevertheless, this method is a quick access to a rough estimate of the global UA value of the recuperator. Looking closer to the heat transfer development around the matrix, a relationship between the local convective and conductive heat transfer coefficients and this global UA value can be established. From the heat transfer model presented in Fig. 3.8, the global UA value can be written as

$$\frac{1}{UA} = \frac{1}{h_h A} + \frac{t_w}{k_w A} + \frac{1}{h_c A} \, , \tag{3.30}$$

where h and k are the convective and conductive heat transfer coefficients respectively. Assuming the conductive term of Eq. (3.30) to be negligible and taking the convective coefficients to be equal to each other (i.e. $h_h = h_c = h$), the global UA value becomes

$$\frac{1}{UA} \simeq \frac{1}{h_h A} + \frac{1}{h_c A} \simeq \frac{2}{hA} \, , \tag{3.31}$$

with h the global convective coefficient. For $k_w = 16 W/mK$ (thermal conductivity of stainless steel [88]), $t_w = 0.15 mm$ (plates thickness [36]) and $h_c = h_h = 100 W/m^2K$ (typical upper coefficient for forced convection in air [88]), the first assumption holds (3 magnitude orders of difference between the conductive and convective terms). The second assumption (i.e. $h_h = h_c$) is due to a lack of information about the flow development on both sides. However, the hot fluid (i.e. exhaust gas) and cold fluid flow rates (i.e. compressed air) are very similar. Since h is a function of the flow velocity [88], the assumption $h_h = h_c$ can be justified.

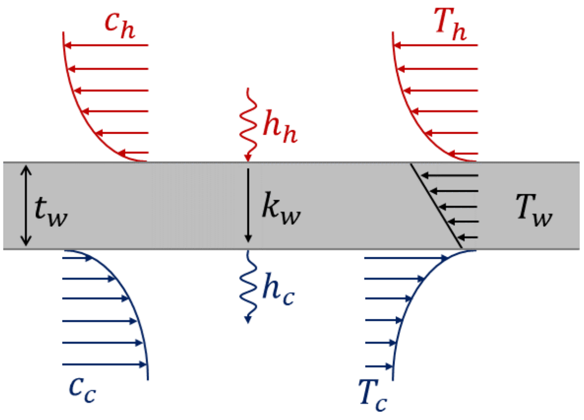

Figure 3.8: Representation of the heat transfer development around a recuperator steel plate.

These assumptions yield the hot and cold sides convective heat transfer coefficients as

$$h_h A = h_c A \simeq 2UA \, , \tag{3.32}$$

for any given UA value.

As stated earlier in this Section, the recuperator model must integrate the thermal capacitance phenomenon. This can be achieved through the application of the energy conservation to the entire recuperator matrix. Figure 3.9 represents the control volume to which the energy conservation should be applied. London [85, 86] proposed a list of idealization to simplify the problem. Among them, the mass flow rates $\dot{m}_h$ and $\dot{m}_c$ are assumed to be constant (i.e. faster response to flow change than to fluid temperature). The overall system is also supposed to be adiabatic (i.e. perfect insulation of the casing) and no internal heat generation exists (e.g. from chemical reaction). The heat flow through the wall is assumed to be normal to the fluid flows only (validated assumption [31]).

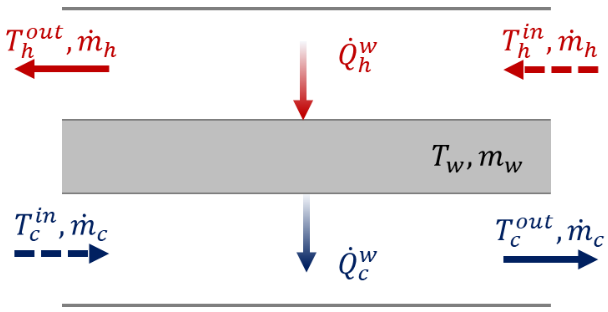

Figure 3.9: Application of the energy conservation on a lumped volume representing the recuperator.

From this set of simplifications, the lumped volume approach and the energy conservation can be used to compute the evolution the wall (i.e. matrix) temperature for a given set of inlet boundary conditions (represented in Fig. 3.9).

This simplified model, although correct from an energy point view (i.e. respect of energy conservation), is not physically consistent. Figure 3.10 illustrates the limitation involved when using only one temperature T_w for the recuperator matrix. By neglecting the 1D temperature distribution inside the matrix, the inlet and outlet temperatures at the boundaries are not coherent with the wall temperature. The above model can be easily extended in order to account for the 1D effects (i.e. variation of matrix temperature with heat transfer area). A side by side adjunction of the lumped volumes represented in Fig. 3.9 allows to model the evolution of T_w with the heat transfer area (A). The newly formed model is represented in Fig. 3.11. It now consists in a global lumped volume discretized into N virtual *cells*, each of them representing a discrete element of the recuperator alongside the heat transfer area.

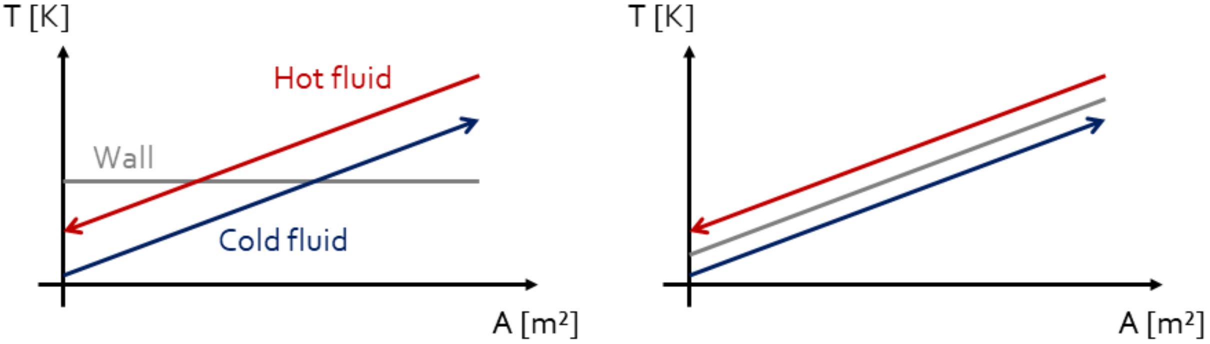

Figure 3.10: Temperature profiles in a counter-flow heat exchanger: cold fluid (blue), matrix (gray) and hot fluid (red). *Left*: unrealistic case with only one cell. *Right*: correct profiles.

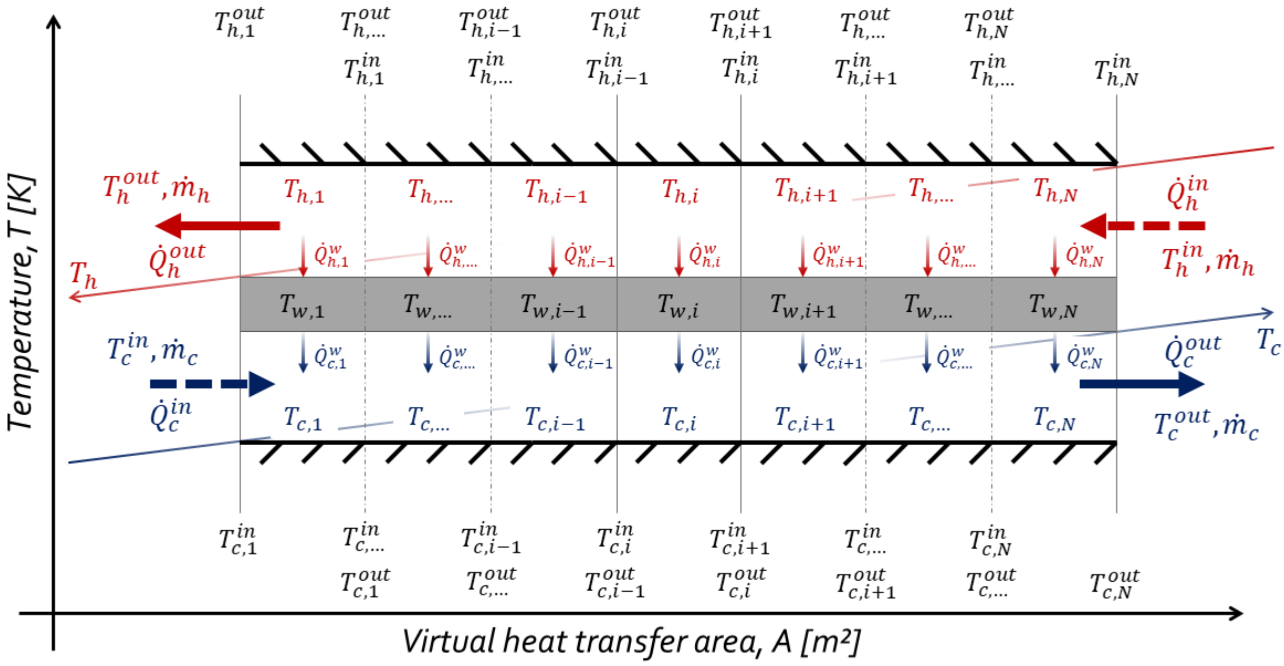

Figure 3.11: Modelling paradigm of the recuperator.

The global model can now be formulated mathematically. At any time t, in the hot side h, the difference between the input ($\dot{Q}_{h,i}^{in}$) ant output ($\dot{Q}_{h,i}^{out}$) heat flows carried into and out of each cell via the stream medium (not represented on Fig. 3.11 for the clarity) is equal to the heat flow ($\dot{Q}^{w}_{h,i}$) going into the matrix. This is written as

$$\dot{Q}^{in}_{h,i} - \dot{Q}^{out}_{h,i} = \dot{Q}^{w}_{h,i} \tag{3.33}$$

The meaning of this statement is that each cell in the hot gas side cannot play the role of an energy accumulator. In other words, the calculation of the gas cells is quasi-steady state. This is based on the assumption that the gas retention time is rather short compared to temperature change rates of the thermal masses [5]. This is true for an infinite number of cells, and should also be a reasonable assumption for a less thin discretization. The question of the number of cells will be further discussed later in this Section. When developing Eq. (3.33) into

$$\dot{m}_h c_{p,h}(T^{in}_{h,i})\Big(T^{in}_{h,i} - T^{out}_{h,i}\Big) = h_{h,i}A_i\Big(T^{av}_{h,i} - T_{w,i}\Big) = h_{h,i}A_i\left(\frac{T^{in}_{h,i} + T^{out}_{h,i}}{2} - T_{w,i}\right), \tag{3.34}$$

$$T^{out}_{h,i} = \frac{(\dot{m}_h c_{p,h}(T^{in}_{h,i}) - \frac{1}{2}h_{h,i}A_i)T^{in}_{h,i} + h_{h,i}A_iT_{w,i}}{\dot{m}_h c_{p,h}(T^{in}_{h,i}) + \frac{1}{2}h_{h,i}A_i}, \tag{3.35}$$

one obtains the outlet temperature of the hot fluid in each cell. In Eq. (3.34) and (3.35), the local UA value of each cell is $h_{h,i}A_i = \frac{h_h A}{N}$.

With the same reasoning, the cold fluid outlet temperature is obtained as

$$\dot{Q}^{out}_{c,i} - \dot{Q}^{in}_{c,i} = \dot{Q}^{w}_{c,i}, \tag{3.36}$$

$$\dot{m}_c c_{p,c}(T^{in}_{c,i})\Big(T^{out}_{c,i} - T^{in}_{c,i}\Big) = h_{c,i}A_i\Big(T_{w,i} - T^{av}_{c,i}\Big) = h_{c,i}A_i\left(T_{w,i} - \frac{T^{in}_{c,i} + T^{out}_{c,i}}{2}\right), \tag{3.37}$$

$$T^{out}_{c,i} = \frac{(\dot{m}_c c_{p,c}(T^{in}_{c,i}) - \frac{1}{2}h_{c,i}A_i)T^{in}_{c,i} + h_{c,i}A_iT_{w,i}}{\dot{m}_c c_{p,c}(T^{in}_{c,i}) + \frac{1}{2}h_{c,i}A_i} \tag{3.38}$$

For any set of recuperator inlet boundary conditions and with the above derived model for the hot and cold sides cells outlet temperatures, the energy balance can be written as

$$m_{w,i}c_w\frac{dT_{w,i}}{dt} = \dot{Q}^{w}_{h,i} - \dot{Q}^{w}_{c,i} \tag{3.39}$$

$$= \dot{m}_h(h(p^{in}_{h,N}, T^{in}_{h,i}) - h(p^{in}_{h,N}, T^{out}_{h,i})) - \dot{m}_c(h(p^{in}_{c,1}T^{out}_{c,i}) - h(p^{in}_{c,1}, T^{in}_{c,i})), \tag{3.40}$$

for each discrete matrix element. In this equation, the mass of each cell is equal to the global matrix mass divided by the number of cells ($m_{w,i} = \frac{m_w}{N}$). Here h for stands for the specific enthalpy and c_w represents the matrix specific heat capacity.

This dynamic model will be calibrated in Section 5.1.4 with the aim of giving it a dynamics fitting experimental observations (fine tuning of m_w) and the desired effectiveness (fine tuning of UA). The number of differential equations it consists in is equal to the number of cells that are utilized. A trade-off between the model accuracy and computational complexity must therefore to be established.

Pressure losses model

The magnitude of the pressure losses of any viscous fluid and over any duct is physically connected to flow velocity. The Darcy-Weibach correlation, deriving from fluid mechanics, can accurately model regular losses (i.e. losses due to the fluid viscosity). As the fluid inside the recuperator is subject to changes in flow direction, singular losses (e.g. losses due to recirculation zones) should also be modelled. Both regular and singular losses can be represented with an improved version of the Darcy-Weibach correlation, expressed as

$$\Delta p = \left(c_f \frac{L}{D_h} + \xi \right) \frac{\rho c^2}{2} \ , \tag{3.41}$$

where c_f is the friction coefficient, L the duct equivalent length, D_h the duct hydraulic diameter, ξ the coefficient for singular losses, ρ the fluid density and c the flow velocity. Although Eq. (3.41) provides an accurate and physical model of the pressure losses, the limited knowledge of the recuperator geometry and of flow development inside it makes it challenging to apply the improved Darcy-Weibach correlation in this case. Consequently, a simpler model must be utilized. The pressure losses in each side of the recuperator can be quantified with

$$\Delta p = (1 - \sigma_{rec}) p_{in} \ , \tag{3.42}$$

where σ_{rec} is a virtual pressure losses coefficient. From the knowledge gained with the physical nature of the pressure losses, expressed with Eq. (3.41), and with the results presented in Fig. 3.7b, a correlation between σ_{rec} and the squared of the mass flow rate can be established,

$$\sigma_{rec} = f(\dot{m}^2) \ , \tag{3.43}$$

as suggested by [6]. This will be further discussed during the model calibration in Section 5.1.4.

Black-box representation and final considerations

The recuperator black-box model and its input and output variables are represented in Fig. 3.12. As a final remark for the recuperator model, given its volume, the absence of a mass accumulator (i.e. plenum similar to that of the combustion chamber) could raise interrogations. In fact, the reason for which the mass flow rates are considered as time independent and that no accumulation is taken into account is due to the limited knowledge that we have of the aerodynamics inside the recuperator. The application of a plenum would require the knowledge of the inlet and outlet mass flow rates while only the inlet boundary conditions are available in this model. Although some authors [5] mention the use of plena at the recuperator inlet and outlet sections in their model, few explain which approach was chosen to obtain the outlet flow rates. If need arises for the modelling of mass accumulation inside the recuperator, the computation of the outlet mass flow rates should be of prior interest.

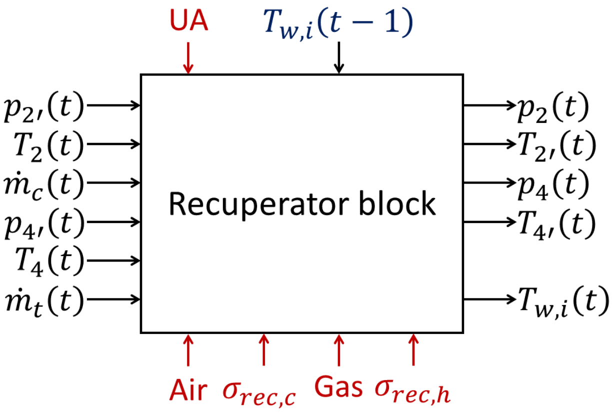

Figure 3.12: Recuperator block input and output variables.

3.5.3 Determination of the number of cells

In this Section, the number of cells that will be used in the recuperator model is determined. The trade-off to be investigated lays between the model accuracy and its computational complexity. The dynamic behavior of the component is also verified to ensure that the model outputs physically consistent results during transients.

A rough calibration aiming at reproducing transients in the T100 was performed. It will not be presented here since it was only made on purpose to validate the number of cells. The boundary inlet conditions that were applied to the model are represented on Fig. 3.13.

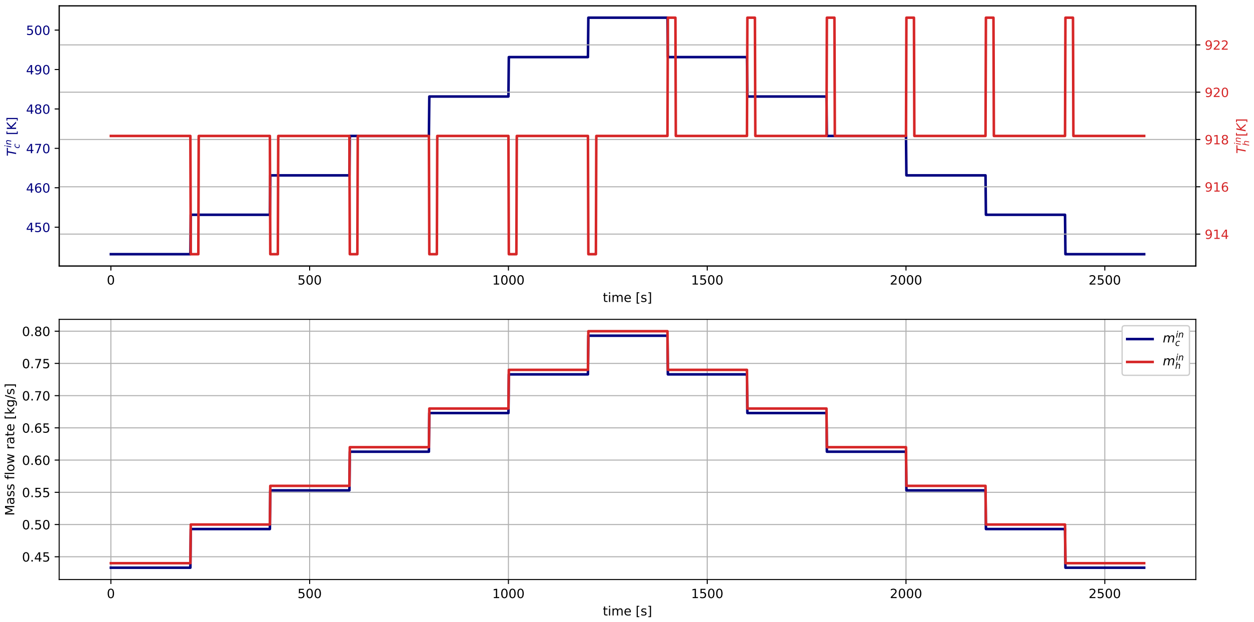

Figure 3.13: Inlet boundary conditions (temperatures and flow rates) for the cold side (blue) and hot side (red) applied to the recuperator model for the validation of the number of cells.

The response of the temperature at the cold leg outlet (T_c^{out}) is depicted in Fig. 3.14 for a number of cells $N = 100$. The obtained response profile is perfectly consistent with the experimental results presented by [28]. However, a fine tuning of the matrix mass will be made in Section 5.1 in order to obtain the correct time constant for the response and to limit the under- and over-shoots. The current result for T_c^{out} will be taken as a reference for the comparison of the temperature responses obtained with a reduced number of cells. The arbitrary choice of $N = 100$ is inspired from [89] who developed a similar discretized model for an evaporator.

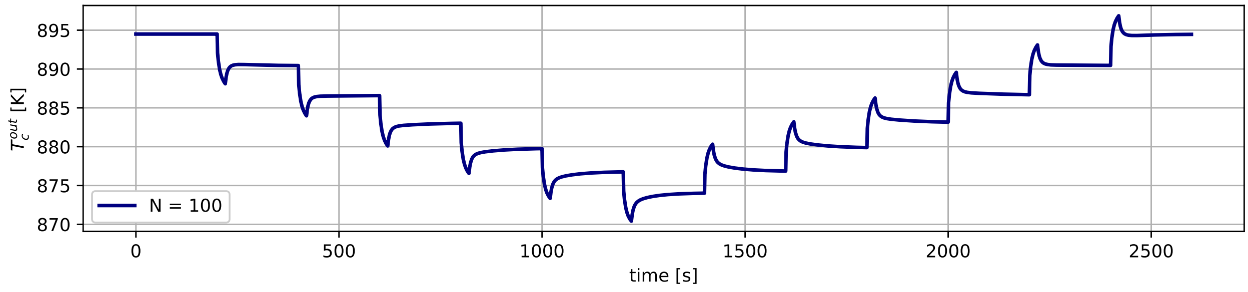

Figure 3.14: Recuperator cold side outlet temperature as resulting of the transient boundary conditions depicted in Fig. 3.13.

Table 3.1 gathers the errors obtained with different number of cells for T_c^{out} and for the effectiveness (ϵ). The latter are defined as

$$e_{T_c^{out}} = \frac{|T_c^{out}(N=i) - T_c^{out}(N=100)|}{T_c^{out}(N=100)} \qquad e_\epsilon = \frac{|\epsilon(N=i) - \epsilon(N=100)|}{\epsilon(N=100)} \tag{3.44}$$

The mean error can be interpreted as the steady state error. The maximum error illustrates the error during transients. The maximum to mean error ratio can be perceived as the error magnitude during transients with regard to the steady state error.

The number $N = 5$ is a clear corner stone above which the mean errors, maximum errors and maximum to mean error ratios drop. For $N = 10$, the improvement in accuracy (max. error

	Errors during transient compared to the case $N = 100$					
	Error on T_c^{out} [%]			Error on ϵ [%]		
N	Mean	Max.	Max./Mean	Mean	Max.	Max./Mean
2	$5.679e-2$	$7.049e-1$	12.41	$1.202e-1$	$1.432e-0$	11.92
3	$2.075e-2$	$2.640e-1$	12.72	$4.387e-2$	$5.241e-1$	11.95
5	$5.867e-3$	$1.423e-2$	2.426	$1.241e-2$	$2.922e-2$	2.354
10	$1.389e-3$	$3.213e-3$	2.314	$2.937e-3$	$6.729e-3$	2.291

Table 3.1: Validation of the number of cells based on the error of the response to the transient described in Fig. 3.13 evaluated w.r.t. the case with $N = 100$.

reduced by a factor 10 compared to $N = 5$) does not justify the increased complexity (system of 10 differential equations to be solved). The significant gain in precision when increasing N from 3 to 5 (mean error for T_c^{out} reduced by a factor 10) undoubtedly supports the addition of 2 equations compared to the case $N = 3$. Nevertheless, in order to limit the model complexity, it is here decided to bound the number of cells to $N = 3$. This decision is motivated by the relatively low mean errors obtained with that model configuration (less than 0.05%). If needs be to increase the recuperator accuracy during transients, the model can be easily refined by using 5 cells instead of 3.

Quoilin et *al.* [89], in their similar model for an evaporator, used $N = 10$. This trade-off was deriving from steady state analyses of the heat flow through the matrix only. Henke et *al.* [5] also used a similar model but integrated longitudinal conduction in the recuperator matrix, the latter being responsible of the effectiveness degradation at part load [31]. However, they did not communicate on the selected number of cells. Kim et *al.* [24] developed a dynamic model for the Capstone $C30$ and they discretized the recuperator as-well, but with a slightly different cells arrangement. They also performed a sensitivity analysis of the steady-sate error on the heat flow with regard to the number of cells. The relative error was exponentially decreasing with the number of cells. The computed errors were $e_{N=2} = 2.791e-2\%$, $e_{N=3} = 1.331e-2\%$, $e_{N=5} = 4.749e-3\%$ and $e_{N=10} = 1.018e-3\%$. The latter are very close to mean errors on T_c^{out} reported in Table 3.1. Kim et *al.* [24] also used $N = 10$ in their model. However, these values must be interpreted with precaution since different error definitions are used.

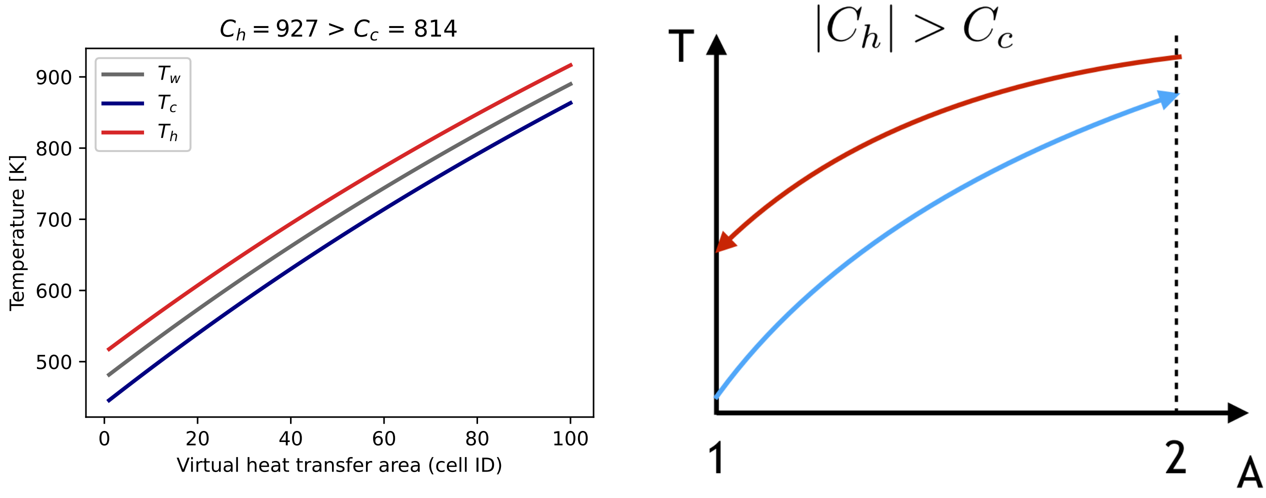

(a) Obtained temperature profile

(b) Theoretical temperature profile [88]

Figure 3.15: Comparison of obtained and expected temperature profiles in the recuperator. The obtained profiles have a the expected curvature direction.

The goal of the discretization into cells being to account for the 1D phenomenon (i.e. variation of matrix temperature alongside heat transfer area), the temperature profiles inside the recuperator should be analysed. Figure 3.15a depicts the obtained profiles while Fig. 3.15b represents the theoretical expectation for a counter-flow heat exchanger with dominating hot heat capacity rate (e.g. a recuperator) [88]. The obtained profiles match the curvature expectations and the temperature differences at the inlet and outlet sections also have the correct relative magnitudes (i.e. larger difference at the cold leg inlet than at the outlet).

3.6 Shaft block

The shaft does not directly contribute to the thermodynamic cycle. However, it constitutes the core element of the mGT by transferring the power produced by the turbine to the compressor and to the generator. Its high rotational speed confers him the role of an important energy accumulator inside the system. However, its relatively low moment of inertia (I), compared to heavy duty gas turbines, limits the amount of energy stored into it. This low moment of inertia also makes the rotational speed of mGTs much more sensitive to disturbances. It is therefore important to construct an accurate model for the shaft dynamics.

The shaft black-box model and its input and output variables are represented in Fig. 3.16. Note that, in this figure, N represents the rotational speed expressed in $[rpm]$.

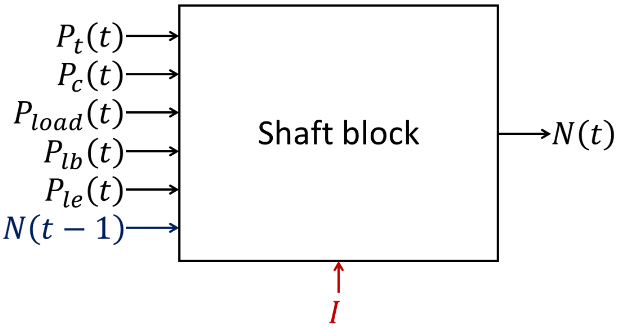

Figure 3.16: Shaft block input and output variables.

Governing equations

A shaft dynamic behavior is governed by the difference between the input power (P_{in}) and the load applied to it (P_{out}). The conservation of rotating energy is therefore formulated mathematically as

$$\frac{d\omega}{dt} = \frac{P_{in} - P_{out}}{I\omega} , \tag{3.45}$$

where ω is the shaft angular velocity. In the case of a mGT, P_{in} corresponds to the power generated by the turbine (P_t). P_{out} can be split into two categories: (1) the useful power and (2) the mechanical power losses. The useful power accounts for the power required to drive the compressor (P_c) and the mechanical power absorbed by the generator (P_{gen}). The power losses represent all the friction losses the shaft assembly is subject to. The latter are mainly the bearing losses and some eventual air friction losses. Since it is difficult to identify them separately, they are both regrouped under the bearing losses (P_{lb}).

Modelling approaches

There are different modelling approaches for the conversion from mechanical energy to the final electricity generated my the mGT, depending on the way the machine is operated. The first one is represented in Fig. 3.17.

With this approach, P_{gen} is split into the electrical energy generated by the mGT (P_{elec}) and the energy lost inside the generator and power electronics, as well as the energy consumed by the mGT auxiliaries (i.e. fuel compressor, ventilation air fan, oil pump, buffer air pump, cooling water pump of the generator and in a minor way, the control system). These energies are modelled as a whole with the electrical losses (P_{le}). In this case, the load power (P_{load}) is computed by the control system (see Section 3.7) such that P_{elec} matches the demanded power (P_{dem}).

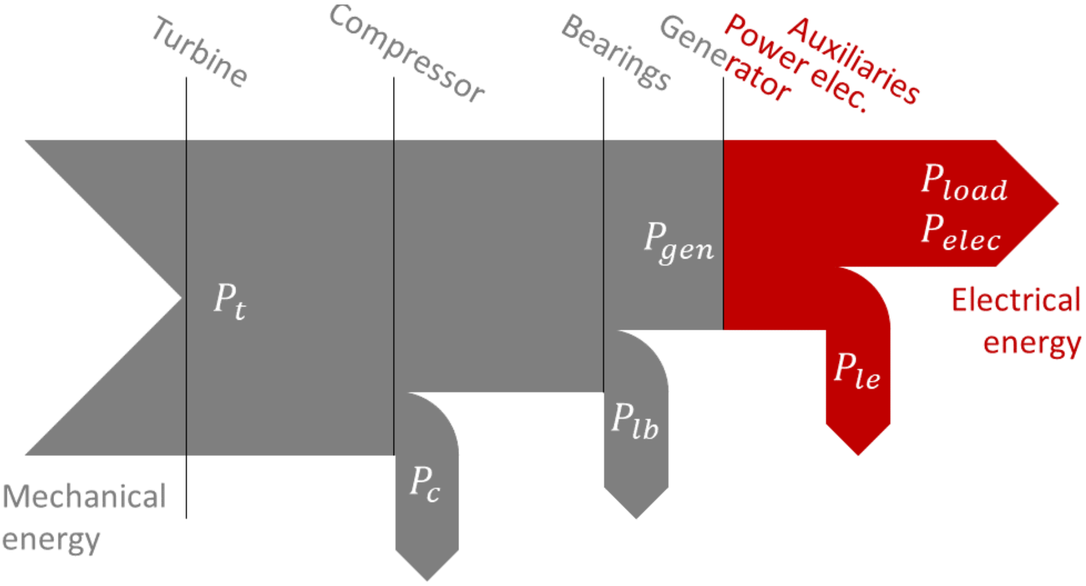

Figure 3.17: Model for power balance on the shaft: first approach.

The second approach is depicted in Fig. 3.18. With the latter, P_{load} is computed by the controller such that the power coming out of the power electronic converter matches P_{dem}. In this case, P_{elec} is equal to P_{dem} subtracted by the auxiliaries consumption (P_{aux}).

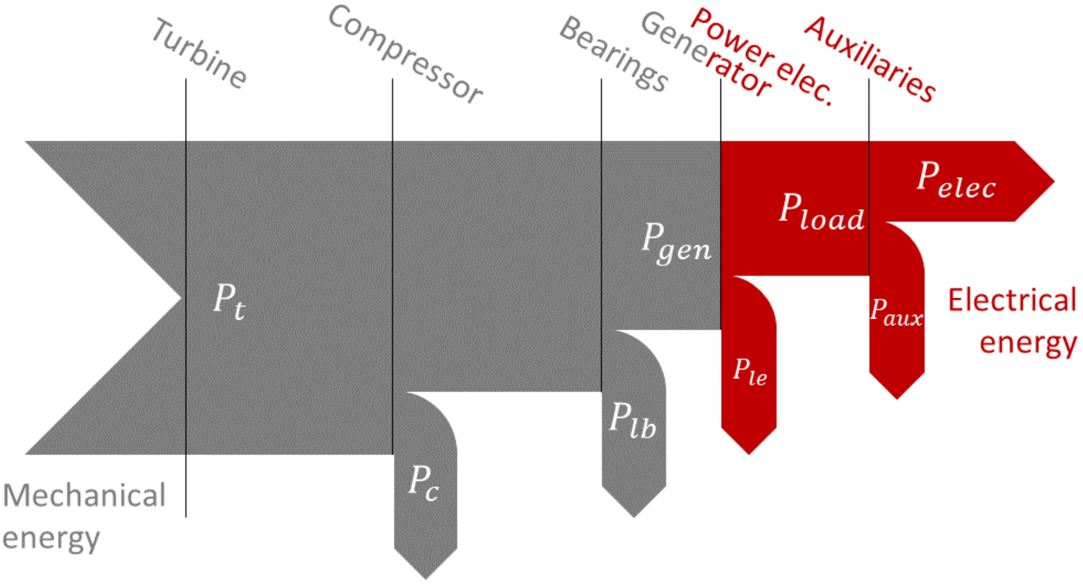

Figure 3.18: Model for power balance on the shaft: second approach

Final model formulation

Based on the above considerations, the global energy balance introduced by Eq. (3.45) can be rewritten as

$$\frac{d\omega}{dt} = \frac{P_t - P_c - P_{load} - P_{lb} - P_{le}}{I\omega} \tag{3.46}$$

where, with the first approach, P_{le} accounts for the auxiliaries consumption while it does not with the second. The dissociation between the two approaches was introduced because, depending on the mGT system, the P_{elec} is evaluated differently. Correlations for P_{lb}, P_{le} and P_{aux} will be proposed in Section 5.1.6, based upon models published in the literature and experimental data. There, the value of I will also be discussed.

3.7 Controller block

In order to perform global transient analyses with the developed model, a controller must be implemented. Indeed, the regulation of the generated power and amount of injected fuel (i.e. input variables $u(t)$ introduced in Section 3.1) is required to ensure the system stability while satisfying the demanded power requirements in any set of atmospheric conditions (i.e. disturbance variables $d(t)$ introduced in Section 3.1).

Heavy duty gas turbines are traditionally operated at constant speed and constant TOT for any load requirement [48, 90]. The speed and TOT are maintained constant by adjusting the fuel flow rate and by varying the inlet guide vanes (IGV) angle. Micro gas turbines, instead, are variable speed controlled [21, 46]. To any power demand corresponds a predefined reference speed. The fuel injection rate is regulated to maintain the TOT constant.

Hubin [91] received the control scheme of T100 from the manufacturer [28]. The controller he implemented in the `Simulink` environment was later reused and partially retuned by Govaerts in his `Simulink` model [28]. The system showed a stable behavior and a very good agreement with experimental results during transients. The model also integrated the sensors and actuators inertia. Other authors used the same control logic but with their own control schemes [5, 11]. Within this Thesis, it has been decided to reuse the scheme received by Hubin [91] because of the excellent results it provided. Therefore, the main goal of this work was the successfully implement the T100 controller inside the `Python` model.

The detailed information about the control system must be kept confidential. Consequently, this Thesis only provides the general build-up of the controller (detailed schemes hidden behind the PID blocks). The T100 controller consists into two major systems, described below.

3.7.1 Power control

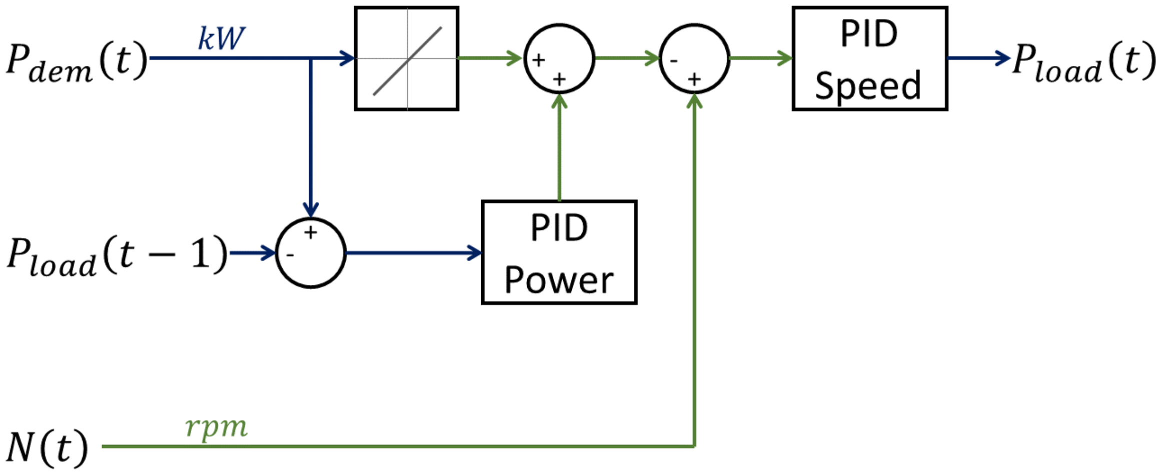

Figure 3.19: Scheme of the power control system: (1) calculation of the corrected reference speed, (2) regulation based on the error on speed.

This control loop aims at regulating the mGT speed through a control of the load (P_{load}) applied by the generator to the shaft. This load corresponds to the electrical power that is produced by the mGT.

First, a look-up table links the demanded power (P_{dem}) to a predefined reference speed. Afterwards, this reference speed is corrected with a PID regulation of the fault signal between P_{dem} and P_{load}. Finally, the error between the corrected reference speed and the actual shaft speed is sent to another PID controller that outputs an updated P_{load}. The power control scheme is represented in Fig. 3.19.

3.7.2 Fuel control

This control system regulates the amount of fuel that is injected inside the combustion chamber. It is subdivided into three different loops. The injected fuel rate corresponds to the least among the three different computed values.

- **Acceleration loop**: used during the start-up phase to limit the acceleration of the shaft.
- **Speed loop**: used to ensure that the machine is not over-speeding.
- **Temperature loop**: used to maintain TOT constant.

However, only the TOT control is implemented in this work, because the two other loops schemes were not available. According to [28], the TOT loop is used most of the time in normal conditions.

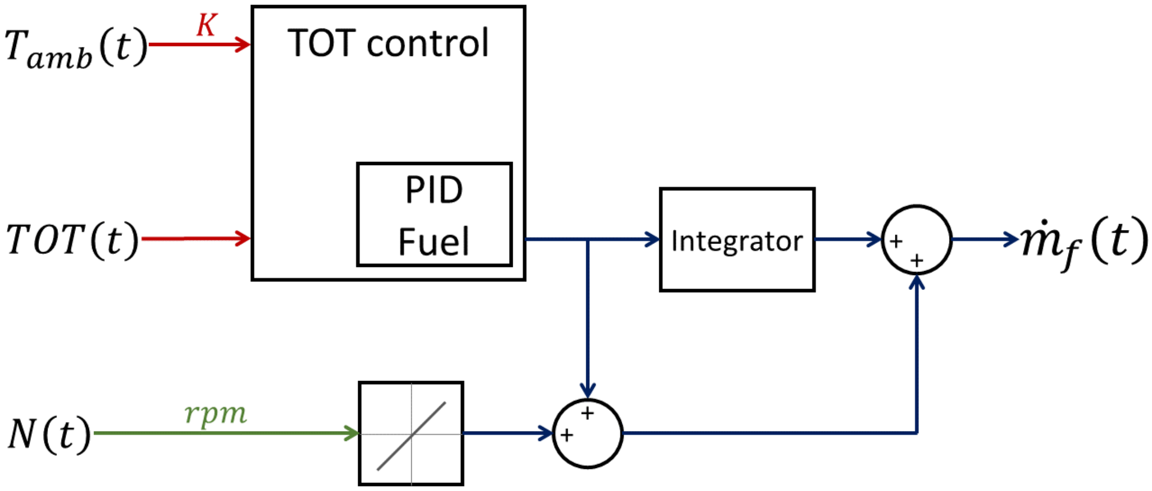

Figure 3.20: Scheme of the fuel control system: (1) TOT error signal, (2) reference fuel for current speed.

At first, a compensation fuel requirement is evaluated based on the ambient temperature (T_{amb}) and the TOT. A reference value is attributed to TOT depending on T_{amb} (e.g. 645^oC at 15^oC). This reference value is selected to maximise the mGT efficiency (i.e. maximization of temperature maximizes the Carnot efficiency) while respecting the constraint on the maximum recuperator hot leg inlet temperature. With reduced ambient temperatures, the compression is achieved more efficiently and less power is consequently required to drive the compressor. Therefore, the TIT, and thus also the TOT, must be limited to reduce the power generated by the turbine.

In a second time, a predefined reference fuel requirement is attributed based on the shaft speed via a look-up table. The TOT compensation fuel is then added to this reference fuel requirement. This newly defined corrected fuel requirement is finally summed with the integral of the *TOT* compensation fuel.

The fuel control scheme is represented in Fig. 3.20. In this work, as mentioned in Section 3.3, the compressor used to increase the natural gas pressure is not modelled. It is therefore assumed that the input natural gas naturally matches the fuel system requirements prescribed by Turbec (i.e. $6.0 bar$ [27]).

3.8 Global mGT dynamic model

3.8.1 Graphical representation

Thanks to the black-box illustrations introduced for each component at the end of the previous Sections, the global mGT model can be represented with the block diagram depicted in Fig. 3.21. A larger version of it is available in Appendix D.

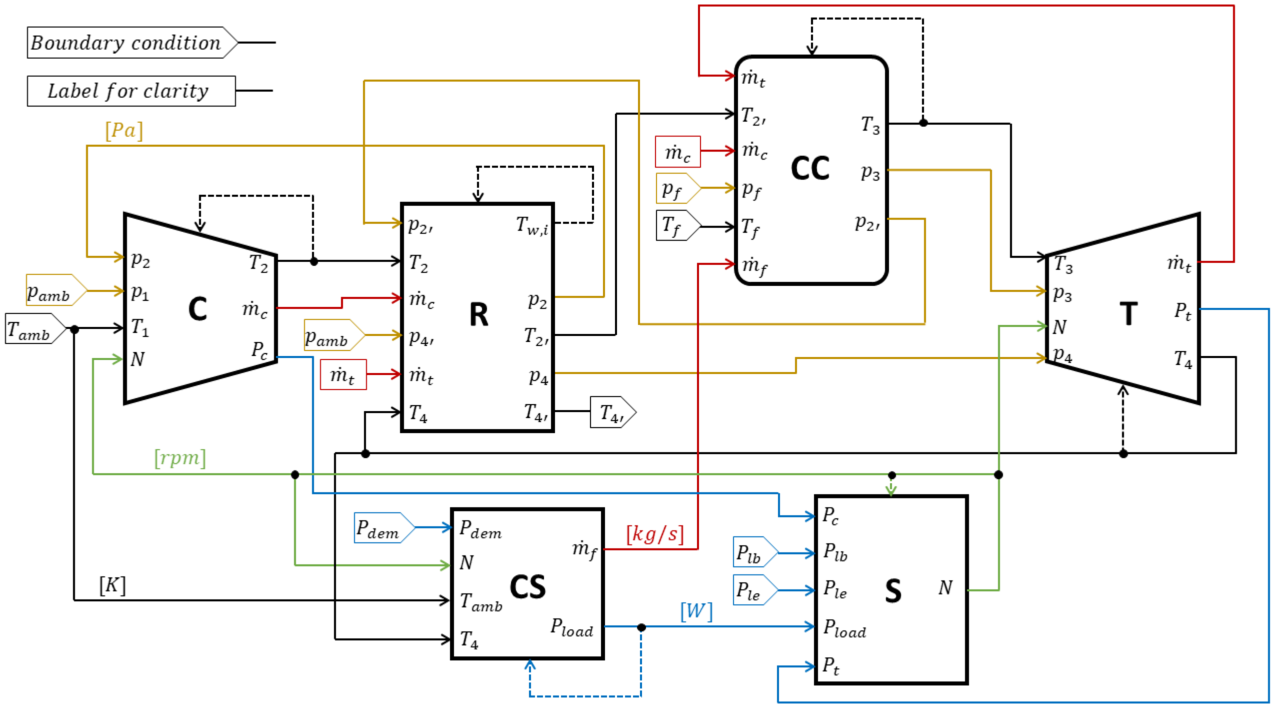

Figure 3.21: Block diagram representation of the global mGT model. Pressure streams in *gold*, temperature streams in *black*, mass flow streams in *red*, power streams in *blue* and shaft speed streams in *green*. The dashed lines represent the feedback loops. A larger version is available in Appendix D.

3.8.2 Mathematical formulation

The non linear system of equations describing the temporal evolution $\dot{x}(t)$ of the state variables, for a given set of initial values $x(t)$, disturbance $d(t)$ and control $u(t)$ variables, is reported below.

Let us emphasize that only one of the three equations utilized for the recuperator (i.e. $T_{w,i}$) is reported, because of their similarity (i.e. $i \in [1, 2, 3]$ and $N = 3$). The global dynamic model is therefore limited to a set of nine differential algebraic equations (DAE).

$$
\begin{aligned}
\frac{dT_2}{dt} &= \frac{1}{m_{cas,comp.}c_{casing}}(\dot{m}_c(h(p_2, T_{air,comp.}) - h(p_2, T_2))) \\
\frac{dT_3}{dt} &= \frac{1}{m_{cas,comb.}c_{casing}}(\dot{m}_t(h(p_3, T_{gas}) - h(p_3, T_3))) \\
\frac{d\rho_3}{dt} &= \frac{1}{V_{comb}}(\dot{m}_c + \dot{m}_f - \dot{m}_t) \\
\frac{du_3}{dt} &= \frac{1}{\rho_3 V_{comb}}(\dot{m}_c h_{2'} + \dot{m}_f(h_f + \eta_{comb.}LHV) - \dot{m}_t h_3 - u_3(\dot{m}_c + \dot{m}_f - \dot{m}_t)) \\
\frac{dT_4}{dt} &= \frac{1}{m_{cas,turb}c_{casing}}(\dot{m}_t(h(p_4, T_{gas,turb.}) - h(p_4, T_4))) \\
\frac{d\omega}{dt} &= \frac{1}{I\omega}(P_t - P_c - P_{load} - P_{lb} - P_{le}) \\
\frac{dT_{w,i}}{dt} &= \frac{1}{m_{w,i}c_w}(\dot{m}_h(h(p^{in}_{h,N}, T^{in}_{h,i}) - h(p^{in}_{h,N}, T^{out}_{h,i})) - \dot{m}_c(h(p^{in}_{c,1}T^{out}_{c,i}) - h(p^{in}_{c,1}, T^{in}_{c,i})))
\end{aligned}
$$

CHAPTER 4
NUMERICAL MODEL

This short Chapter introduces the general organization of the numerical tool. It aims at briefly describing the simulation environment layout that has been constructed for this work, as well as how the sequential solution for the system of differential equations proceeds. Some of the improvements this simulation tool could be subjected to, are also addressed.

4.1 Numerical framework

The numerical framework, constructed in `Python 3`, is illustrated in Fig. 4.1. It is organized into different modules, each of them being dedicated to a specific task. The `Thermo` *`module`* contains all the functions required for the evaluation of thermodynamics and chemical quantities (e.g. specific heat capacities, molar masses, ...). As stated earlier, the reference tables are issued from `thermo 0.2.6` [77] (gas constants and molar masses) and from `CoolProp` [78] (all the other quantities). The `Combustion` *`module`* provides the functions utilized for the computation of the mixtures composition and of the mixtures oxidation process. The `Maps` *`module`* integrates all the functions required for the numerical formulation of the compressor and turbine performance

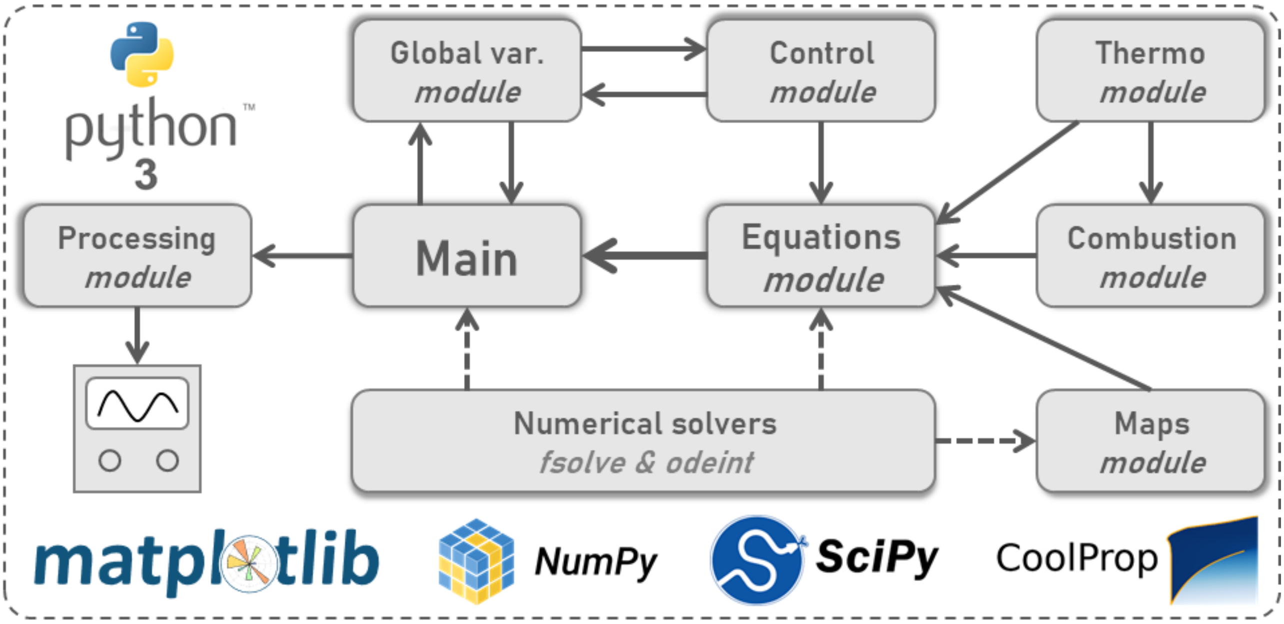

Figure 4.1: Simulation environment of the numerical tool.

maps. It also contains the functions requested for the processing of the results on these maps. The `Global var.` *`module`* is used to store the global variables that have to be accessible by the `Control` *`module`*, independently of the code execution (i.e. during the integration process). The `Equations` *`module`* contains all the equations introduced in Chapter 3, under the form of `Python` functions. There, the global system of differential equations presented in Section 3.8 is assembled. The sequential solving procedure takes place in the `Main` class, to which, for each time step, the `Equations` *`module`* provides the vector of derivatives of the state variables. The `Processing` *`module`* is utilized for the management of the simulation results and for the graphical illustrations.

4.2 Sequential solving procedure

The sequential solving procedure, resulting from the interaction between the `Main` class and the `Equations` *`module`*, is explained on the flow chart in Fig. 4.2. At first, steady state initial values are computed for the state variables for a given set of initial conditions.

It should be emphasized that the selection of guess values needed for computation of the initial state variables is of major importance. Indeed, the stiffness of the global system of equations (i.e. mainly induced by the required match between the compressor and turbine flow rates) seriously complicates its resolution. Thus, as soon as the global mGT model is calibrated, efforts must be made to manually find the proper set of steady state variables in the different off-design conditions. Therefore, as soon as the steady state points are computed for different loads, they should be stored for future initializations of the solving procedure.

Once the state variables are initialized, the sequential procedure is launched. It can be observed in Fig. 4.2 that the combustion is computed iteratively. The evaluation of p_3 and T_{gas} indeed requires the evaluation of the flue gas heat capacity, itself function of the flue gas composition. But this composition is a function of the air flow rate ($\dot{m}_c$), itself function of p_3, so an iterative process is required. The number of necessary iterations is typically around 5.

At the end of the sequential procedure, the derivatives of the state variables are evaluated by the mean of the conservation equations. The numerical solver (*odeint*) then integrates the system to the next time step. In this work, the numerical scheme utilized in *odeint* is the *Adams/BDF* method, and is issued from the *LSODA* routine from the `FORTRAN77` library *ODEPACK*. Its main strength is to switch automatically between non-stiff (*Adams* method) and stiff (*backward differentiation formula*, *BDF* method) solvers, depending on the problem behavior.

4.3 Performances and discussions

The selection of the time step (Δt) is based on the statement that it has to be smaller than the smallest characteristic time (τ_{min}) of the phenomena inside the system, in order to ensure the numerical stability of the solvers. This numerical requirement typically applies to explicit solvers [40]. Although the present problem is implicit and *odeint* solvers utilize *multi-step methods*, this statement sufficiency remains preserved to ensure the numerical convergence.

Camporeale et *al.* [40] utilized explicit solvers and selected $\Delta t = 1ms$ for a $60MW$ gas turbine. Henke et *al.* [5] emphasized that the limiting factor for Δt was given by the dynamics involved with the mass conservation equations (i.e. related to the gas volumes). For a $100kW$ machine, they chose to use $\Delta t = 0.5ms$ in their in-house solver (i.e. explicit predictor corrector approach).

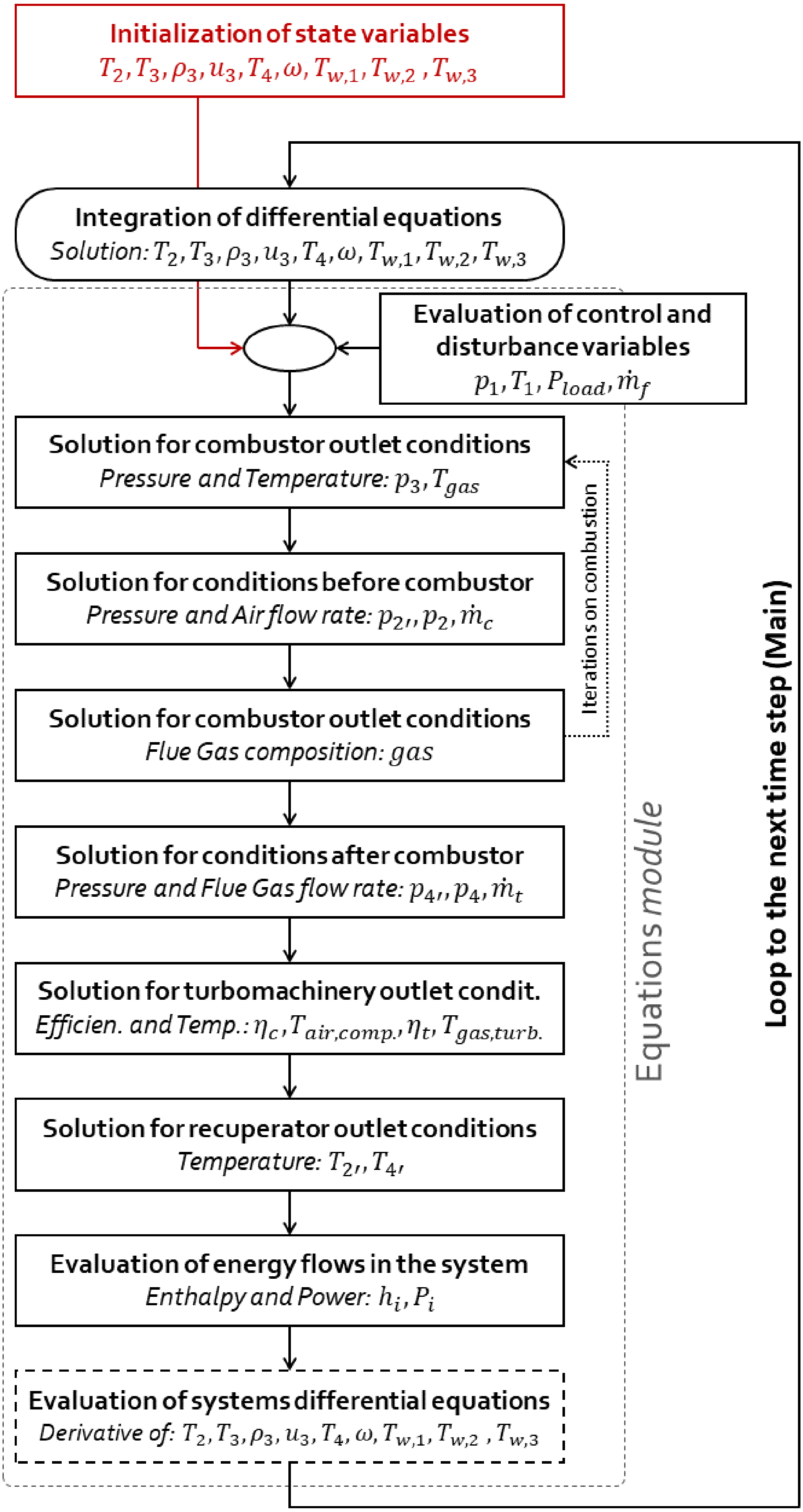

Figure 4.2: Sequential solving technique for the mGT model presented in Fig. 3.21.

As it will be justified in Section 5.1.3, the smallest gas volume utilized in this work is 5.542 liters. The associated time constant is $\tau = 5.542ms$, so Δt was initially set to $5ms$, to guarantee the numerical stability.

However, transient tests were performed with power steps limited to $\pm 20kW$ and revealed that $\Delta t = 100ms$ led to the exact same results as with $\Delta t = 5ms$. This can be explained by the relatively low disturbance and because the solvers utilize *multi-step methods*.

Therefore, since a greater Δt in the present implementation reduces the execution time, it is finally set to $\Delta t = 100ms$. Simulations were performed on a personal computer equipped with a 11th Gen Intel(R) Core(TM) i7-1165G7 @2.80GHz processor. The present model had a calculation to simulated time ratio of about 45 (15% of CPU utilization). Other time ratios obtained with different Δt are also reported in Fig. 4.3. However, it should be emphasized that, since *odeint* solvers utilize *multi-step methods*, the computation time is directly related to the magnitude of the events during the transient simulation. Therefore, Fig. 4.3. should only be interpreted as an illustration of the relationship between the time ratios and Δt (e.g. time ratios of about 20 were also obtained with other transients).

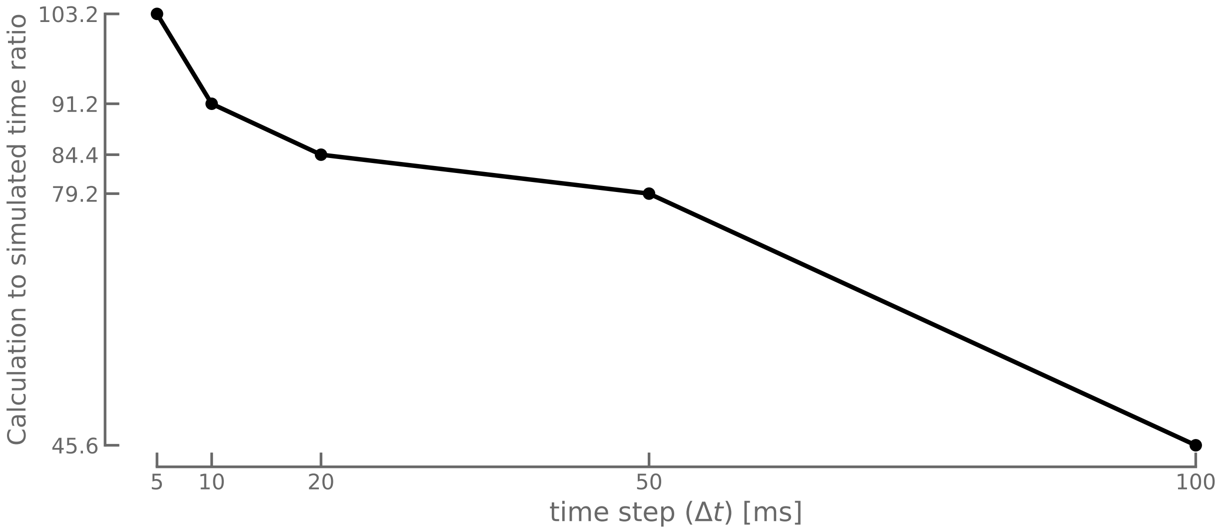

Figure 4.3: Numerical performances of the simulation tool: calculation to simulated time ratio.

These performances are extremely poor compared to other models (e.g. Henke et *al.* [5] obtained a ratio of 0.17 and Camporeale et *al.* obtained a ratio between 0.05 and 0.17) and prevent any real-time simulation (i.e. because time ratio superior to 1). They are attributed to (1) the resolution of the system to obtain p_3 and T_{gas} (see Eq. (3.16)), (2) to the iterative procedure on the combustion process (see Fig. 4.2) and (3) to the resolution of the ellipses for the computation of the compressor map (see Eqs. (2.8) & (2.9)).

Despite parallelization not being possible in this case, these performances could be improved by reducing the model complexity. Iterative procedures can be relaxed by utilizing the results from previous time steps as guess values. Also, previous time steps could be utilized to compute the average γ during the compression and expansion processes (see Eqs. (3.8) & (3.21)), consequently improving the model accuracy. Nevertheless, due to time limitation, such *memory blocks* have not been implemented in the model.

More information about the numerical model can be found in its documentation (not provided here, please contact this Thesis supervisor, Prof. Francesco Contino, to access it).

CHAPTER 5

CALIBRATION, SIMULATION RESULTS AND DISCUSSION

The goal of this Chapter is the validation of the numerical tool and the assessment of its performances. In Section 5.1, the physical model constructed in Chapter 3 is calibrated to represent the T100 part load and dynamic behavior. The steady state and dynamic results obtained with this calibrated model are then presented and compared with experimental data in Sections 5.2 and 5.3. The discussions made all along this Chapter are finally reported and summarized in Section 5.4, where the future development perspectives of this simulation tool for micro gas turbines are addressed. There, its current main assets are also highlighted.

5.1 Model calibration

This Section aims at performing the calibration of the model presented in Chapter 3, in order to fit the steady state and transient results obtained with the VUB T100 test rig. When the available experimental data are not sufficient, this calibration is made with additional results published in the literature.

This Section is summarized in Table 5.1, where the source for calibration data and future improvements are addressed. In Section 5.1.1, the VUB T100 test rig and the set of experimental data are briefly introduced. Then, each parameter of the mGT model is calibrated.

Component	**Parameter**	**Value**	**Source**	**Sec.**	**Improvements**
Compressor	Perform. map	n.a.	Manufact.	5.1.2	Part load performances
	Cas. heat cap.	$52.5kJ/K$	Expe.	5.1.2	Heat transfer model
Combustor	Efficiency	97%	Literature	5.1.3	Exp. validation
	Press. losses	5.5%	Literature	5.1.3	Exp. validation
	Cas. heat cap.	$0kJ/kg$	Literature	5.1.3	Fix instabilities
Recuperator	UA value	$\simeq 5.2kW/K$	Expe.	5.1.4	Diff. for each leg
	Mat. heat cap.	$92.5kJ/K$	Expe.	5.1.4	-
	Press. losses	5% & 2%	Literature	5.1.4	Exp. validation
Turbine	Cas. heat cap.	$61.1kJ/K$	Literature	5.1.5	Exp. validation
Shaft	Bear. losses	$\simeq 1.5kW$	Literature	5.1.6	Exp. validation
	Elec. losses	$\simeq 10kW$	Lit. Exp.	5.1.6	Exp. validation
	Inertia	$8.3e^{-3}kg \cdot m^2$	Literature	5.1.6	Identification technique
Controller	Settings	n.a.	Manufact.	5.1.7	Fix instabilities

Table 5.1: Summary of the calibration process.

5.1.1 Calibration data set

The VUB T100 test rig, which was first utilized for other research purposes, has been converted about ten years ago in a micro humid air turbine, based on a series 2 Turbec T100 mGT. Nevertheless, it can still be operated in a classical recuperated Brayton cycle configuration, despite slightly increased heat and pressure losses between the compressor outlet and recuperator inlet, due to new additional components.

The list of sensors utilized in pure mGT configuration and that are installed in the test rig are reported in Table 5.2. The detailed information about them was collected from [11].

Sensor	**Type**	**Location**	**Manufacturer**	**Accuracy**
T_1	-	Compressor inlet	-	$\pm 2^oC$
p_2	Differential sensor	Compressor outlet	*Yokogawa*	$\pm 150Pa$
T_2	Class-A Pt100	Compressor outlet	*Yokogawa*	$\pm 1\%$
$p_{2,bis}$	Differential sensor	Recup. cold leg inlet	*Yokogawa*	$\pm 150Pa$
$T_{2'}$	K-type class 1	Combustor air inlet	-	$\pm 0.4\%$
T_4	K-type class 1	Turbine outlet	-	$\pm 0.4\%$
$T_{4'}$	Class-A Pt100	Recup. hot leg outlet	*Yokogawa*	$\pm 0.55^oC$
N	Speed sensor	*Controller*	-	$\pm 0.1\%$
P_{load}	Power sensor	*Controller*	-	$\pm 1\%$
P_{dem}	-	*Controller*	-	-
P_{elec}	Power sensor	Grid connection	-	-
$\dot{m}_f$	Flow rate sensor	Combustor fuel inlet	-	$\pm 1\%$

Table 5.2: Detailed information about the sensors utilized for the generation of the experimental data. The acquisition system uses *Yokogawa* $MX110$ analog and $MX115$ digital modules with a sampling frequency of $10Hz$. Information collected from [11].

Temperature sensors are installed at different locations, corresponding to the indices utilized in the thermodynamic cycle reported in Fig. 1.1 (see Section 1.1.1). The machine is equipped with two sensors at the compressor inlet, two at the recuperator cold leg inlet and two at the recuperator hot leg outlet. The temperatures T_1, $T_{2'}$ and $T_{4'}$ are consequently calculated as the average of the measured values. No sensor is installed at the turbine inlet (TIT or T_3). In fact, the spatial distribution of the temperature at the combustor outlet would make a single measurement irrelevant.

Unfortunately, because of space limitations (i.e. pipes too short), neither the air flow nor the exhaust gas flow rates can be measured in the facility. The measured volumetric flow rate (m^3/s) for the fuel is converted in mass flow rate (kg/s) by assuming a constant fuel density of $0.8217kg/m^3$ (value provided by the VUB research team).

The pressure is only monitored at the compressor outlet and at the recuperator inlet with differential sensors. The ambient pressure, which is not probed, is assumed to have a constant value of $101020Pa$ [28].

Thanks to the collaboration between our research team and researchers who have worked on this test rig, a set of experimental raw data, generated in 2015, was provided for the validation of the present model. The disturbance variables monitored during the test case (i.e. T_1 and P_{dem}) are reported in Fig. 5.1. Steps of $\pm 10kW_e$ and $\pm 20kW_e$ were applied to the power demand (P_{dem}) and constant power demand results were monitored for $P_{dem} = 70$, 80, 90 and $100kW_e$. The start-up phase, during which components warm-up, is not reported here.

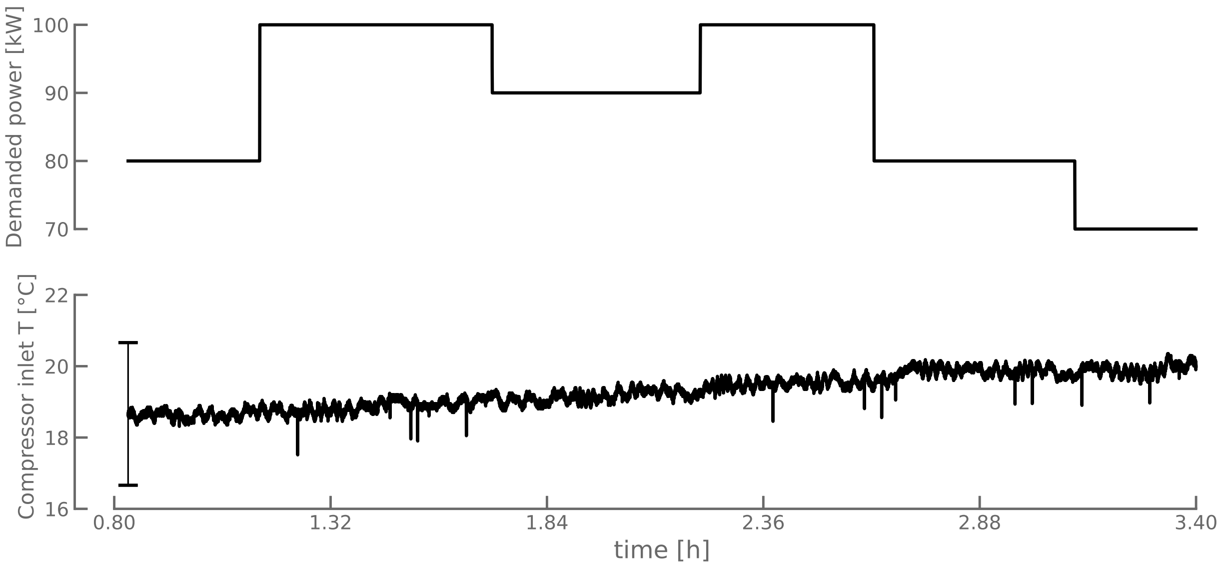

Figure 5.1: Disturbance variables during the test case. The $50min$ of start-up phase (i.e. before $\simeq 0.80h$) are not reported in the figure. The ambient pressure is assumed to have a constant value of $101020Pa$.

5.1.2 Compressor block

The calibration of the T100 compressor performances was already performed with the modelling of the maps. The only two remaining variables to be tuned are the casing mass $m_{cas,comp.}$ and its specific heat capacity c_{casing}.

Sanity check of the maps model

To ensure that the maps model provides consistent results, the latter can be tested by representing the experimental transients on the compressor map. Based on the measured inlet temperature (T_1), outlet pressure (p_2) and shaft speed (N), Figs. 5.2 & 5.3 were constructed.

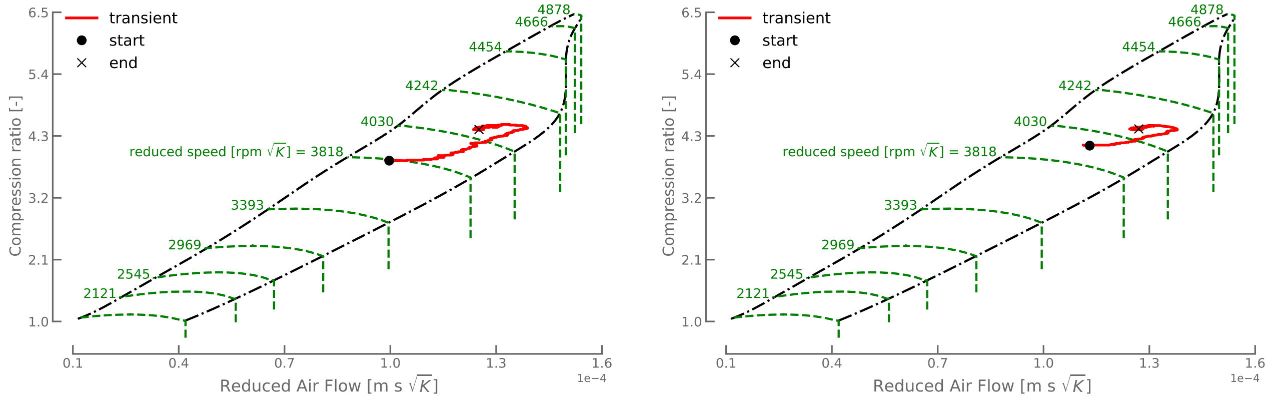

(a) 80 to $100kW$ ($+20kW$ step)

(b) 90 to $100kW$ ($+10kW$ step)

Figure 5.2: Visualization of the transients on the compressor map: positive power steps.

The typical over and undershooting paths (i.e. during transients, the air flow rate goes above or below the value of its destination point, indicated with a black cross on the maps) are caused by the way the mGT is operated. The positive power steps are associated to overshoots of about +10% in reduced air flow compared to destination point whereas the negative steps cause undershoots of about -15%.

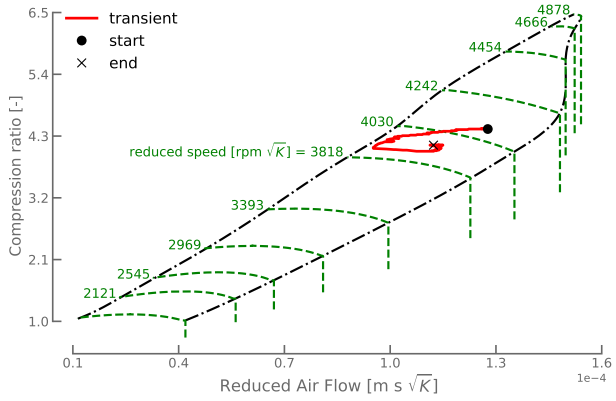

(a) 100 to $90kW$ ($-10kW$ step)

(b) 100 to $80kW$ ($-20kW$ step)

Figure 5.3: Visualization of the transients on the compressor map: negative power steps.

During the negative power steps, the air flow rate dangerously approaches the surge limit. A surge margin (SM) analysis, defined as in Eq. (2.2), is depicted in Fig. 5.4 and provides more information about the undershoots. While the minimum value that the SM should reach to

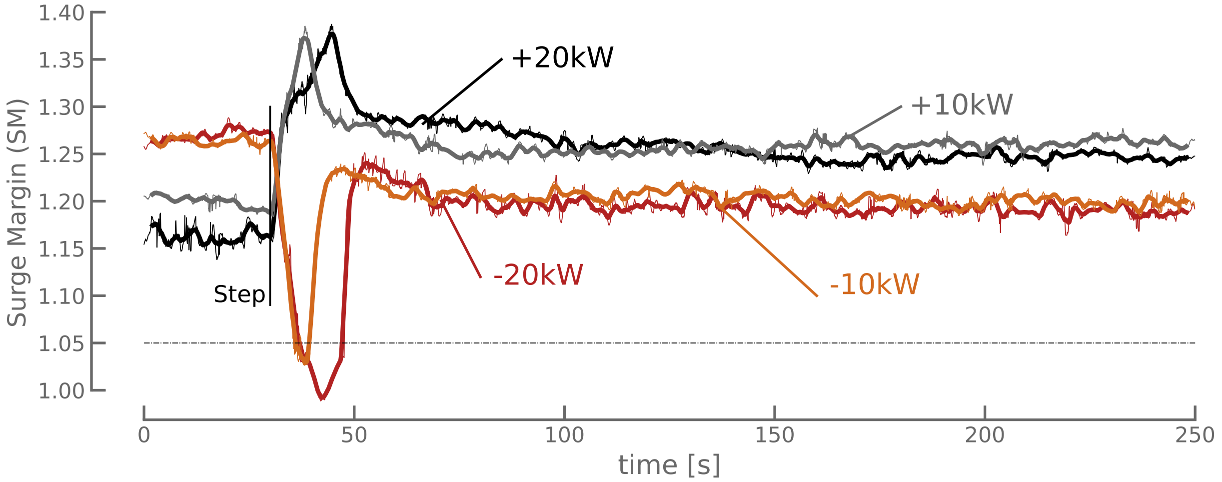

Figure 5.4: Surge margin analysis of the four transients. SM goes below the recommended stability limit of 1.05 with the negative steps.

guarantee stable operation is typically fixed at 1.05 in mGT compressors [13], the SM associated to the negative power steps crosses this limit, and even goes below 1.00, where a surge cycle could be initiated. However, although crossing the recommended limit, the compressor remains in stable operations.

Similar observations were made in our research team, and for a large set of experimental data. The map models needed to process the results were different than those utilized in this work. Nevertheless, they were constructed based on the same manufacturer maps. After discussions with the VUB research team who provided the original maps, we have assumed that the latter slightly differs from the actual compressor performances (e.g. because of eventual time degradation). The air flow rate is therefore under-evaluated with the present map model compared to the actual one.

However, the selection of the compressor inlet pressure, which has not been measured, has also been identified as a high sensitivity factor leading to these observations. Indeed, in the map region corresponding to the part load operations (e.g. $80kW$) and where the surge margin crosses the recommended limit of 1.05, the iso-speed lines are almost horizontal. Consequently, for a given rotational speed, a small change in the compression ratio causes an important deviation in the evaluated air flow rate.

Nevertheless, the current map model offers satisfying and physically consistent results in most operating cases. It will therefore not be modified, but the limitation in its part load results will be further discussed in Section 5.4.

Identification of the compressor dynamics

The dynamics of the compressor outlet temperature can now be evaluated. Ignoring the exact casing composition, it is simply assumed that its specific heat capacity is $500J/kgK$ (i.e. similar value to stainless steels).

The optimum value for $m_{cas,comp.}$ was found to be $105kg$. It was determined at the least squares sense by minimizing fitting root-mean-square error. More details and justifications about this approach are provided in Appendix E. Henke et *al.* [5] utilized a casing heat capacity of $36.7kJ/K$, which amounts at 70% of the value determined here (i.e. $m_{cas,comp.}c_{casing} = 52.5kJ/K$). The results obtained for the compressor outlet temperature (T_2) with this calibration are reported in Fig. 5.5, in comparison with the experimental data. The air composition was modelled as $[N_2] = 78\%$, $[O_2] = 21\%$ and $[Ar] = 1\%$.

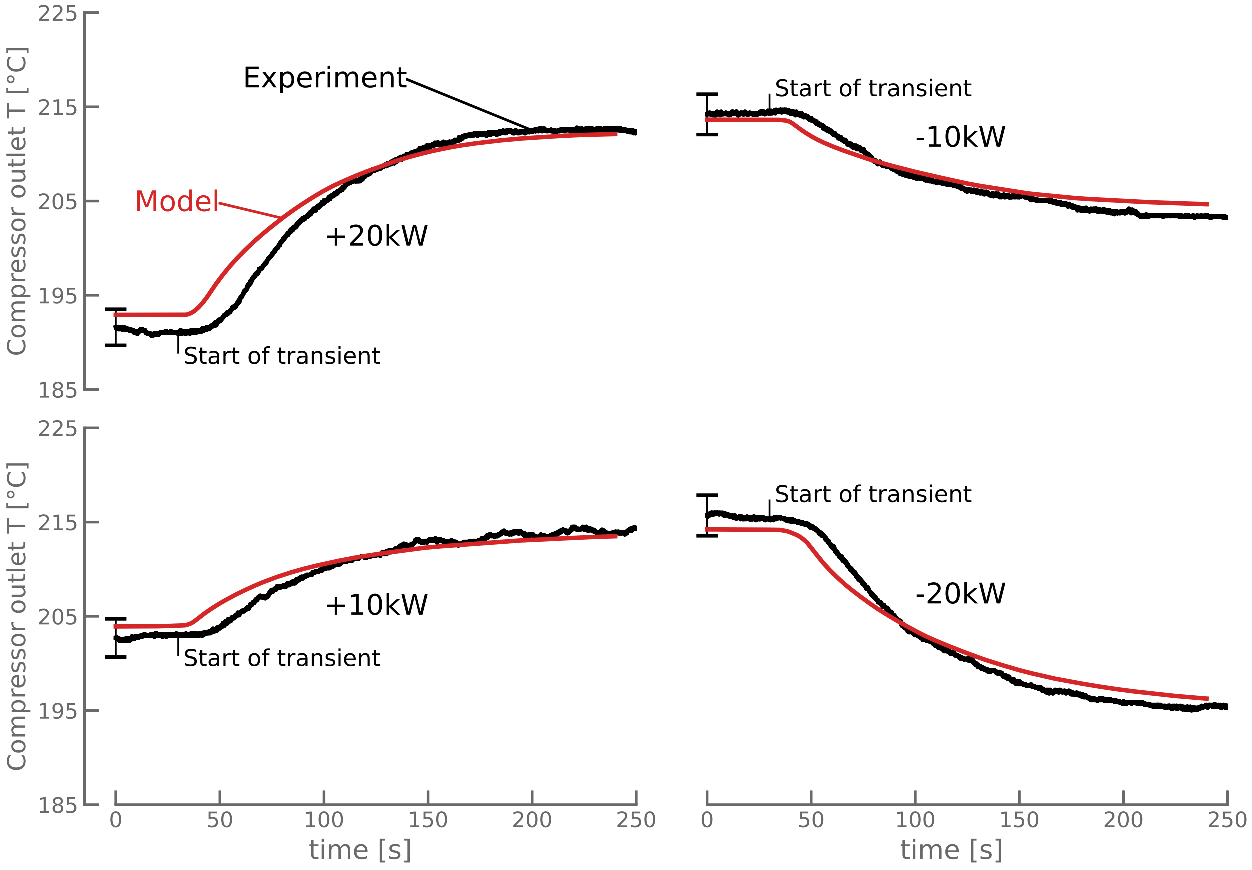

Figure 5.5: Comparison of the measured and calculated compressor outlet temperature (T_2) with $m_{cas,comp.} = 105kg$ for the different transients. The air composition was modelled as $[N_2] = 78\%$, $[O_2] = 21\%$ and $[Ar] = 1\%$.

The maximum error observed in steady state is smaller than 2^oC, which is in the range of sensor accuracy. This can be attributed to a misevaluation of the isentropic efficiency and of the inlet temperature (see Section 5.2), but also indicates that the simplified compression model, introduced in Section 3.2, is valid in the T100 operating range.

The maximum error obtained during the transients is 5^oC for the positive steps, whereas it is limited to 2.5^oC for the negative steps. These values could be further reduced by improving the dynamic model for T_2. Indeed, the assumption that the compressor outlet temperature is equal to a virtual casing temperature reaches its limit by failing to capture the delay and the inflection point in the temperature response just after the transient. This delay is particularly well visible in the $+20kW$ step. Therefore, a model accounting with more details for the conductive and convective heat transfer between the compressed air and the casing could be established.

5.1.3 Combustor block

In the combustor model, the variables related to the combustion process (combustion efficiency η_{comb}) and to the mass and energy accumulation (combustor volume V_{comb} and casing mass $m_{cas,comb.}$) must be calibrated. The pressure losses coefficient (σ_{comb}) must also be evaluated. Because the sensors available in the VUB test rig are not sufficient to derive these values from the experiments, they will be calibrated based on data published in the literature.

Identification of the combustion efficiency and combustor pressure losses

As stated in Section 3.3, η_{comb} is used to model both the combustion efficiency and the combustor heat losses. Govaerts [28] assumed constant heat losses of $10kW$ (equivalent to $\eta_{comb} = 96.9\%$ at full load) based on previous works conducted at VUB. Montero Carrero [11] compiled all the thermal losses in the system through the combustor model, with a constant value of $19kW$ (equivalent to $\eta_{comb} = 94.3\%$ at full load). Renzi et *al.* [17] chose $\eta_{comb} = 97\%$.

Based on the above considerations, a value of 97% is here selected for the combustion efficiency parameter.

Hohloch et *al.* [83] evaluated experimentally the combustor relative pressure losses (δP_{comb}) to about 5.9%. They also reported that this value was almost independent of the load point. Henke et *al.* [6] utilized $\delta P_{comb} = 5.66\%$ in their steady state model. At VUB, Govaerts [28] selected $\delta P_{comb} = 5.5\%$ and Montero Carrero [11] took $\delta P_{comb} = 5\%$.

Because it is a good trade-off between the reported values, δP_{comb} is set to 5.5% in this work. The pressure losses coefficient in the combustor is therefore calibrated as $\sigma_{comb} = 94.5\%$.

Introduction of the natural gas model

It is convenient at this stage to introduce the natural gas supplied at the VUB test rig. Its molar composition, with dominant constituents, was transmitted by the VUB research team and is reported below:

$$[CH_4] = 84.25\%,\ [C_2H_6] = 3.45\%,\ [C_3H_8] = 0.55\%,\ [C_4H_{10}] = 0.18\%,$$
$$[C_5H_{12}] = 0.10\%,\ [CO_2] = 1.19\%,\ [He] = 0.05\%,\ [N_2] = 10.23\%$$

The important amount of nitrogen limits its calorific value, with a LHV which was evaluated at $40.564MJ/kg$ by the supplier. When the input air and fuel flow rates are $0.7496kg/s$ and $8.694g/s$ respectively (i.e. full load experimental results), the flue gas composition, for the air composition provided in Section 5.1.2, is evaluated by the present model as:

$$[N_2] = 76.74\%,\ [O_2] = 17.28\%,\ [Ar] = 0.98\%,\ [CO_2] = 1.71\%,\ [He] = 0.00\%,\ [H_2O] = 3.28\%$$

The boundary conditions utilized for the fuel in this model are $p_f = 6.0bar$ and $T_f = 303.15K$. These values are assumed to be constant and were taken from [11].

Identification of the combustor dynamics

The combustor casing mass ($m_{cas,comb.}$) must be tuned to integrate the combustor outlet temperature dynamics. Govaerts [28] utilized a casing heat capacity ($m_{cas,comb.}c_{casing}$) of $5kJ/kg$ while Henke et *al.* [5] chose $14.5kJ/kg$.

Nevertheless, in the present model, it has been observed that the energy conservation on the combustor casing caused instabilities in the turbine inlet temperature, therefore impacting the entire mGT model. A large range of casing masses (i.e. from $0kg$ to $100kg$) have been tested and it turned out that the instabilities disappeared for values very close to $0kg$.

Consequently, the energy conservation on the combustor casing, represented with Eq. (3.17) (see Section 3.3), has been removed from the global system of equations formulated in Section 3.8. Therefore, with this new model, one has $T_3 = T_{gas}$. The consequences of this choice will be discussed in Section 5.3.

The combustor volume (V_{comb}), which is assumed to be constant in order to apply mass conservation equation on its control volume, is the last parameter to be identified.

If all the boundary flow rates (i.e. air, fuel and flue gas) and the combustor outlet pressure and temperature (p_3 and T_3) were measured experimentally with a high precision, V_{comb} could be tuned to minimize the fitting error for ρ_3. However, since neither the flow rates, nor p_3 and T_3 can be evaluated in the test rig, this approach cannot be selected here.

Several values have been tested during step responses. It turned out that for $V_{comb} = 5$, 20, 50 and 100 liters, the system dynamic response was very similar. Only the characteristic times were slightly impacted. More information about these tests is provided in Appendix E.

A value of $5.5422e^{-3}m^3$, corresponding to the actual combustor volume, was provided by the VUB research team. This value offered satisfying dynamic results in the global mGT model so it was kept. Govaerts [28] and Hubin [91] rather utilized $3.5e^{-3}m^3$.

5.1.4 Recuperator block

Four variables must be calibrated in the recuperator model: the global UA value, the matrix mass (m_w) and the pressure losses coefficients in both sides ($\sigma_{rec,c}$ and $\sigma_{rec,h}$). In this Section, a correlation is first established for the UA value and m_w is then evaluated with transient analyses. The coefficients $\sigma_{rec,c}$ and $\sigma_{rec,h}$ are fixed based on data proposed in the literature.

Correlation for the global UA value

A correlation for the UA value with the air flow rate is constructed from the constant power demand results, measured at 70, 80, 90 and $100kW$. The utilized boundary inlet conditions are the compressor outlet and turbine outlet temperatures (experimental) and the air and flue gas flow rates (computed as described in Section 5.1.2). Because no data is available for the expansion ratio during the operations, the flue gas flow rate can not be computed with the turbine map. It is therefore evaluated as the sum of the air and fuel flow rates (the last one being measured experimentally).

The UA value is tuned in each case to match the experimental effectiveness. The flue gas composition, required to evaluate its specific heat, is computed with the combustion model. Figure 5.6 depicts the obtained results. The left side plots represent the cold and hot legs recuperator outlet temperatures ($T_{2'}$ and $T_{4'}$). The formulation of the correlation is given in Appendix E.

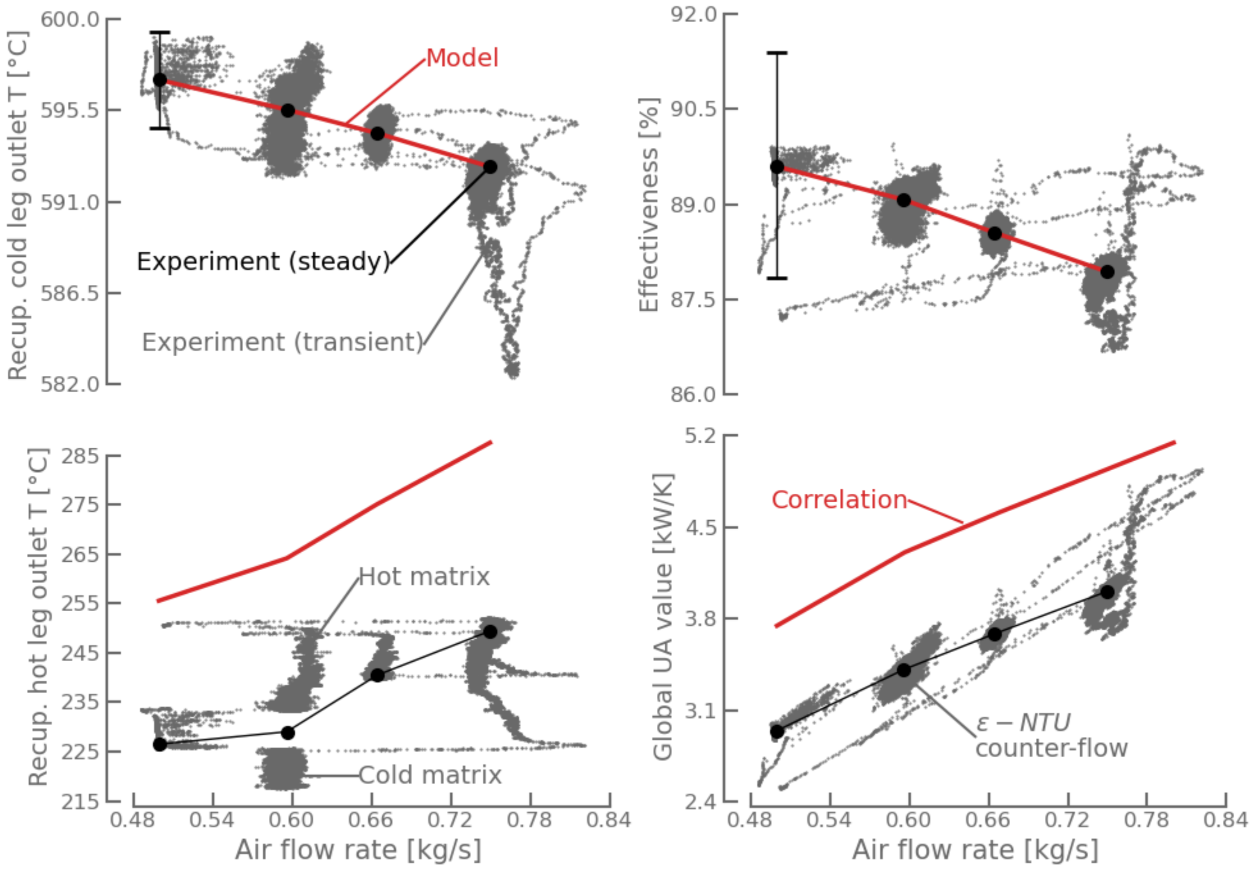

Figure 5.6: Validation of the correlation constructed for the recuperator global UA value.

Because the effectiveness is defined with $T_{2'}$, the match between the measured and calculated cold leg outlet temperatures is perfect. In contrast, there is a gap of about 30^oC at the hot leg outlet. This is attributed to the assumption that the convective heat transfer coefficient is the same in both sides (see Eq. (3.32)). This can be overcomed by defining two UA correlation (i.e. one for each side). However, since $T_{4'}$ has no impact on the system in non-CHP configuration and because of time limitation, this was not implemented in the present model.

It can also be observed in the bottom-left plot of Fig. 5.6 that the experimental $T_{4'}$ is strongly impacted by the recuperator matrix temperature. During the first period when the machine was running at $80kW$ (i.e. corresponding to an air flow rate of about $60kg/s$), $T_{4'}$ is about 20^oC lower than at then end of the experimental cycle, when all components reached their nominal operating temperature (i.e. recuperator matrix fully warmed up).

Discussion on the measured effectiveness and UA value

The upper right plot describes the measured effectiveness and the one obtained with the correlation for the UA value, depicted in bottom right plot. It can observed in the latter that the UA value computed from the experimental results with the $\epsilon - NTU$ method (see Eq. 3.30) is under-evaluated compared to the actual one (i.e. assumed to be similar to the constructed correlation). This is due to the assumption, made for the derivation of the experimental UA, that the recuperator is a full counter-flow heat exchanger, while the actual one is of mixed counter and cross-flow type. This configuration is less effective in terms of heat transfer than a pure counter-flow arrangement, so the UA value is higher for the actual recuperator.

The UA increasing trend with air flow rate is physically consistent. Indeed, the convective heat transfer coefficient is directly related to the flow velocity (i.e. related to the flow rate). The global heat transfer being essentially driven by convection, the UA value consequently increases with the air flow rate.

Let us finally observe that the measured effectiveness is smaller than the expectations reported in Fig. 3.7a (see Section 3.5). This is attributed to the ageing and the fouling of the recuperator (test rig installed for more than ten years). This can also be attributed to a partial degradation of the sensor performances with time.

Also, the typical increasing-decreasing trend with the air flow rate of high compactness recuperators is not observed here. This is attributed to the fact that the mGT was not operated at sufficient part load (i.e. lower loads than $70kW$ required). In Fig. 3.7a, the maximum effectiveness is obtained for an air flow rate of about $0.65kg/s$, corresponding to electrical loads of about $70kW$. With the observations made on the compressor map (i.e. under-evaluation of the air flow rate), it can be assumed that the effectiveness obtained here for a *computed air flow* of about $0.50kg/s$ is the maximum that can be observed.

Identification of the recuperator dynamics

The matrix mass (m_w) is obtained with the same methodology as for the compressor casing mass, and the matrix specific heat capacity is also assumed to be $c_w = 500J/kgK$.

The value offering the best trade-off between maximum and average error during the transients was determined to be $m_w = 185kg$ (see Appendix E for more details). Figure 5.7 depicts the results obtained with this calibration. For the four power steps, the maximum fitting error lays between 1.41 and 2.48^oC, while the average error is between 0.54 and 1.30^oC. These values are almost all in the range of the sensor accuracy, the latter being close to $\pm 2.4^oC$.

The offset error, particularly visible in the $+10kW$ step, is attributed to a misevaluation of the UA value. The latter was indeed computed such that only one value was attributed to each air flow rate while small deviations around this single values are observed experimentally (see Fig. 5.6). This error could also be partly attributed to a misevaluation of the hot gas flow rate (see previous paragraphs for its evaluation).

Identification of the pressure losses coefficients

No pressure sensors are installed at the recuperator boundaries. It is therefore not possible to establish a correlation between the air flow rate and the pressure losses inside the recuperator based on the VUB data.

Fortunately, some scholars proposed an evaluation of the relative pressure losses (δP). In her model, Montero Carrero [11] utilized $\delta P_{rec,c} = 4.98\%$ and $\delta P_{rec,h} = 1.90\%$. Henke et *al.* [6] identified separately 3.48% of pressures losses inside the pipe network between the compressor outlet and the recuperator inlet, and 2.18% inside the recuperator cold side. In our model, this can be interpreted as $\delta P_{rec,c} = 5.66\%$. They also utilized linear correlations with the volumetric flow for the pressure losses in the hot side and outlet pipe, and evaluated them at $630.7Pa/(m^3/s)^2$ and $323.4Pa/(m^3/s)^2$ respectively. In a paper published two years later [5], they chose $\delta P_{rec,c} = 2.04\%$ (without pipe network) and $\delta P_{rec,h} = 2.73\%$

In this work, it is decided to use $\delta P_{rec,c} = 5\%$ and $\delta P_{rec,h} = 2\%$ because these values provide a good match with the experimental results. Therefore, the pressure losses coefficients defined in Section 3.5 are calibrated as $\sigma_{rec,c} = 95\%$ and $\sigma_{rec,h} = 98\%$.

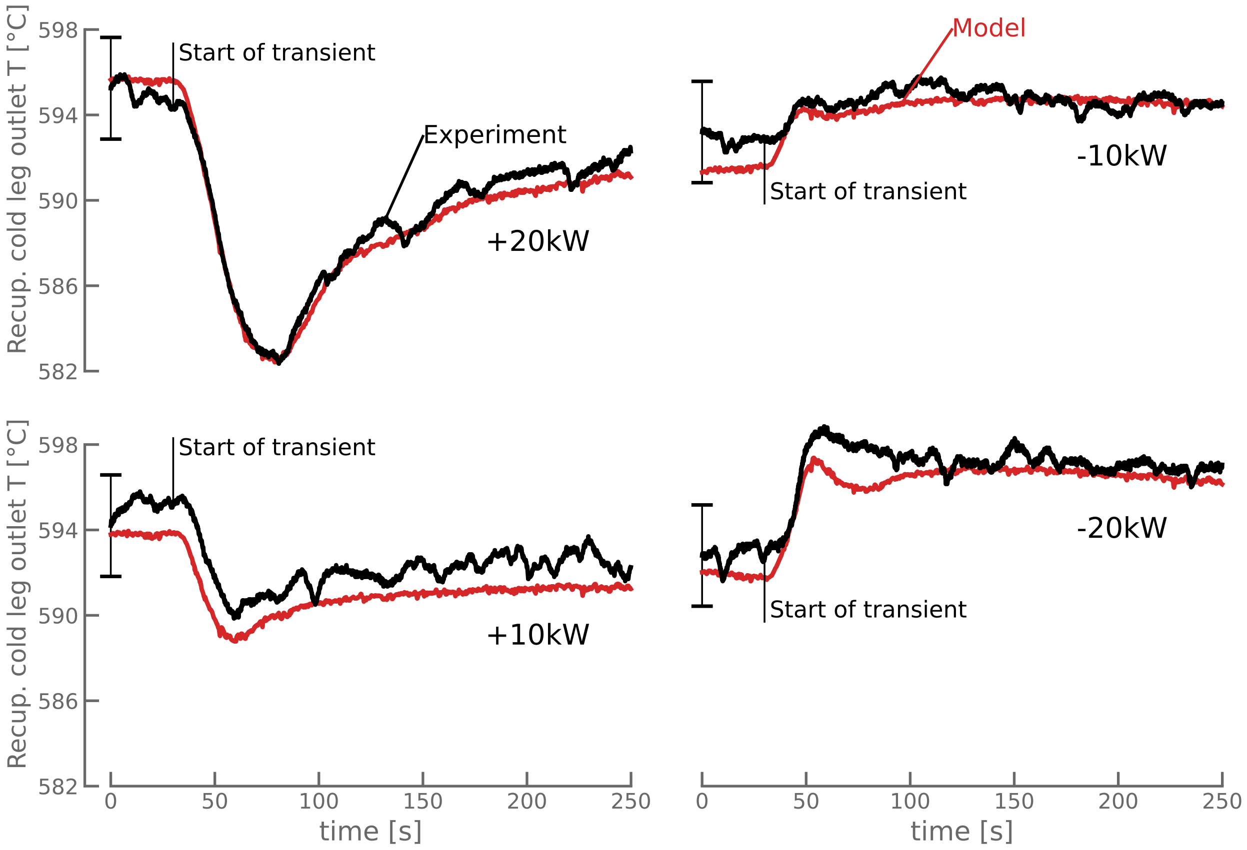

Figure 5.7: Comparison of the measured and calculated recuperator cold leg outlet temperature ($T_{2'}$) with $m_w = 185kg$ for the different transients.

5.1.5 Turbine block

Ideally, the same methodology as for the compressor should be applied to determine the turbine casing mass ($m_{cas,turb.}$). Unfortunately, none of the boundary conditions needed for that aim are measured experimentally.

Although the pressure levels, flue gas flow rate and composition could be estimated with the calibrated model presented in the previous Sections, the turbine inlet temperature is the main unknown. The latter could also be processed with the developed model, but the uncertainty brought by all these estimations would make an accurate calibration of $m_{cas,turb.}$ irrelevant. Therefore, it will be roughly estimated based on calibrations proposed by other authors.

Govaerts [28] utilized the same model as the present one for the casing energy conservation. He selected a casing heat capacity ($m_{cas,turb.}c_{casing}$) of $12.25kJ/K$ to ensure the numerical stability of his model. Henke et *al.* [5], who constructed a similar model, identified experimentally a value of $61.1kJ/K$ to give to the TOT the correct dynamics.

Since the compressor casing heat capacity obtained in this work was relatively close to that of Henke et *al.* (i.e. relative difference of 30%), the value of $61.1kJ/K$ is picked-up from their model for the present one. With $c_{casing} = 500J/kg$, this gives $m_{cas,turb.} = 122.2kg$.

5.1.6 Shaft block

Two models for the auxiliaries consumption (P_{aux}) were introduced in Section 3.6. In the T100 installed at VUB, P_{aux} is not taken into account by the control system when computing the load to be applied to the generator (P_{load}). This means that the power supplied to the electrical grid (P_{elec}) is lower than the demanded power (P_{dem}). Therefore, the second approach for the shaft power balance is selected for the current model.

Consequently, four variables have to be calibrated in the shaft block. First, correlations must be established for the *bearing losses* (P_{lb}), that account for bearings friction and for some eventual air friction, and for the *electrical losses* (P_{le}), accounting for the generator and power-electronic losses. The shaft moment of inertia (I) must also be evaluated. The auxiliaries consumption, although non-participating to the shaft dynamics, will be calibrated here as well.

Bearing losses correlation

Friction losses are typically evaluated experimentally with deceleration tests. However, a proper application of these tests requires a very accurate knowledge of the shaft moment of inertia. Since it is unknown at this stage, this technique is not applicable. Nevertheless, from the friction theory, it can be established that the *bearing losses* of our model have a quadratic relationship to the shaft speed and can be expressed as

$$P_{lb} = a_1 N + a_2 N^2 \; , \tag{5.1}$$

where a_1 and a_2 are two user defined constants. Hubin [91] and Govaerts [28] have chosen to establish a linear correlation for these losses with the shaft speed. They assumed that P_{lb} had a value of $1kW$ at $70,000rpm$ (i.e. this value was apparently reported by the manufacturer but could not be verified in this work). Therefore, they obtained $a_1 = 14.28e^{-3}[W/rpm]$ and $a_2 = 0$. Henke et *al.* [5] calibrated their model to meet the measured electrical power output. They obtained $a_1 = 21.33e^{-3}[W/rpm]$ and $a_2 = 0$, what is equivalent to $P_{lb} \simeq 1.5kW$ at full load. A comparison between both models is illustrated in Fig. 5.8. Because Henke's model is based on experimental observations and not on assumptions that could not be verified here, it is selected for this work. Let us note that Traverso [21] utilized a model with the same magnitude order for the bearing losses (i.e. $P_{lb} \simeq 0.9kW$) in a Bowman TG-45.

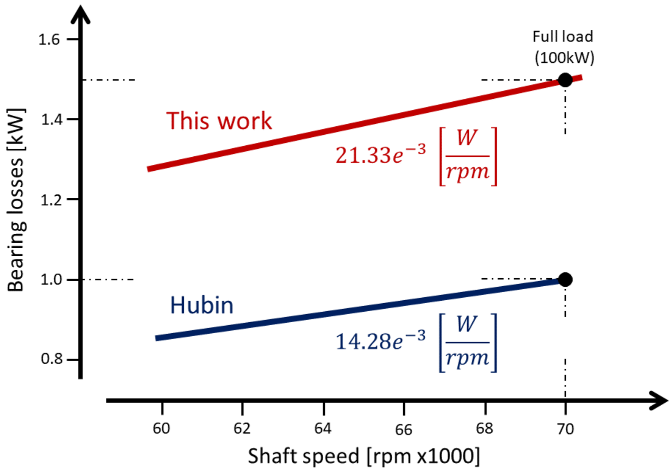

Figure 5.8: Proposed correlations between the bearing losses and the shaft speed.

Correlation for electrical power losses and auxiliaries consumption

As stated earlier, P_{le} accounts here for the generator and power-electronic losses. However, in order to assess the global system efficiency, P_{aux} must also be evaluated. According to [3], the latter are mainly driven by the fuel compressor. It has also been observed by [6] that this consumption is nearly constant in all operating conditions and would have a value of about $3.5kW$ (i.e. value deduced from an experimental correlation constructed by Henke et *al.* [5]). However, experimental observations made with the data collected at the VUB test rig rather suggest that P_{aux} is not exactly constant. A correlation expressed as

$$P_{aux} = -5.0802e^{-3} P_{load}^3 + 2.3891 P_{load}^2 - 2.3492e^2 P_{load} + 8.3781e^3 \; , \tag{5.2}$$

is built between P_{aux} $[W]$ and P_{load} $[kW]$. For $P_{load} = 100kW$, this gives $P_{aux} \simeq 3.7kW$, which is close to the value proposed by [5]. Renzi et *al.* [17] suggested that the fuel compressor consumption was about $3kW$ at full load, meaning that P_{aux} is essentially driven by this fuel booster. The constructed correlation and the experimental data are represented in Fig. 5.9.

Some authors also proposed models for P_{le}. Henke et *al.* [5] constructed a global correlation for P_{le} and P_{aux}, as a function of the generator mechanical input power (P_{gen}). The latter is expressed as

$$P_{le+aux} = 3473 + 0.0812 P_{gen} + 2.67e^{-7} P_{gen}^2 - 4.48e^{-12} P_{gen}^3 \ , \tag{5.3}$$

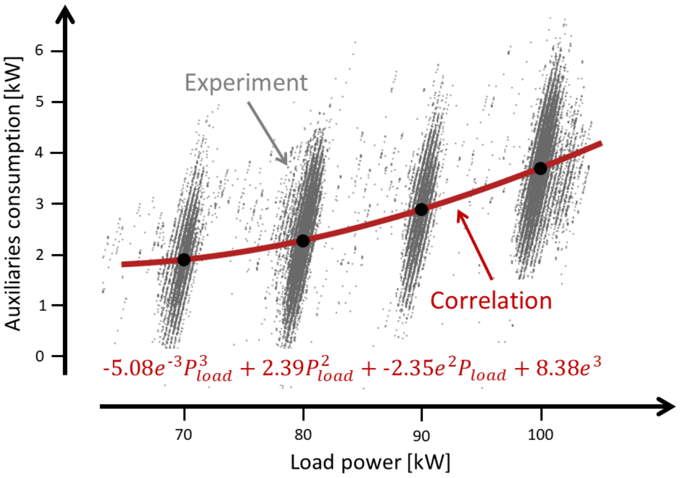

Figure 5.9: Proposed correlation between the auxiliaries consumption and load power.

with the powers expressed in W. Montero Carrero [11] proposed to model the generator with an electrical efficiency of 99% and the power electronics with a conversion efficiency of 95%. A combined value of 94% for them both has also been reported by [9]. Because these values have already been used by the VUB research team in different models, they were selected for this work. Figure 5.10 represents the different power lower losses as functions of P_{gen}. The blue curve on the top illustrates the correlation constructed by Henke et *al.* [5] for P_{le} and P_{aux}. The blue curve in the bottom illustrates the model for P_{le} utilized by the VUB research team. Finally, the red curve stands for the model utilized in this work for P_{le} and P_{aux}. At full load (i.e. $P_{elec} = 100kW_{el}$), the total conversion losses between the shaft mechanical power and the electrical power delivered to the grid are about $10.7kW$.

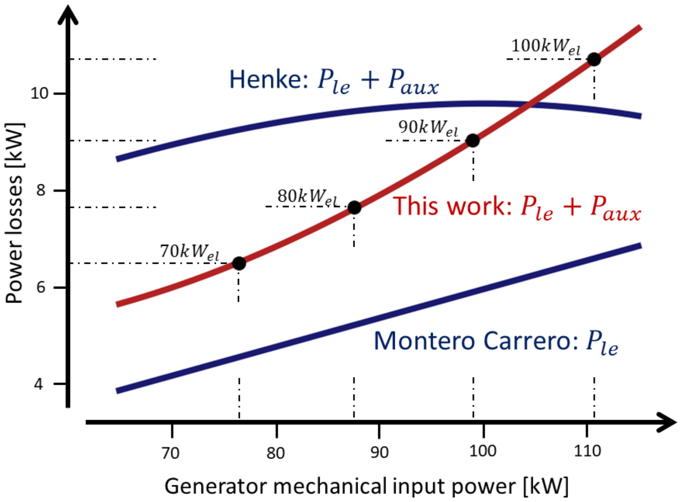

Figure 5.10: Correlations proposed between the power losses and generator mechanical input power.

Determination of the shaft moment of inertia

The last parameter to be identified is the shaft moment of inertia (I). When all the loads applied to a shaft are known with a high precision, this value can be deduced from deceleration tests. However, as it has been described in the previous paragraph, our knowledge about these loads is rather empirical and approximate. A theoretical derivation of the shaft moment of inertia is also complicated due to its complex shape.

Figure 5.11 was constructed to compare some values obtained from an extensive literature review, for different machines. The initial goal, when constructing this figure, was to establish a correlation between the shafts inertia and the mGTs nominal power, and to pick-up a value for our machine. However, it turned out that there is no convergence for the shafts inertia, even for the same machines.

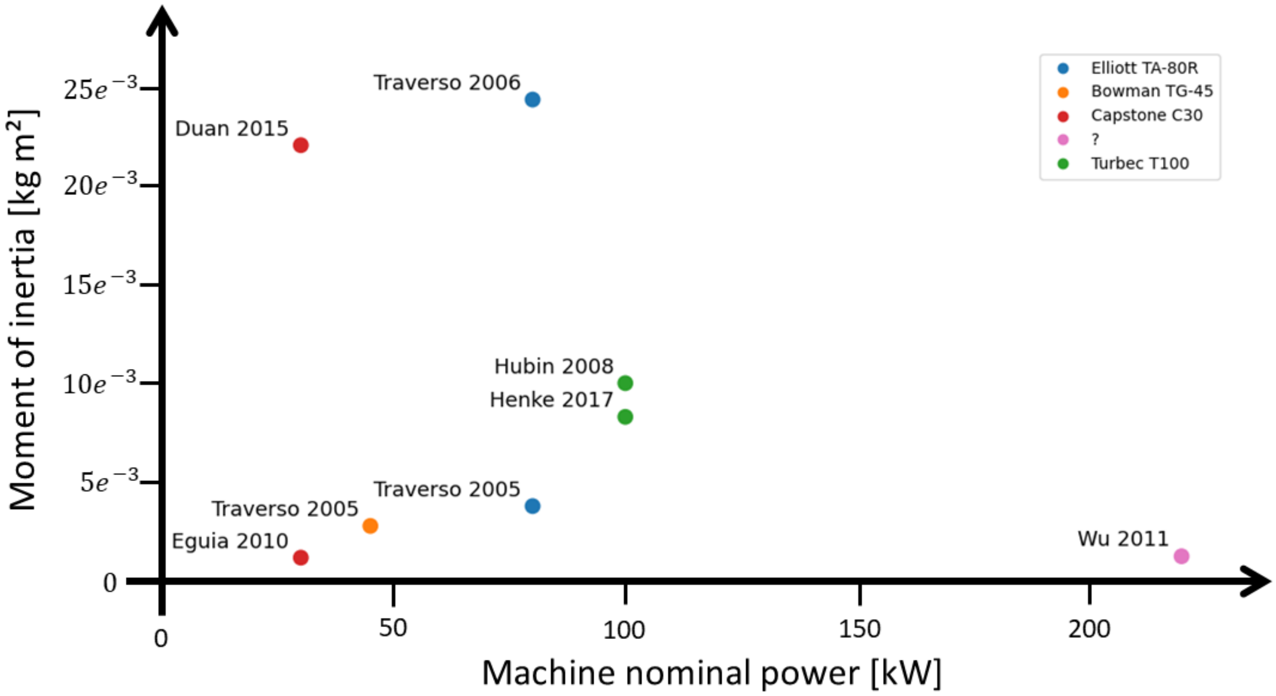

Figure 5.11: Moments of inertia utilized in different models for a small variety of mGTs. The outliers, like $I = 0.09 kgm^2$ utilized by He et *al.* for the C30 [92], are not reported for the figure clarity. References to these values are: [5, 15, 16, 18, 21, 22, 32, 91].

In fact, there is no clear agreement on the procedure to determine this value. Although it is sometimes obtained from experimental measurements [21], it is most of the time tuned inside the model to match experimental results.

A clear example to illustrate the difficulty to obtain a precise value for I is that Traverso et *al.* [15, 16] utilized two different I, with one magnitude order of difference, for the same machine (i.e. Eliott TA-80R), in an externally firing application. Because of the limited explanation on the way these values have been determined, it is difficult to establish the reason for this significant update.

As illustrated, it is difficult to obtain a clear value for the moment of inertia, although it has a major impact on the system dynamics. However, because of the very good dynamic results obtained by Henke et *al.* [5], and because of the similarity between our shaft power balance models, it is decided to reuse their value of $I = 8.3e^{-3} kgm^2$.

5.1.7 Controller block

The control system, briefly introduced in Section 3.7, was relatively complex to implement in the `Python` numerical model, compared to how this could have been carried in other languages allowing for block programming and transfer function formulation (e.g. `Simulink`). However, this was successfully achieved, thanks to the use of global variables (i.e. `Global var. module`).

The controller utilizes reference tables and gains, originally calibrated by the manufacturer for an actual machine. With the present model, this calibration of the parameters has led to instabilities in the control variables (i.e. P_{load} and $\dot{m}_f$), for any set of disturbance variables (i.e. p_{amb}, T_{amb} and P_{dem}) subjected to tiny perturbations (e.g. steps of $0.1 kW$ in P_{dem}).

Multiple tentatives of re-tuning were made, but due to time restriction, it has not been possible to stabilize the control system within the frame of this Thesis. As it will be illustrated in Section 5.3, the rather unstable and very sensitive nature of the constructed system complexifies the adjustment of the controller parameters.

Govaerts [28] encountered similar issues with his `Simulink model`. However, he managed to re-tune the control system parameters provided by the manufacturer in order to obtain stable results. This suggests that the present model could, with sufficient effort, be stabilized too.

Therefore, the dynamic results, that are presented in Section 5.3, were obtained without the implemented control system. In that Section, the very sensitive nature of the constructed system is also thoroughly discussed.

5.2 Steady state results

Steady state results have been computed with the calibrated model for four different load points: 70, 80, 90 and $100kW$. They were obtained by tuning the fuel flow rate such that the TOT matches the value of 645^oC, the latter being prescribed by the control system.

This Section first reports the simulated part load results and the associated operating lines on the compressor and turbine performance maps. They are compared to the experimental results and the deviation between them is justified.

Thereafter, all the measured and simulated operating parameters are compared and discussed, and the relative deviation between them is finally summarized on bar charts. As many of the discussion points have already been addressed during the calibration in Section 5.1, these will only be briefly recalled here.

The relative error (δ_{rel}), or relative deviation, which will be utilized for the comparisons between simulations and experiments, is defined as

$$\delta_{rel} = \frac{|x_{experiment} - x_{simulated}|}{x_{experiment}} \cdot 100\% \, , \tag{5.4}$$

with $x_{experiment}$ and $x_{simulated}$, the experimental and simulated values in SI units respectively.

5.2.1 Representation on the performance maps

The experimental and simulated results are reported on the compressor and turbine performance maps in Fig. 5.12. The experimental data were processed before being depicted. Indeed, since no flow meter is installed in the VUB test rig, the air flow rate was deduced from the inlet temperature, the shaft speed and the compressor outlet pressure, with the compressor map model.

At full load, there is a good agreement between the experimental and simulated results (i.e. $\delta_{rel} = 0.4\%$ for the compression ratio and 0.8% for the reduced air flow). At part load, the compression ratios are similar, with a maximum relative deviation of 1.1% at the $70kW$ point (i.e. left end side of the operating line).

However, there is a large deviation in the reduced air flow for the part load results. The experimental operating line gets indeed closer and closer to the surge line (i.e. which is in contrast with usual operations of mGT compressors [3]), while the simulated line remains more or less parallel to the choke line (i.e. as for a traditionally operated compressors [3]).

This important deviation is assumed to be caused by the processing of the experimental data. As stated in Section 5.1.2, the misevaluation of the air flow rate is attributed to inaccuracies of the original compressor map, compared to its actual performances. With this supposition, the actual air flow rate, which has never been measured in the test rig, is probably higher and closer to the simulated one. Therefore, with a corrected map version, it is assumed that the measured and simulated results would be much closer to each other.

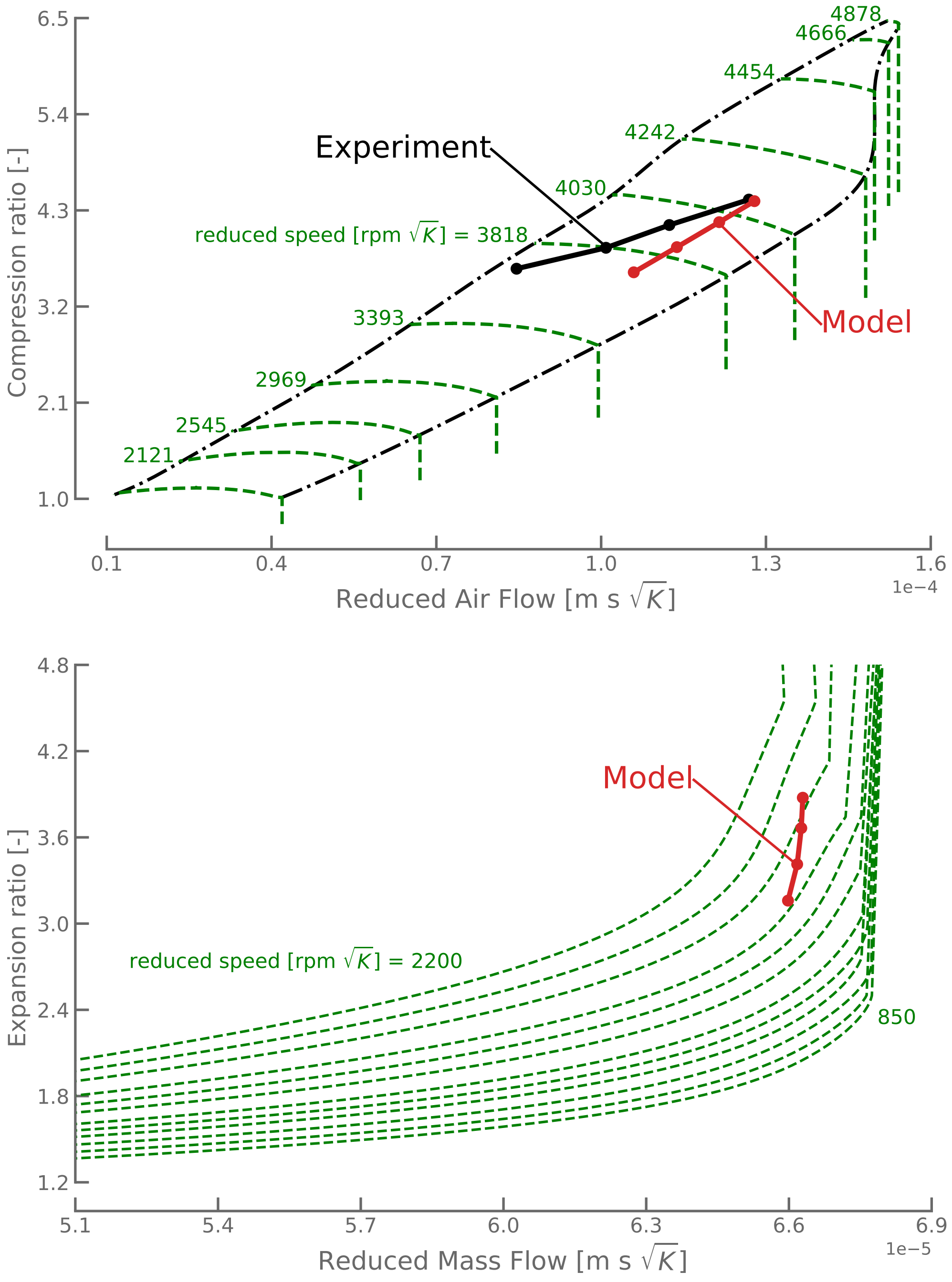

Figure 5.12: Experiment and model operating lines on compressor and turbine maps. The experiment line was deduced from the available data (i.e. T_1, p_2 and N).

Let us finally note, for the comparison, that Renzi et *al.* [17] and Caresana et *al.* [3] reported very similar results to the simulated ones, on their own compressor and turbine map models.

5.2.2 Comparison between measured and simulated results

As it will be illustrated, the full load results show an excellent agreement, but there is a more important deviation at part loads, which is attributed to the misevaluation of the actual turbomachinery performances.

The excessive simulated fuel consumption compared to experiments will also be thoroughly discussed.

Shaft speed and compressor outlet conditions

The simulated and measured shaft speeds at part load are reported in Fig. 5.13. At full load, the match is excellent (i.e. deviation of $9rpm$, $\delta_{rel} = 0.01\%$).

The deviation in the part load results is first attributed to the misevaluation of the actual compressor and turbine performances by their maps. Another part of the justification is associated to the the pressure levels. Indeed, as the pressure in the system is related to the shaft speed through the performance maps, a deviation in it results in a deviation of the shaft speed.

However, the maximum error in compressor outlet pressure is limited to $0.04bar$ (i.e. $\delta_{rel} = 1.1\%$). The second explanation therefore does not justify the large deviation in shaft speed, but suggests that a correlation for the pressure losses coefficients at part load could improve the model accuracy.

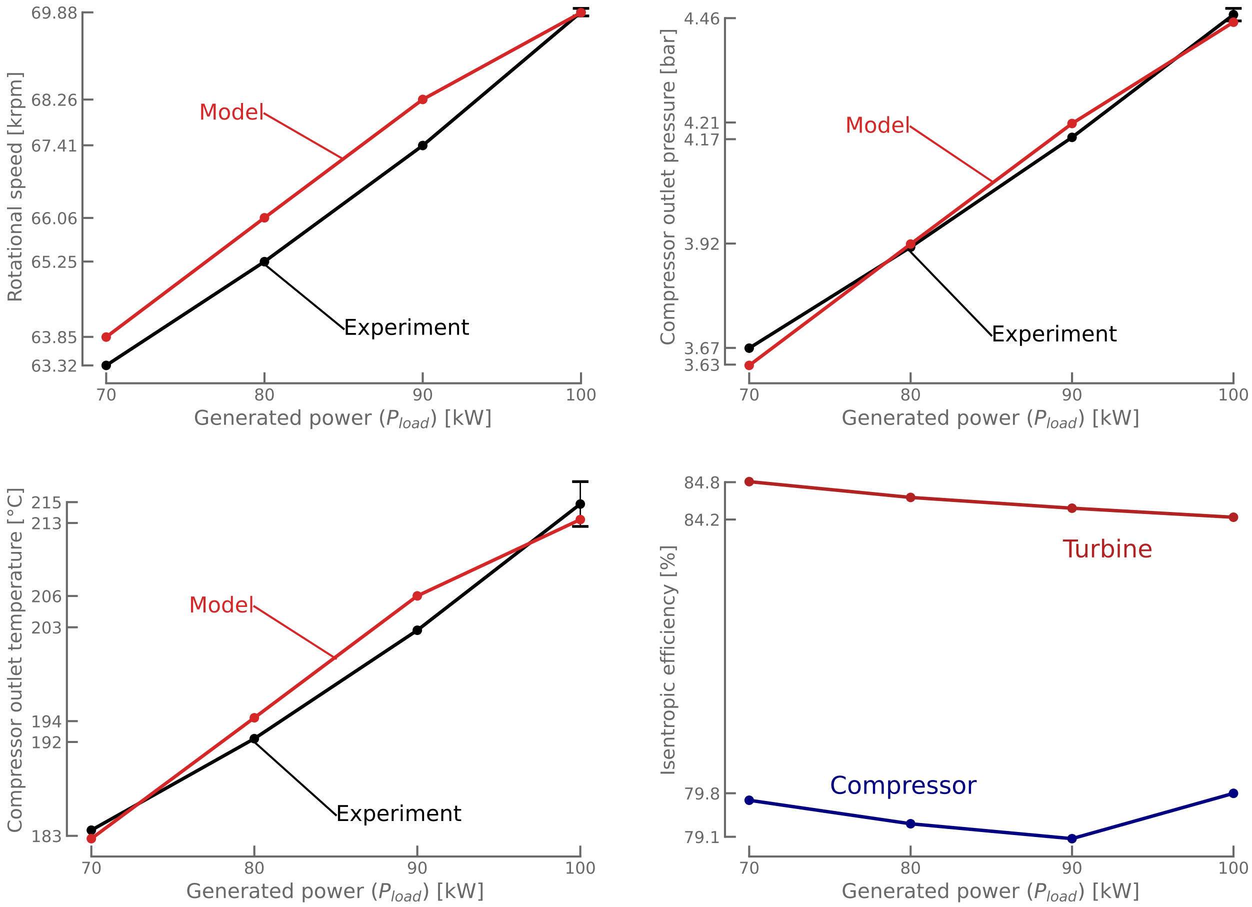

Figure 5.13: Measured and simulated static results: shaft speed and compressor outlet conditions.

The maximum error in compressor outlet temperature is 3.3^oC (i.e. $\delta_{rel} = 0.7\%$). This deviation is first attributed to the different compression ratios (i.e. similar deviations for compressor outlet pressures and temperatures). The positive deviation in the simulation results is also attributed to the simplified compression model (i.e. defining the heat capacity ratio with the inlet temperature only), which over-estimates the compressed air temperature. Finally, a misevaluation of the compressor isentropic efficiency is a potential third justification for this deviation.

The discontinuity in speed, pressure and temperature operating lines can also be analysed through the prism of the compressor isentropic efficiency. As it can be observed in the bottom right plot of Fig. 5.13, $\eta_{is,c}$ is almost linearly decreasing from 70 to $90kW$, threshold above which it increases to reach a 0.7% higher value at full load.

From the observations drawn here, it can be concluded that the compressor map is true to the actual performances at full load, but needs corrections at part loads.

Recuperator outlet temperatures and effectiveness

Figure 5.14 depicts the recuperator cold and hot legs outlet temperatures, as well as its effectiveness for different loads. The best matches are again obtained at full load.

The deviation of the simulated cold leg temperature compared to experiments was not expected, given that the fitting observed during the calibration was extremely good (see Fig. 5.7). No conclusive explanation was found to justify this. However, the turbine outlet temperature is supposed to play a role in this. To support the hypothesis that $T_{2'}$ is constant because of the TOT, Eq. (3.38) involves the assumption that the part load variation of the heat transfer coefficient (see Fig. 5.6) is perfectly compensated by the variation in air flow rate.

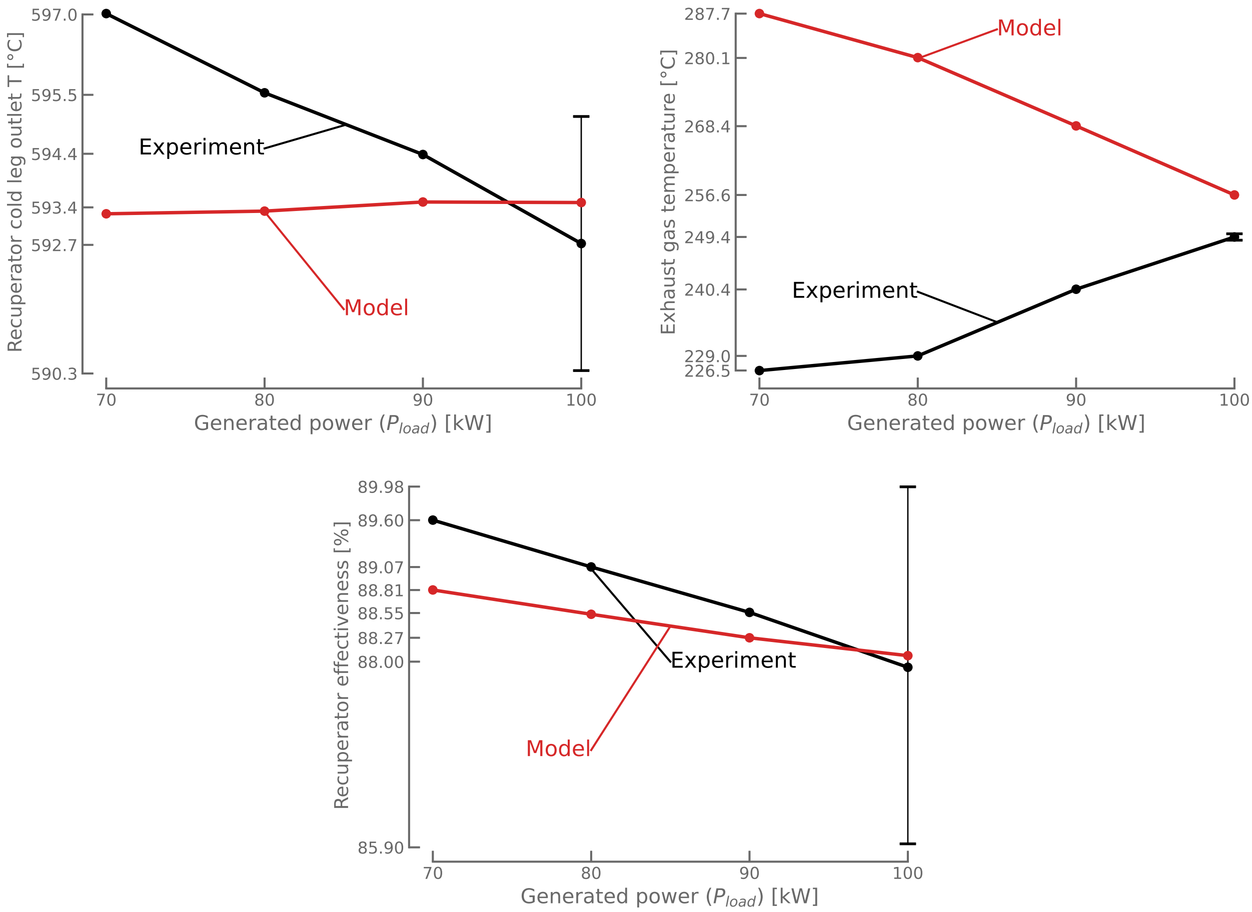

Figure 5.14: Measured and simulated static results: recuperator temperatures and effectiveness.

The deviation in exhaust gas temperature is attributed to the assumption that the heat transfer coefficient is the same in both and hot sides, as it has been explained in Section 5.1.4.

The deviation in effectiveness is attributed both to the error made on the compressor outlet temperature (max. excess of 3.3^oC) and to the error on the recuperator outlet temperature (max. lack of 3.7^oC), resulting in a lower effectiveness (max. lack of 0.79%).

Fuel consumption and roundtrip efficiency

Figure 5.15 depicts the measured and simulated fuel consumption, and the corresponding mGT roundtrip electrical efficiency. The latter is defined as

$$\eta_{elec} = \frac{P_{el}}{\dot{m}_f LHV} = \frac{P_{load} - P_{aux}}{\dot{m}_f LHV} \ , \tag{5.5}$$

with P_{el} the net electrical power output, P_{load} the generated power (i.e. at the power electronics output) and P_{aux} the auxiliaries consumption.

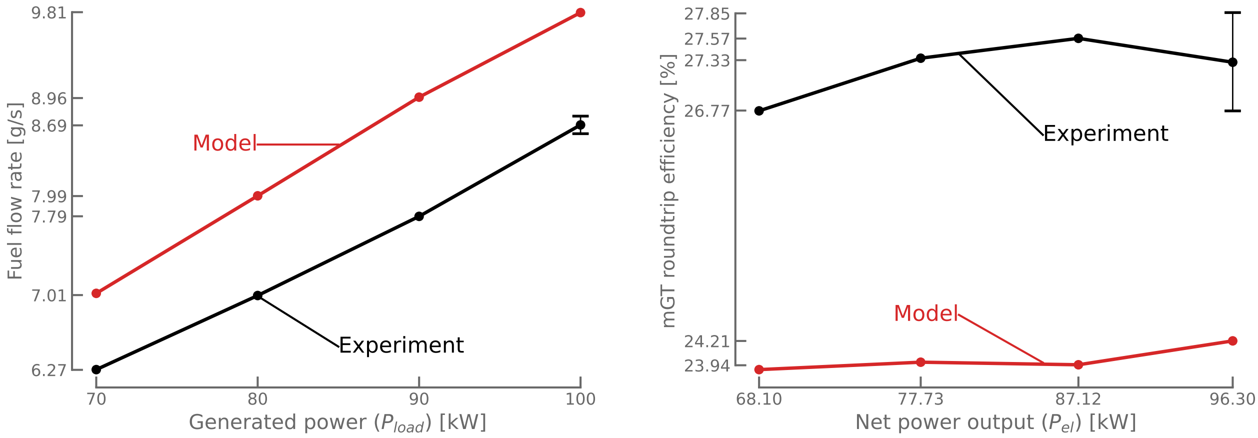

Figure 5.15: Measured and simulated static results: fuel flow rate and mGT roundtrip efficiency.

As it can observed in the left plot, the simulated system over-consumes on average $1g/s$ of fuel compared to the experiments (i.e. $\delta_{rel} = 13.5\%$), while the same TOT was applied. The origin of this problem was identified since the early stages of this project, when comparing the simulated steady state results with some data published in the literature. It is attributed to the thermodynamic model utilized in this tool.

Indeed, several tests were conducted to evaluate the energy balance on the combustor (see Eq. (3.15)) and to validate, with the present combustion model, the operating conditions reported in the literature (see Section 3.3.2). It turned out that, for all the steady state boundary conditions that were tested, the energy conservation on the combustor control volume was systematically violated, with a lack of input power (i.e. sometimes reaching values up to about $90kW_{th}$).

The thermodynamic tables utilized by `CoolProp` in the `Thermo` *`module`* were validated against others. Particularly, the tables for H_2O, which were first identified as a potential problem origin, showed an excellent agreement (see Appendix E for more details). However, the treatment of humid air and gaseous water in the flue gas is still perceived as a possible origin for this issue.

After a relatively important time devoted to investigations, it has been decided to continue the model development, while being aware of this problem, which is still unresolved to date.

5.2.3 Steady state validation with relative error bar charts

The relative deviations between the simulated and experimental results, which have been introduced in the previous Section, are an effective way to validate the model. They are reported on the bar charts in Fig. 5.16.

The roundtrip efficiency, exhaust gas temperature and fuel consumption have been separated from the rest for clarity. The reasons for their important deviation are, as discussed above, the issue with the thermodynamic model when performing the energy balance on the combustion chamber and the assumption that the heat transfer coefficient is the same on both sides of the recuperator.

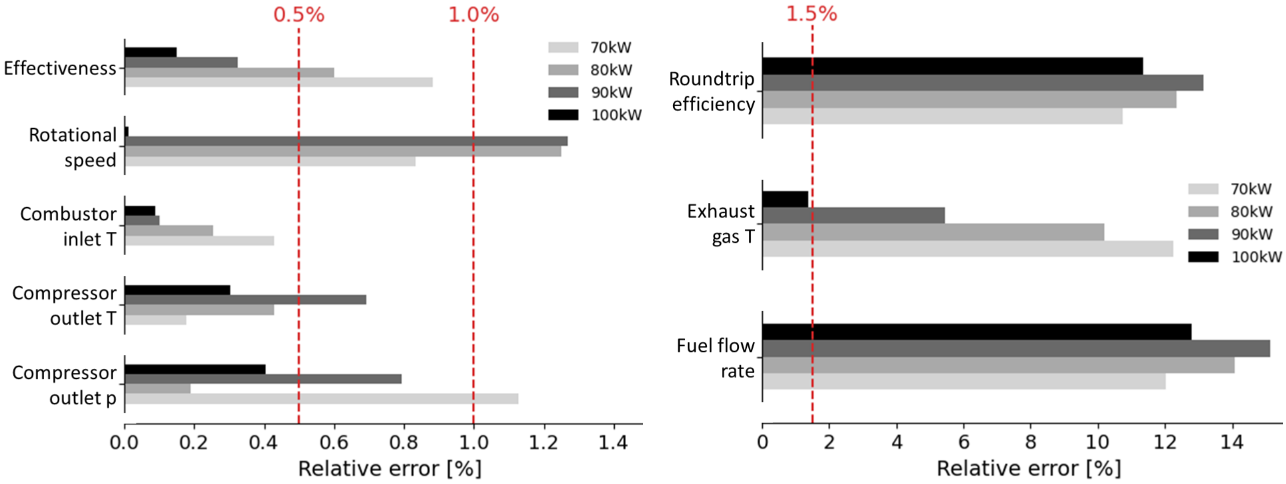

Figure 5.16: Model relative errors with respect to experimental data computed in SI units.

The left plot shows that the steady state relative error is below 1% for most variables that were measured experimentally. The full load results all have a deviation lower than 0.5%, which proves that the calibration was successfully achieved for this point.

The relatively more important deviation in rotational speed has been discussed multiple times and is attributed to the inaccuracy of the performance maps. The deviations in compressor outlet pressure are due to the assumption of constant pressure losses coefficients.

Let us finally observe that the recuperator model provides extremely accurate values for the combustor inlet temperature.

5.3 Dynamic results

As stated in Section 5.1.7, within the frame of this Thesis, time restrictions did not allow for a fine tuning of the control system. It is therefore not possible to reproduce the experimental test cases introduced in Section 5.1.1 with the numerical tool.

Therefore, this section first presents open-system step responses to transients in fuel and load power, in order to identify the mGT dynamic behavior.

Thereafter, pseudo-controlled transient maneuvers from $90kW$ to $85kW$ are introduced. These were constructed by reproducing the controller behavior, as it was observed in experiments.

5.3.1 Open-system step responses

Figure 5.17 represents the transient conditions that were applied to the control variables (i.e. fuel flow rate and load power) and the corresponding shaft speed response.

The present test case is intended to represent a transient maneuver form $100kW$ to $99kW$, and the control variables are set as:

- ***Fuel flow rate***: decreased from its $100kW$ to $99kW$ steady state value with a ramp of $-0.679kW_{chem}/s$ (i.e. chemical power deduced from LHV);
- ***Load power***: decreased from $100kW$ to $99kW$ with ramps ranging from $-0.105kW/s$ to $-0.2kW/s$.

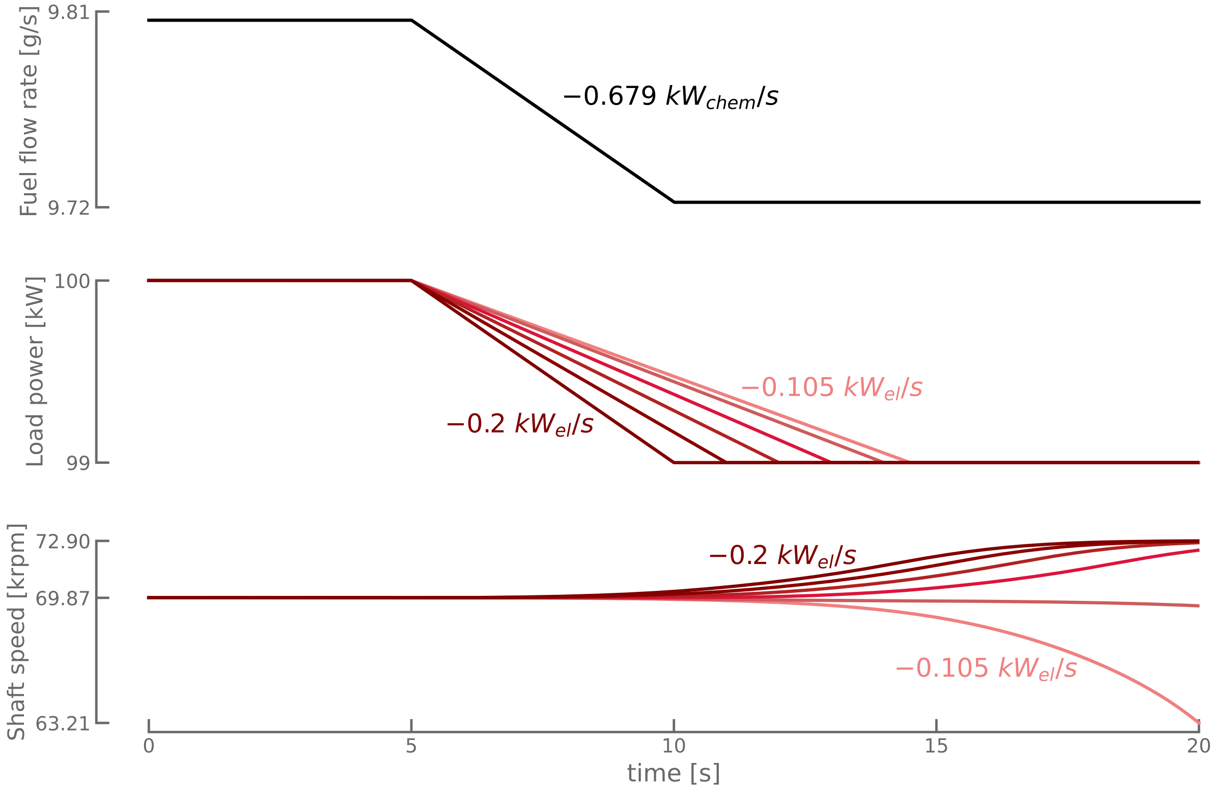

Figure 5.17: Control variables and shaft speed response during transient maneuver from $100kW$ to $99kW$. The coloured curves represent the mGT response with the different control settings.

From the shaft speed responses, which represent the whole system behavior, it turns out that the system is very sensitive to disturbances. The value of $72.90krpm$ reached by the speed corresponds to a user defined upper bound in the maps model (i.e. in the original maps regions where no information was provided). The speed response of the three upper curves during the last five seconds is therefore not physical.

Very few information addressing the mGTs natural high sensitivity and unstable behavior were found in the literature. In most papers introducing dynamic results, both simulated and experimental transients are carried out with the controller, and the latter permanently regulates the system.

From the present simulated results, it can therefore not be firmly concluded that the T100 is a naturally unstable system. The observed very high sensitivity could also be attributed to the combustor model high complexity. Indeed, the complexity involved with the iterative computation of the combustion could generate instabilities, as this had been observed for the interaction with the energy conservation on the combustor casing (see Section 5.1.3). This will be further discussed in the next Sections, where overcoming strategies will be suggested.

The model complexity is also induced by the compressor map model, requiring the resolution of elliptical equations at each time step.

However, since one of the obtained step responses is relatively stable compared to the others, this suggests that the system could be controlled and stabilized. This is verified in the next section, by mimicking the actual controller behavior.

5.3.2 Pseudo-controlled maneuver from $90kW$ to $85kW$.

Figure 5.18 represents the system responses when mimicking the controller strategy in a transient maneuver from $90kW$ to $85kW$ (i.e. bounds selected for obtaining a stable response). The overshoot in load power is intended to initiate the shaft deceleration.

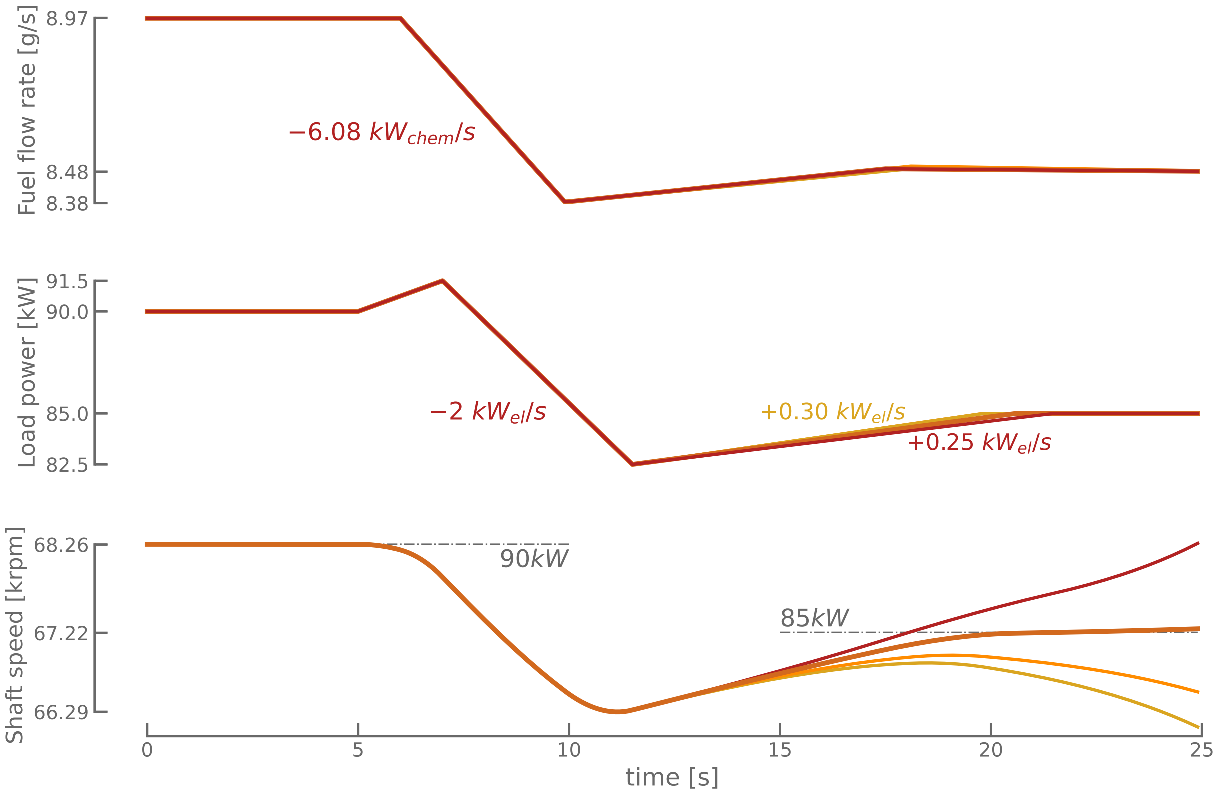

Figure 5.18: Control variables and shaft speed response during the transient maneuver from $90kW$ to $85kW$. The different curves represent the mGT response with the different control settings.

As it is illustrated, the obtaining of a stable response is conditioned by the controller tuning. For clarity, the details on the fuel control settings are reported in the figure (i.e. imperceptible differences). The stable response was obtained for a positive power rate of $+0.275kW_{el}/s$, which was determined after trials and errors.

The other quantities corresponding to these transients are reported in Fig. 5.19. Except for the TIT, all of them show a similar behavior as observed experimentally, as depicted in Fig. 5.20. All the simulated variables show a smaller characteristic time than the experiments, except for the TOT which is excessively smoothen by an over-sizing of the turbine casing heat capacity. On the other hand, the shaft dynamics is very well captured.

The discontinuities in TIT were expected and are attributed to the suppression of the energy conservation on the combustor casing (i.e. decision made because of the induced instabilities).

Additional results related to the mass accumulation in the combustion chamber are provided in Appendix E.

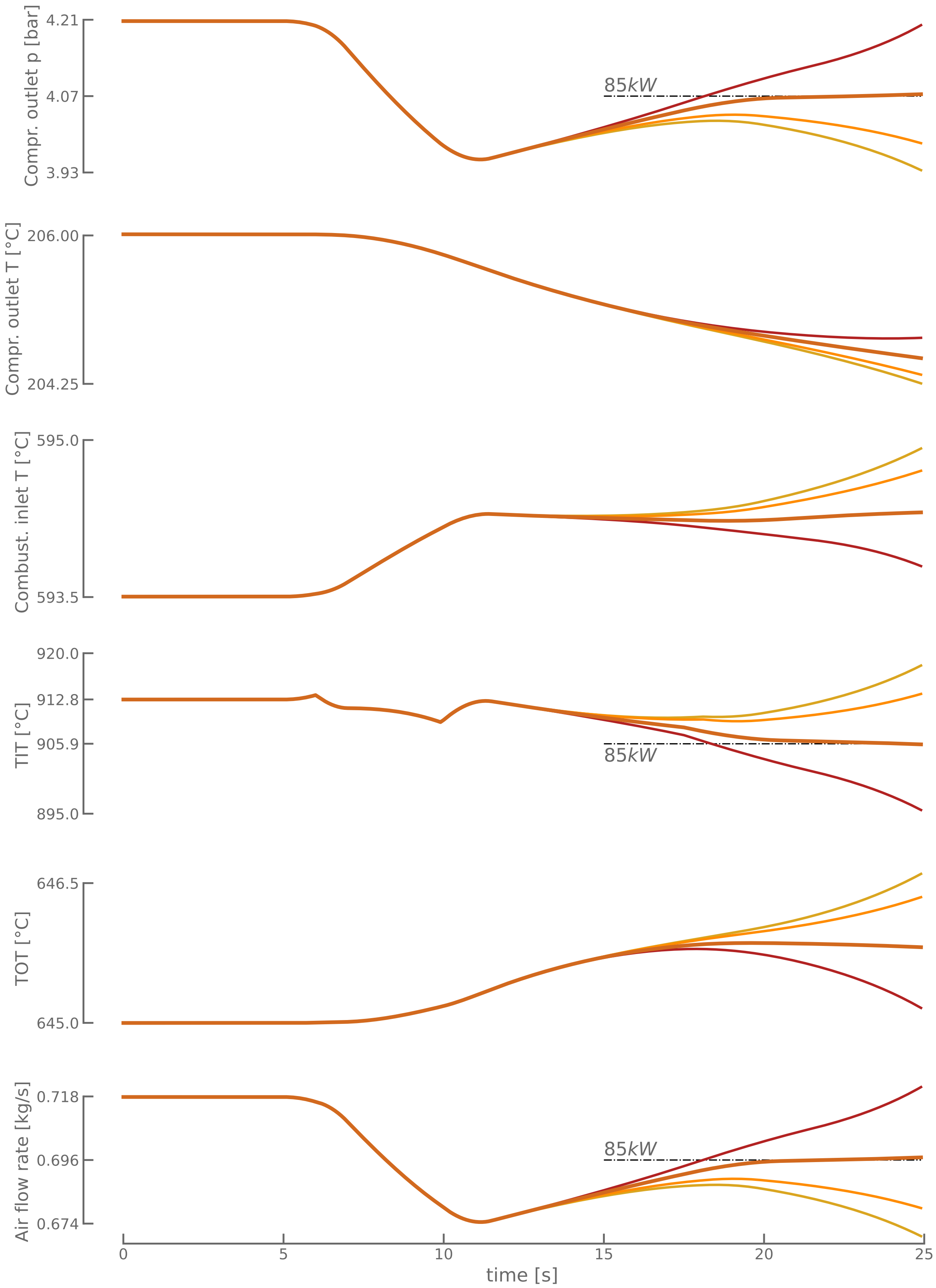

Figure 5.19: Additional results during the transient maneuver from $90kW$ to $85kW$. The different curves represent the mGT response with the different control settings.

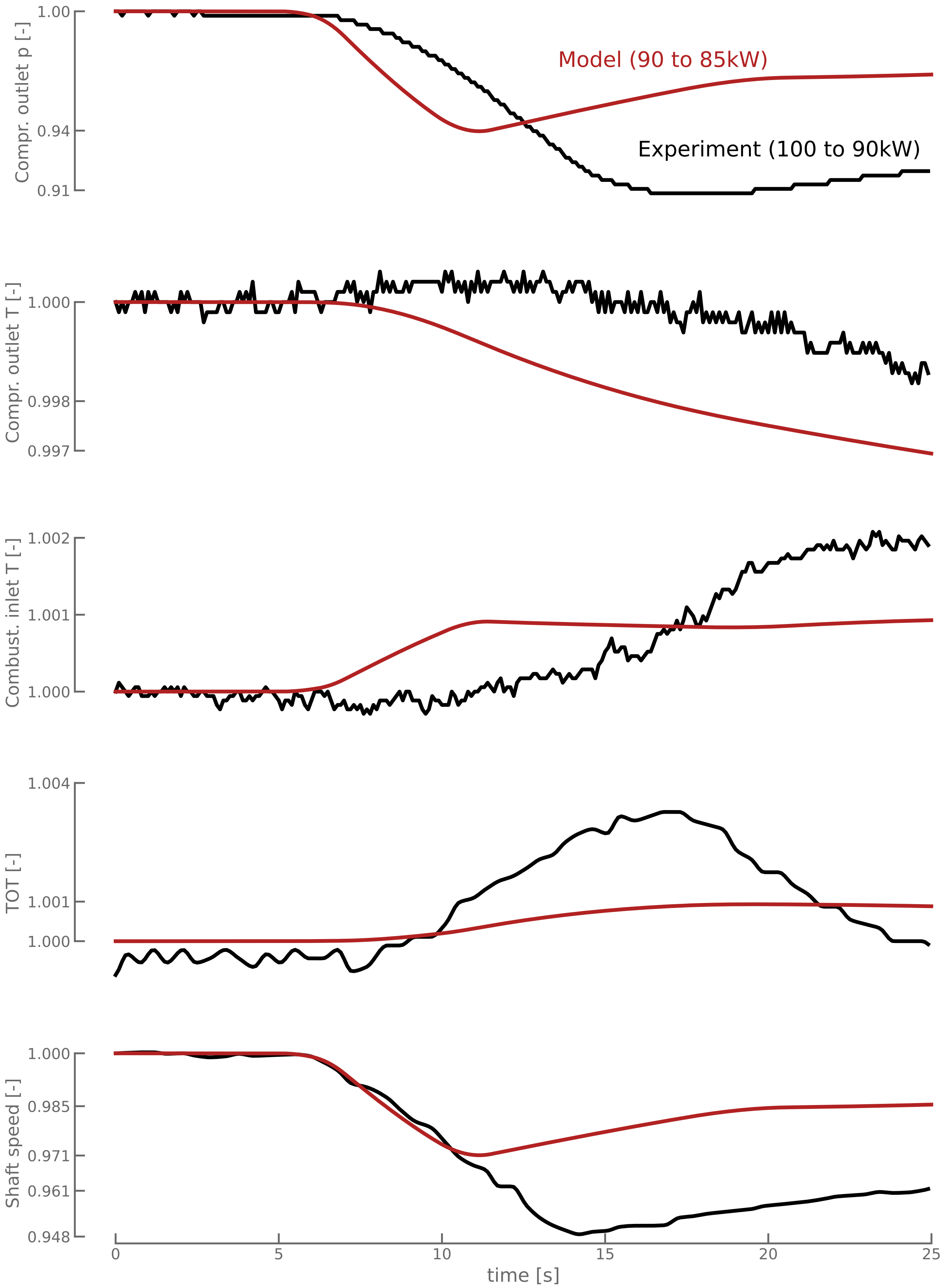

Figure 5.20: Comparison of the transient behaviors: experimental data from $100kW$ to $90kW$ and simulated data from $90kW$ to $85kW$. Normalization with initial conditions. The experimental transient was selected because this is the most similar to the simulated one. The simulation results show smaller characteristic times, except for the TOT.

5.4 Summary of model assets and shortcomings

This Section summarizes, with a bullet points structure to ease the reading, the model assets and shortcomings, and addresses the potential future improvements it could be subjected to.

Performance maps model

- *Assets*:
  - Representation of transients on the maps (rarely encountered in the literature);
  - Highlighted part load inaccuracies of the original maps compared to the actual performances with surge margin analyses.
- *Shortcomings*:
  - Important complexity induced by the solution computation for the ellipses.
- *Future improvements*:
  - Recommend installation of air flow meter in the test rig and use scaling and shifting techniques (see Section 2.2) coupled with experimental results to correct the maps;
  - Use alternatives to ellipses to express the maps (i.e. β lines, ...).

Compressor and turbine models

- *Assets*:
  - Simple model for energy conservation in the casing and showing acceptable results.
- *Shortcomings*:
  - Solution non-uniqueness for air flow rate with the compressor map (see Fig. 5.21);
  - Misevalution of the outlet temperatures because heat capacity ratio defined with inlet conditions only;
  - Misevalutation of the initial delay in temperature outlet response.
- *Future improvements*:
  - Use air flow rate as an input instead of compression ratio to get rid of solution non-uniqueness;
  - Use outlet conditions from previous time-step to compute the average heat capacity ratio;
  - Improve heat transfer model between outlet flow and casing for better evaluation of temperature response;
  - Reduce turbine casing heat capacity for better fit with experiments.

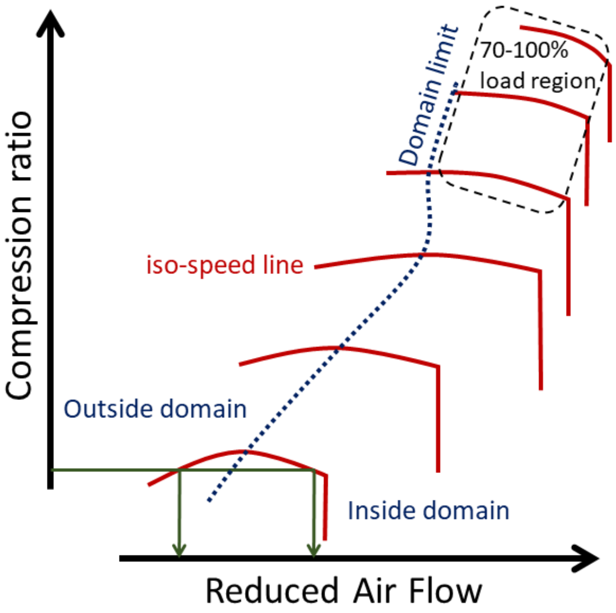

Figure 5.21: Illustration of solution non-uniqueness issue.

Combustor model

- *Assets*:
  - Simple combustion model (one step reaction).
- *Shortcomings*:
  - Induced instabilities with energy conservation on casing;
  - Issue with the thermodynamic model when performing the energy balance and causing excess fuel consumption.
- *Future improvements*:
  - Simplify the control volume energy conservation equation and use T_3 as state variables to reduce the complexity;
  - Use the flue gas heat capacity from the previous time step to get rid of the iterative computation.

Recuperator model

- *Assets*:
  - Low complexity and extremely accurate transient results (only three differential equations while often ten in the literature);
- *Shortcomings*:
  - Wrong evaluation of hot leg outlet temperature.
- *Future improvements*:
  - Use different heat transfer coefficients in each side;
  - Account for longitudinal heat conduction in matrix.

Control system

- *Assets*:
  - Successful implementation in `Python`
- *Shortcomings*:
  - Not correctly tuned yet.
- *Future improvements*:
  - Update reference tables to new system and tune the gains.

Global model and simulation tool

- *Assets*:
    - Effective static and dynamic individual validation of most blocks;
    - Shaft dynamics very well captured;
    - Can be used to model other cycles (*modular problem formulation*);
    - Can be used to test control strategies.
- *Shortcomings*:
    - Excessive computation to simulated time ratio.
    - Main issues for complete validation: (1) inaccuracy of original compressor maps compared to actual performances and (2) excessive fuel consumption due to problem in energy balance around combustor.
- *Future improvements*:
    - Implement memory blocks to reuse values from previous time step and relax complexity;
    - Implement humid air treatment;
    - Work on numerical aspects to find faster solvers;
    - Improve part load calibration (need more experimental results).

CONCLUSION AND PERSPECTIVES

The primary goal of this Thesis was to develop, calibrate and validate a modular and flexible dynamic simulation tool, to perform transient analyses on micro gas turbines systems, with potential applications in alternative and hybrid cycles.

A non-linear grey-box model has been constructed for that aim and, contrary to the `Simulink` models generally proposed in the literature, this one has been successfully implemented in the `Python` open-source programming language. A library of blocks, representing all the conventional mGT components, and which can be easily assembled to form a global model, has been set up to fulfil the modularity requirement and to allow for simulation of novel cycles.

Each block was calibrated to represent the Turbec T100, based on both experimental measurements issued from the VUB test rig and data published in the literature, in order to validate the simulator.

A performance map model for the turbomachinery components, resulting from an in-depth literature review, was constructed in Chapter 2 to fit the original manufacturer maps with elliptical, polynomial and exponential curves, and with hybridization procedures. It shows an extremely high fidelity to the original maps, especially for the turbine reduced flow rate, with an average relative deviation below 0.02% in the typical operating range.

The developed physical and thermodynamic model has been thoroughly discussed for each block in Chapter 3. Among them, a very low complexity and effective model for the recuperator has been introduced, and shows perfect matches with experimental results. A precise model identifying six different contributions to the shaft dynamics has also been established. A first attempt of control system implementation was finally achieved, despite still requiring a fine tuning to obtain stable step responses.

The compressor, recuperator, turbine and shaft blocks were validated against experimental results monitored during constant power demand and transient operations. Full load simulated static results showed an excellent agreement with the experiments.

The relatively more important error on the part load results, essentially due to speed deviations, was attributed to the missevalution of the actual turbomachinery performances by the original performance maps, probably due to time degradation. These conclusions were backed by surge margin analyses, showing inconsistencies with the compressor map model, and by the high fidelity of the model to the original maps.

Moreover, the average relative error on the part load static results was always inferior to 1%, except for the fuel consumption and exhaust gas temperature. The excessive fuel consumption is due to an issue in the thermodynamic model when performing the energy balance on the combustion chamber, and could not be fixed up to now. The reason for missevalution of the exhaust gas temperature was attributed to the assumption that the heat transfer coefficient is the same on both recuperator sides.

The simulated system showed a high sensitivity to disturbances with unstable step responses. No solid conclusion was drawn about the physical consistency of this observation, as the complexity involved by the model could also results in instabilities. Simplifications of the conservation equation around the combustor could allow for the assessment of physical consistency of this observation.

However, pseudo controlled transient maneuvers showed that the system could be regulated between two operating points. With these maneuvers, the simulated dynamic behavior could be qualitatively validated against experimental data.

The numerical performances of the simulator were relatively poor compared to other models, with a computation to simulated time ratio usually ranging between 20 and 40. Nevertheless, routes were suggested to overcome this limitation regarding real-time simulations, such as the implementation of memory blocks.

The information reported in this Thesis intends to serve a baseline for future works. From the conclusions drawn throughout this document, it turns out that critical focus should be put on fixing the issue with the energy balance on the combustor, causing an excess fuel consumption, as discussed in Section 5.2.2.

Also, a correction of the compressor map with scaling and shifting methods, and based on test bench measurements of the air flow rate, should allow for more accurate simulation results.

The recuperator model developed in this work, which has been identified as this simulation tool main asset, should systematically be considered when constructing dynamic models for mGTs.

To the aim of studying the dynamics of mGT systems with this numerical tool, the main challenge lays in the establishment and the fine tuning of control strategies to obtain stable step responses.

Appendices

APPENDIX A

ADDITIONAL INFORMATION ABOUT THE T100

Frequently encountered research teams

Some of the research teams frequently encountered in literature during this work and utilizing the T100 are non-exhaustively listed below, and their contribution is briefly introduced:

- **TPG-DiMSET**, *Thermochemical Power Group, Dipartimento di Macchine, Sistemi Energetici e Trasporti, Università di Genova, Genova, Italy.*

  In 2005, A. Traverso proposed `TRANSEO`, a simulation environment for the assessment of dynamic performances of mGTs [21] (initially applied to a Bownman TG-45). With other authors, he then worked on transient models for externally fired mGTs and on Closed Brayton Cycles for solar applications (both based on a Elliott TA-80R) [15, 16]. Starting from 2010, Ferrari et *al.* published experimental analyses on the dynamic performances of the T100 recuperator [37, 87];

- **DLR**, *Institute of Combustion Technology, German Aerospace Centre, Stuttgart, Germany.*

  In 2010, M. Hohloch et *al.* published steady state and transient experimental results obtained with the T100 [83]. The next year, Zanger et *al.* proposed experimental investigations of pressure losses on the performance of the T100 [93]. In 2015, Zornek et *al.* constructed and validated a combustor prototype for the use of low calorific fuels [25]. More recently, Henke et *al.* introduced and validated static and dynamic models for the T100 [5, 6];

- **CNR**, *Istituto Motori, Napoli, Italy.*

  In 2015, Calabria et *al.* proposed CFD analyses of the T100 combustor at part load and by varying fuels [29], as well as with liquid fuels [4]. In 2017, di Gaeta et *al.* proposed a dynamic model for the T100 fed by natural gas and hydrogen blends [12];

- **DIISM**, *Dipartimento di Ingegneria Industriale e Scienze Matematiche, Universita Politecnica delle Marche, Ancona, Italy.*

  Caresana et *al.* studied in 2014 the effects of ambient temperature on the global performances of a T100 mGT-CHP unit [3]. The next year, Comodi et *al.* proposed strategies to enhance mGTs performance in hot climates [10] and in hybrid systems with PV [30];

- **VUB**, *Department of Mechanical Engineering, Vrije Universiteit Brussel, Brussels, Belgium.*

> For more than 10 years now [58], VUB has developed a strong expertise in micro humid air turbines. Several Master Theses [28, 91] and PhD Theses [11] were conducted in the field of mHATs and alternative cycles. First researches in this domain started around 2008 [58]. Moreover, their experimental test rig permitted the validation of the developed models, with the first experimental results published in 2012 [59].

Let us finally mention M. Renzi, from *Libera Università di Bolzano*, who is a frequent co-author of the above listed research teams.

APPENDIX B

FITTING COEFFICIENTS OF THE PERFORMANCE MAPS

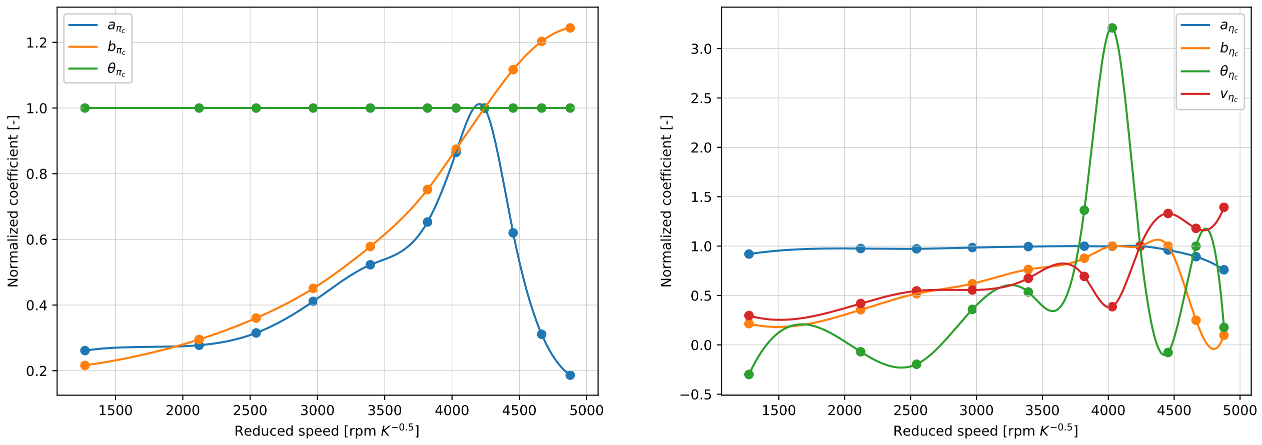

(a) Compressor mass flow

(b) Compressor efficiency

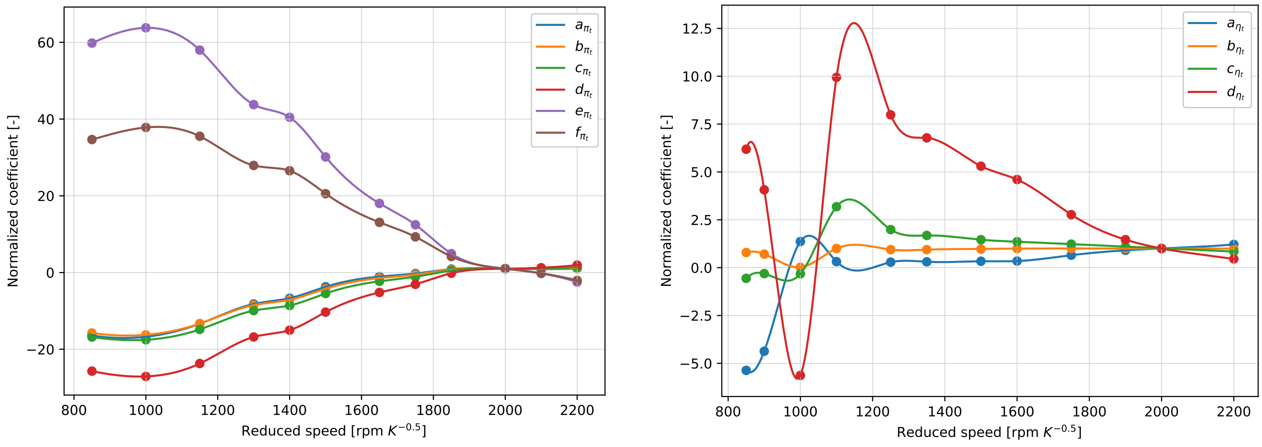

(c) Turbine mass flow

(d) Turbine efficiency

Figure B.1: Coefficients used for the expression of performance maps. The normalization was made w.r.t the full load operating speed of the T100.

APPENDIX C

DERIVATION OF THE CONSERVATION EQUATIONS

The control volume model for conservation equations

The control volume approach is typically used for the establishment of dynamic models for open systems where the mass and energy flows are the variables of interest. This method is intended to correlate the mass and internal energy trapped inside a so called *control volume* with the mass and energy flows crossing the boundary of the latter. Figure C.1 illustrates this approach. Applied to the control volume, the mass and internal energy conservation equations are expressed as

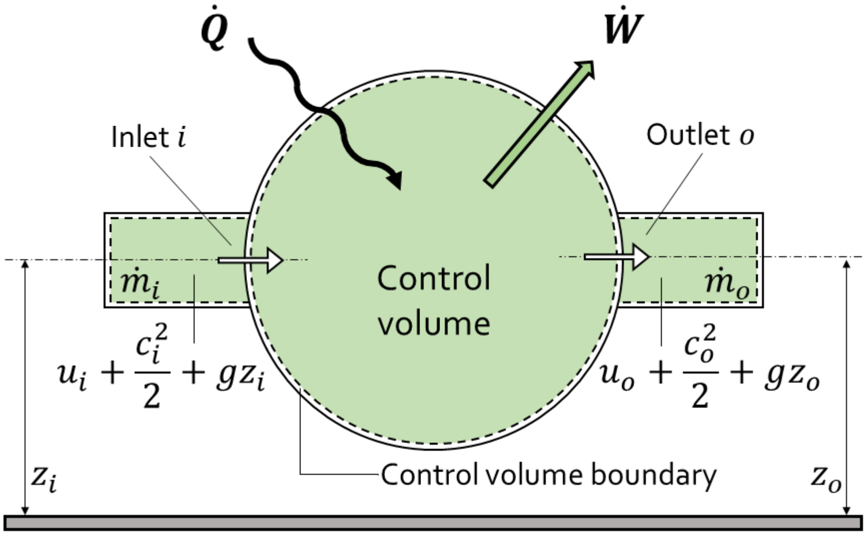

Figure C.1: Graphical illustration of the control volume model used in thermodynamic systems.

$$\frac{dm_{cv}}{dt} = \dot{m}_i - \dot{m}_o \, , \tag{C.1}$$

$$\frac{dU_{cv}}{dt} = \dot{m}_i\Big(u_i + \frac{c_i^2}{2} + gz_i\Big) - \dot{m}_o\Big(u_o + \frac{c_o^2}{2} + gz_o\Big) + \dot{Q} - \dot{W} \, , \tag{C.2}$$

where m_{cv} and U_{cv} are the mass and internal energy trapped inside the control volume. In this model, the energy conservation builds upon the variation of internal (u), kinetic (c^2) and gravitational (gz) specific energies (i.e. J/kg) contained into the flow between the inlet and outlet sections of the volume, as well as the heat and work flows exchanged by the volume with the outside.

It has to be stressed that the work term used in Eq. (C.2) includes both the work of the flow across the boundary (e.g. the work provided to the shaft in expansion machines) and all other forms of it. For this reason, it is convenient to introduce the concept of flow work.

Concept of flow work

Whenever a mass flow crosses a control volume, a force pushes the mass located at the inlet (m_i) and outlet (m_o) sections into and out of the volume respectively. Figure C.2 illustrates this.

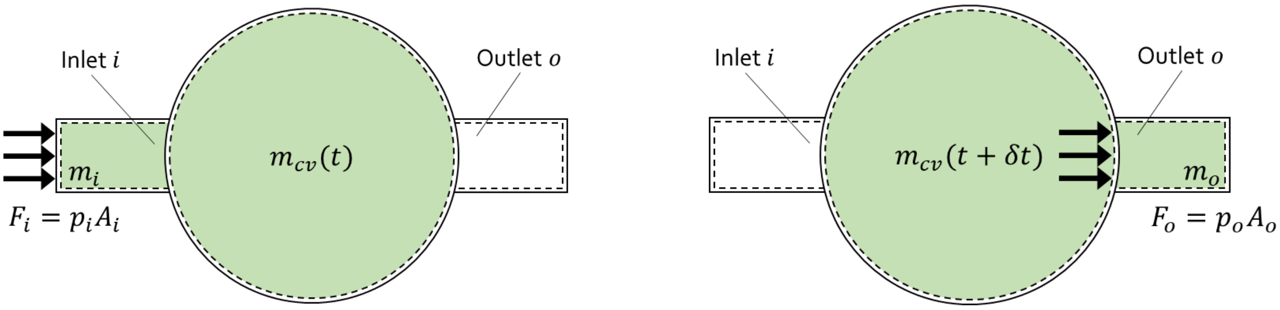

(a) Push m_i into the control volume.

(b) Push m_o out of the control volume.

Figure C.2: Graphical illustration of the concept of flow work applied to a control volume.

Because the masses m_i and m_o undergo a displacement due to the forces, a work is done on the system at its inlet and by the system at its outlet. The work rate at the inlet and outlet sections can be defined as

$$\frac{\delta W}{\delta t} = \dot{W} = F\frac{dx}{dt} = Fc = (pA)c \, , \tag{C.3}$$

with c the flow speed, p the pressure and A the section area. Formulating the mass flow rate as

$$\dot{m} = \rho A c = \frac{Ac}{v} \, , \tag{C.4}$$

the work therm of Eq. (C.2) can be reformulated as

$$\dot{W} = \dot{W}_{cv} + p_o A_o c_o - p_i A_i c_i = \dot{W}_{cv} + \dot{m}_o p_o v_o - \dot{m}_i p_i v_i \, , \tag{C.5}$$

with $\dot{W}_{cv}$ the work flow across the boundary of the control volume and $\dot{m}pv$ the flow work rate at the inlet and outlet sections.

Enthalpy form of energy conservation

Thanks to the reformulation of the work flow in Eq. (C.5), it can be shown that the energy conservation can be expressed with the specific enthalpy instead of specific internal energy. Indeed, recalling the definition of the specific enthalpy,

$$h = u + pv \, , \tag{C.6}$$

with v the specific volume (i.e. m^3/kg), the internal energy conservation,

$$\frac{dU_{cv}}{dt} = \dot{m}_i\Big(u_i + \frac{c_i^2}{2} + gz_i\Big) - \dot{m}_o\Big(u_o + \frac{c_o^2}{2} + gz_o\Big) + \dot{Q} - \dot{W}_{cv} - \dot{m}_o p_o v_o + \dot{m}_i p_i v_i \, , \tag{C.7}$$

can be rewritten as

$$\frac{dU_{cv}}{dt} = \dot{m}_i\left(h_i + \frac{c_i^2}{2} + gz_i\right) - \dot{m}_o\left(h_o + \frac{c_o^2}{2} + gz_o\right) + \dot{Q} - \dot{W}_{cv} \tag{C.8}$$

The benefit of this formulation is to consider only the work flow through the control volume boundary (i.e. work done by or on the system) and to ignore the inlet and outlet pressures and specific volumes.

Generic form of conservation equations

The equations developed in the previous section usually undergo some simplifications to make them more suitable for off-design models. They are also generally written in intensive variables form.

Usual simplifications

Some simplifications usually apply to the energy conservation equation. Whereas the motivation for these simplifications is that some terms are negligible regarding the others, it is often an asset to express the energy conservation with thermodynamics quantities only. Indeed, when developing off-design models (e.g. for micro gas turbine systems), the variations of kinetic and gravitational specific energies can be difficult to model with few accurate information available on the system geometry.

Thus, in this work, we will assume that the variations in kinetic and gravitational energies are negligible. This can be supported by magnitude order considerations. Looking at the gravity, one observes that a $1m$ elevation variation would cause a 100 times smaller change in specific energy than a $1K$ variation in gas temperature. Looking at the flow speed, it can also be noted that a $10m/s$ variation would cause a 20 times smaller change in specific energy than $1K$ variation.

Consequently, the simplified following equation will be used in this work. It used in many dynamic models for mGTs [5, 18, 49, 51].

$$\frac{dU_{cv}}{dt} = \dot{m}_i h_i - \dot{m}_o h_o + \dot{Q} - \dot{W}_{cv} \tag{C.9}$$

Use of volumetric mass density

When modelling open systems with gaseous media, it is often more convenient to use the density as a variable instead of the mass. Indeed, the density can be used as a flow variable (e.g. likewise the pressure and the temperature) whereas the use of the mass is intrinsically connected to the notion of volume (i.e. as suggested by the ideal gas law).

For this reason, the mass and energy conservation equations are rewritten as functions of the density. If the control volume satisfies

$$\frac{dV}{dt} = 0\,, \tag{C.10}$$

the conservation equations are written as

$$V_{cv}\frac{d\rho_{cv}}{dt} = \dot{m}_i - \dot{m}_o\,, \tag{C.11}$$

$$V_{cv}\frac{d(\rho_{cv}u_{cv})}{dt} = \dot{m}_i h_i - \dot{m}_o h_o + \dot{Q} - \dot{W} \tag{C.12}$$

Because the motivation for using the conservation equations with the control volumes is to model both mass and energy accumulation, as well as deriving the outlet conditions based on the inlet variables, the internal energy of the control volume can be used as a variable intended to ensure the model continuity. This approach is equivalent to assuming that the outlet conditions are equal to that of inside the control volume. This simplification was also made by [18, 49, 51].

Although the energy conservation equation could be based on the temperature instead of specific energy, deriving such formulation is a rather intricate task, considering the dependency of the heat capacity on the temperature. Indeed, an exact development, as follows,

$$\frac{d(\rho u)}{dt} = \frac{d\rho}{dt}u + \rho\frac{du}{dt} = \frac{d\rho}{dt}c_vT + \rho\frac{d(c_vT)}{dt} = \frac{d\rho}{dt}c_vT + \rho\left(\frac{dc_v}{dt}T + c_v\frac{dT}{dt}\right), \tag{C.13}$$

leads to a relatively complex expression. More precisely, the complexity lies in the evaluation of the time derivative of the specific heat capacity at constant volume. Whereas some authors decided to neglect this term [18, 49], it is here decided to base the energy balance on the specific energy, in order to ensure energy conservation. This choice was also made by [5, 51]. Nevertheless, Eq. (C.12) can be further developed in order to isolate the internal energy term. Integrating the previous consideration about the model continuity (i.e. outlet conditions equal to inside conditions), one obtains the following equations:

$$\frac{d\rho_o}{dt} = \frac{\dot{m}_i - \dot{m}_o}{V_{cv}}, \tag{C.14}$$

$$\frac{du_o}{dt} = \frac{\dot{m}_ih_i - \dot{m}_oh_o + \dot{Q} - \dot{W} - u_o(\dot{m}_i - \dot{m}_o)}{\rho_oV_{cv}} \tag{C.15}$$

Finally, the intensive variables being that of interest when modelling systems, the pressure and temperature can be derived from the ideal gas law and from the definition of the specific internal energy (e.g. extracted from a thermodynamic database). The non-linear system of equations to be solved when extracting p_0 and T_0 from ρ_0 and u_0 is given by:

$$\begin{cases} p_o - \rho_oRT_o & = 0 \\ u_o - u_{database}(p_o, T_o) & = 0 \end{cases} \tag{C.16}$$

APPENDIX D

BLOCK DIAGRAM OF THE GLOBAL MGT MODEL

This page is intentionally left blank.

Please see next page (large figure).

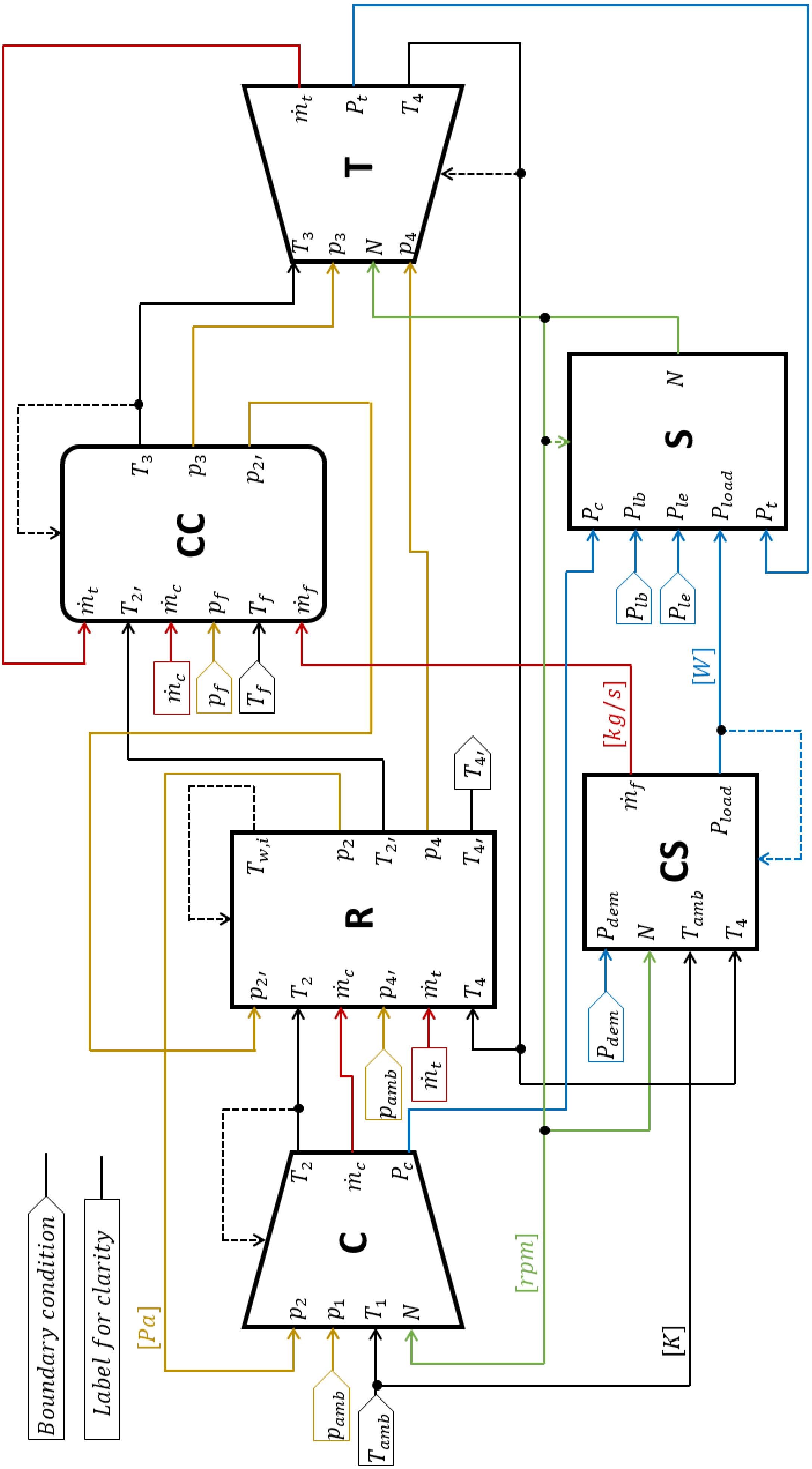
T
$\dot{m}_t$
P_t
T_4
T_3
p_3
N
p_4
CC
T_3
p_3
$p_{2'}$
$\dot{m}_t$
$T_{2'}$
$\dot{m}_c$
p_f
T_f
$\dot{m}_f$
$\dot{m}_c$
p_f
T_f
S
N
P_c
P_{lb}
P_{le}
P_{load}
P_t
P_{lb}
P_{le}
$[W]$
$[kg/s]$
CS
$\dot{m}_f$
P_{load}
P_{dem}
N
T_{amb}
T_4
P_{dem}
R
$T_{w,i}$
p_2
$T_{2'}$
p_4
$T_{4'}$
$T_{4'}$
$p_{2'}$
T_2
$\dot{m}_c$
$p_{4'}$
$\dot{m}_t$
T_4
p_{amb}
$\dot{m}_t$
C
T_2
$\dot{m}_c$
P_c
p_2
p_1
T_1
N
p_{amb}
T_{amb}
$[Pa]$
$[rpm]$
$[K]$
Boundary condition
Label for clarity

APPENDIX E

DETAILS FOR THE CALIBRATION AND SIMULATION RESULTS

Compressor casing mass

The dynamics of the compressor outlet temperature is tuned with the casing mass parameter. Based on the experimental shaft speed, compressor outlet pressure and inlet temperature, the model is capable of predicting the compressor outlet temperature. Figure E.1 illustrates the results obtained with the model for different casing masses, in comparison with the experimental values measured during four transient cases, where different load steps where applied. The

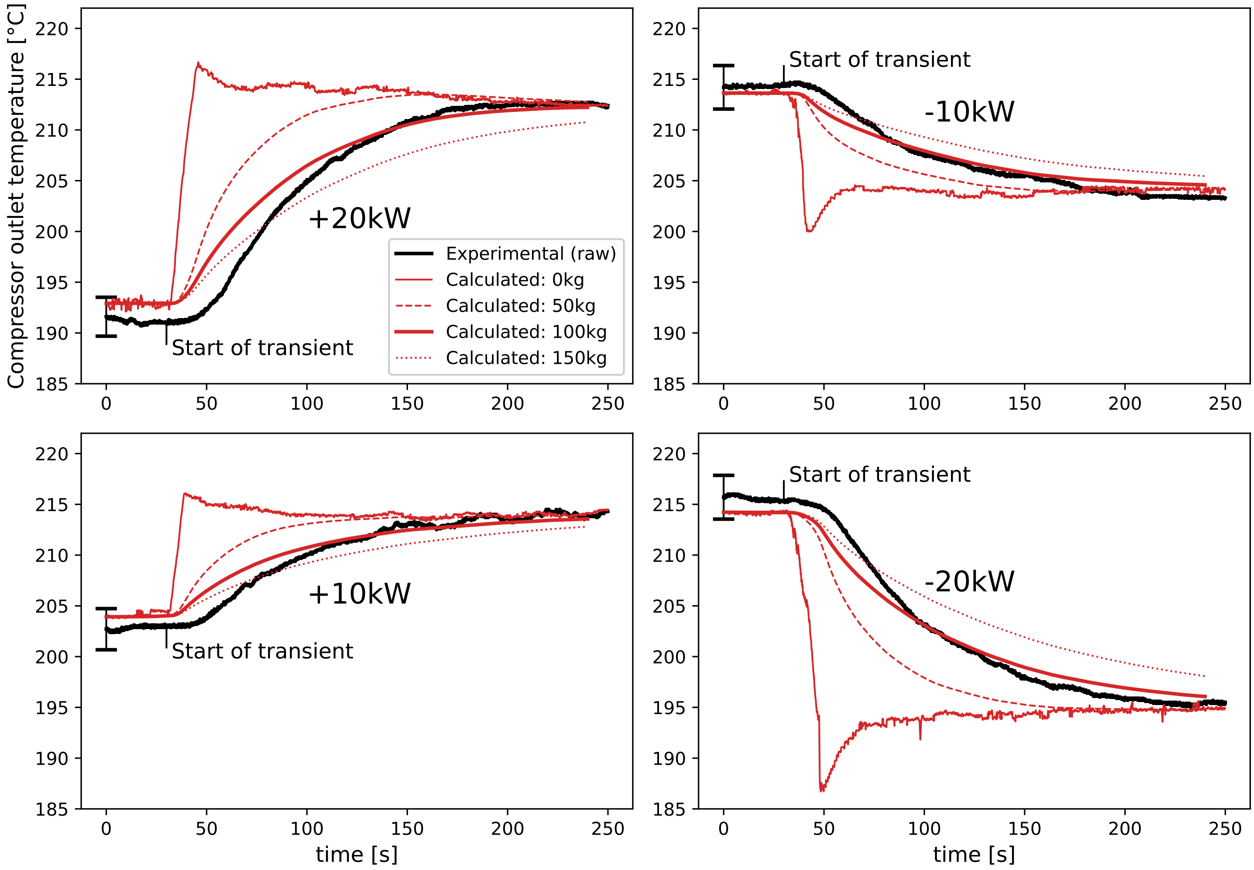

Figure E.1: Compressor outlet temperature (T_2) obtained for different casing masses.

case where $m_{cas,comp.} = 0kg$ corresponds to a quasi-steady state model. The results obtained in this context clearly indicate that the temperature dynamics at the compressor outlet has to be taken into account. For that aim, Fig. E.2 was constructed. It depicts the relative fitting errors obtained with different casing masses during the transients. The *max.* curve corresponds to the maximum relative error, while the *mean* curve is the average relative error. The root-mean-square error (*rms*), being the metric traditionally utilized for fitting purposes, is also reported.

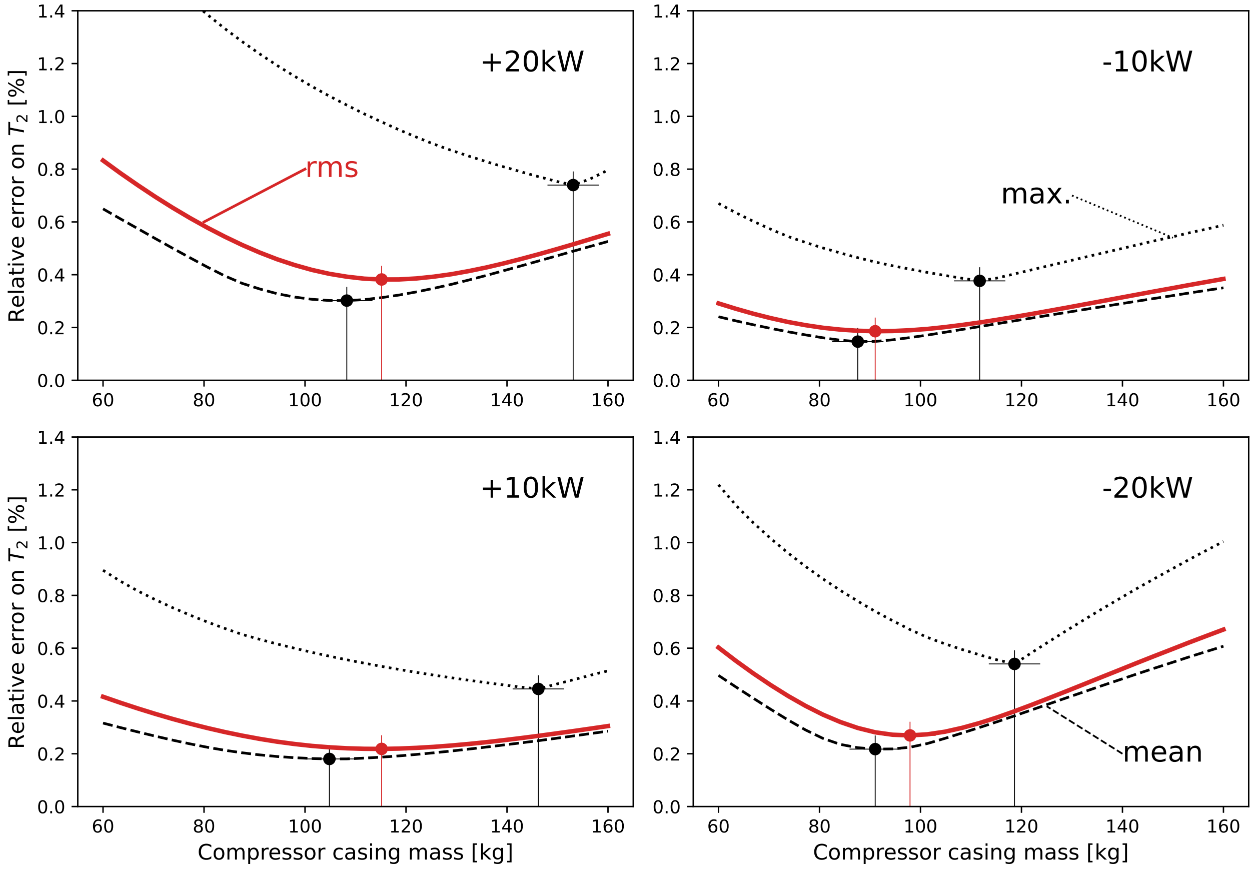

Figure E.2: Relative error on compressor outlet temperature (T_2) obtained for different casing masses. *Black dotted*: maximum error during transient. *Black dashed*: average error on the transient. *Red solid*: root-mean-square error of the transient.

It can be first noted that, for each of the four cases, a limitation of the maximum error involves the need of a higher mass than for a limitation of the mean error. It can also be observed that, for the cases with positive power steps (i.e. +10, $+20kW$), the mass minimizing the root-mean-square error is about $115kg$ in both cases. But for negative power steps of -10 and $-20kW$, the optimum masses are $91kg$ and $98kg$ respectively. Because this mass must be tuned with a constant value whatever the power step magnitudes, an averaged value of $105kg$ is selected.

The error observed on the compressor outlet temperature during the transients is reported in Fig. E.3. The maximum error observed in steady state is smaller than 2^oC, which is in the range of sensor accuracy. This can be attributed to a misevaluation of the isentropic efficiency and of the inlet temperature, but also indicates that the simplified compression model, introduced in Section 3.2, is valid in the T100 operating range.

The maximum error obtained with $105kg$ is 5^oC. This value could be further reduced by improving the dynamic model for T_2. Indeed, the assumption that the compressor outlet temperature is equal to a virtual casing temperature reaches its limit by non-modelling the delay in temperature response after the transient. This delay is particularly well visible for the $+20kW$ step. Therefore, a model accounting with more details for the conductive and convective heat transfer between the compressed air and the casing could be established.

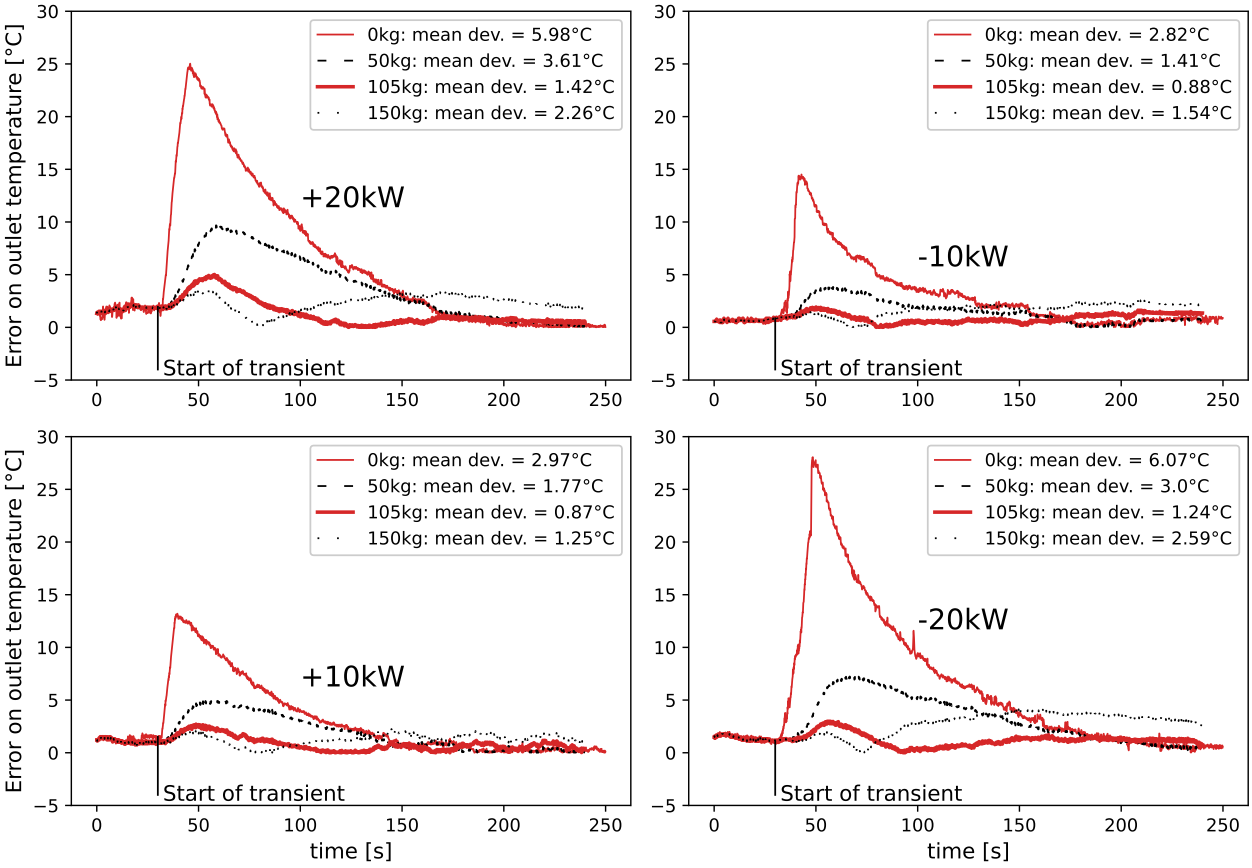

Figure E.3: Error on compressor outlet temperature (T_2) observed during the transients.

Recuperator calibration

Correlation for the UA value

The linear interpolation for the UA value is built with the following steady state points:

$$\begin{cases} UA & = (3741.5, 4303.5, 4595.0, 4940.0) \quad [W/K] \\ \dot{m}_c & = (0.4992, 0.5959, 0.6641, 0.7496) \quad [kg/s] \end{cases} \tag{E.1}$$

Matrix mass

The matrix mass (m_w) is calibrated with a similar methodology as for the compressor casing mass. Figure E.4 reports the different errors (i.e. max, mean, rms) obtained for different m_w. In contrast to the compressor, there is no clear optimum. In fact, the errors obtained for certain power steps are biased by the steady-state offset error (e.g. $+10kW$). Therefore, a value of $m_w = 185kg$ is selected to optimize in priority the fitting of the $+20kW$ step.

The obtained fitting errors during the four transients are reported in Fig. E.5.

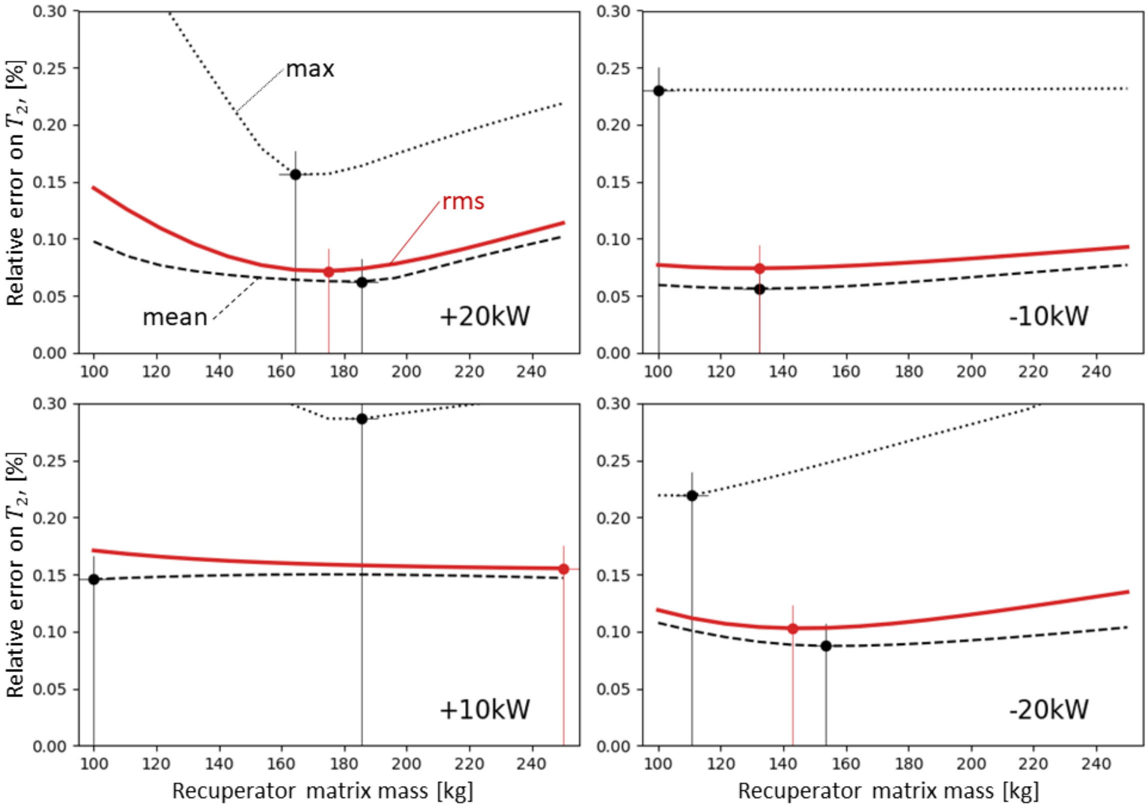

Figure E.4: Relative error on recuperator cold leg outlet temperature ($T_{2'}$) obtained for different casing masses. *Black dotted*: maximum error during transient. *Black dashed*: average error on the transient. *Red solid*: root-mean-square error of the transient.

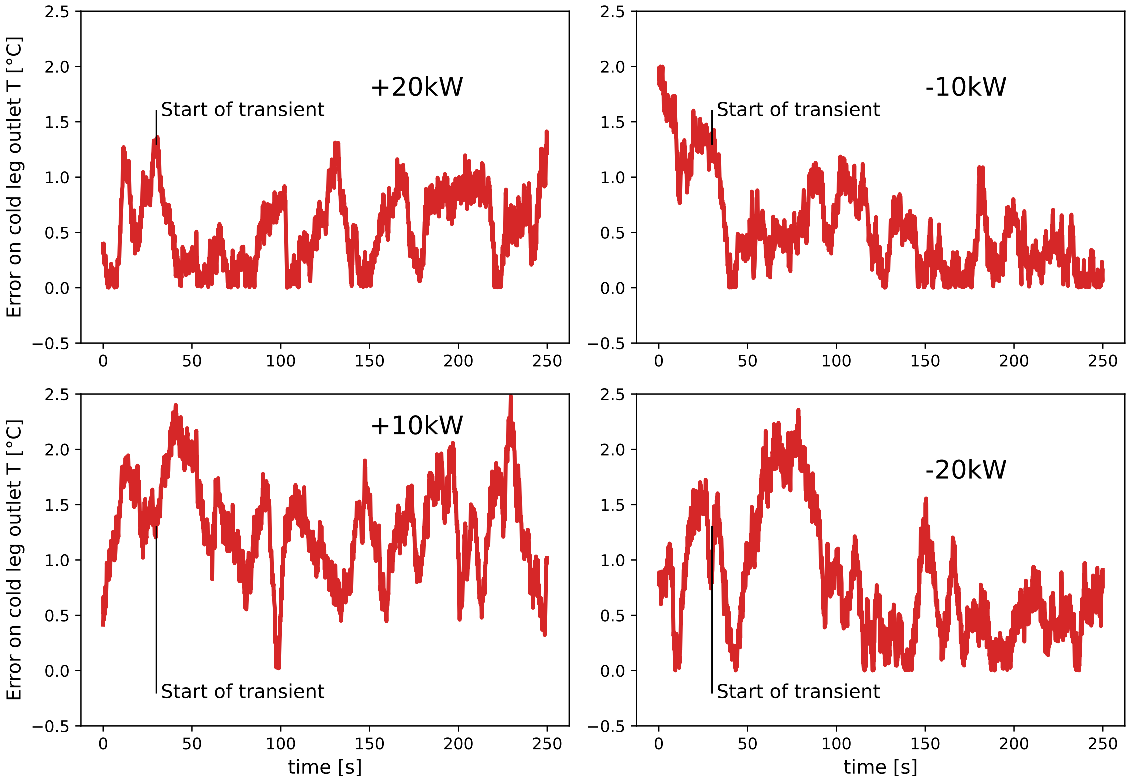

Figure E.5: Error on recuperator cold leg outlet temperature ($T_{2'}$) observed during the transients.

Combustion chamber volume

The impact of the combustor volume (V_{comb}) on the global mGT model have been evaluated. Different values of V_{comb} have been tested during two transient cases, where the load (P_{load}) and the fuel flow rate ($\dot{m}_f$) were changed. The obtained shaft speed responses are reported in Figs. E.6 & E.7.

It can be observed that the dynamic behaviour of the shaft speed is essentially the same for all V_{comb} (except for $V_{comb} = 500L$). The latter only slightly impacts the characteristic times.

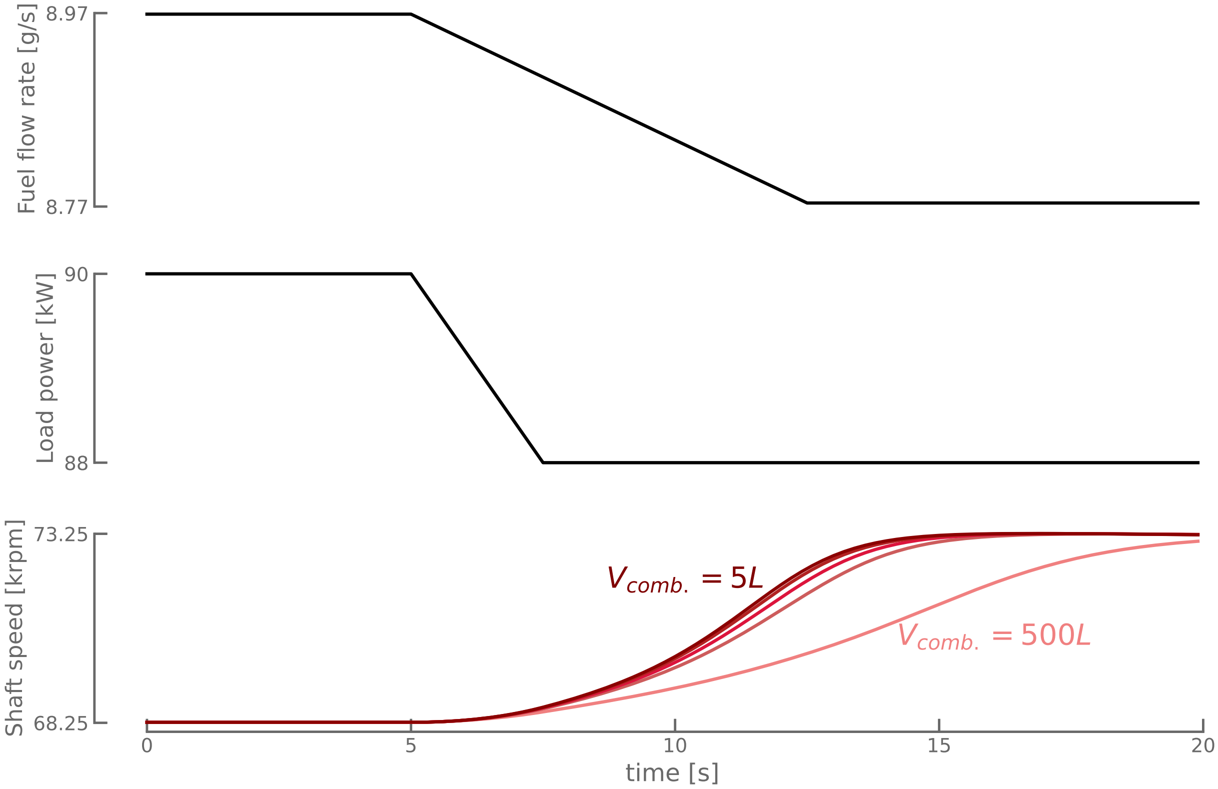

Figure E.6: Shaft speed response to transient in fuel and load power: acceleration. Combustor volume (V_{comb}), *pink* to *dark red*: $500L$, $100L$, $50L$, $20L$, $5L$.

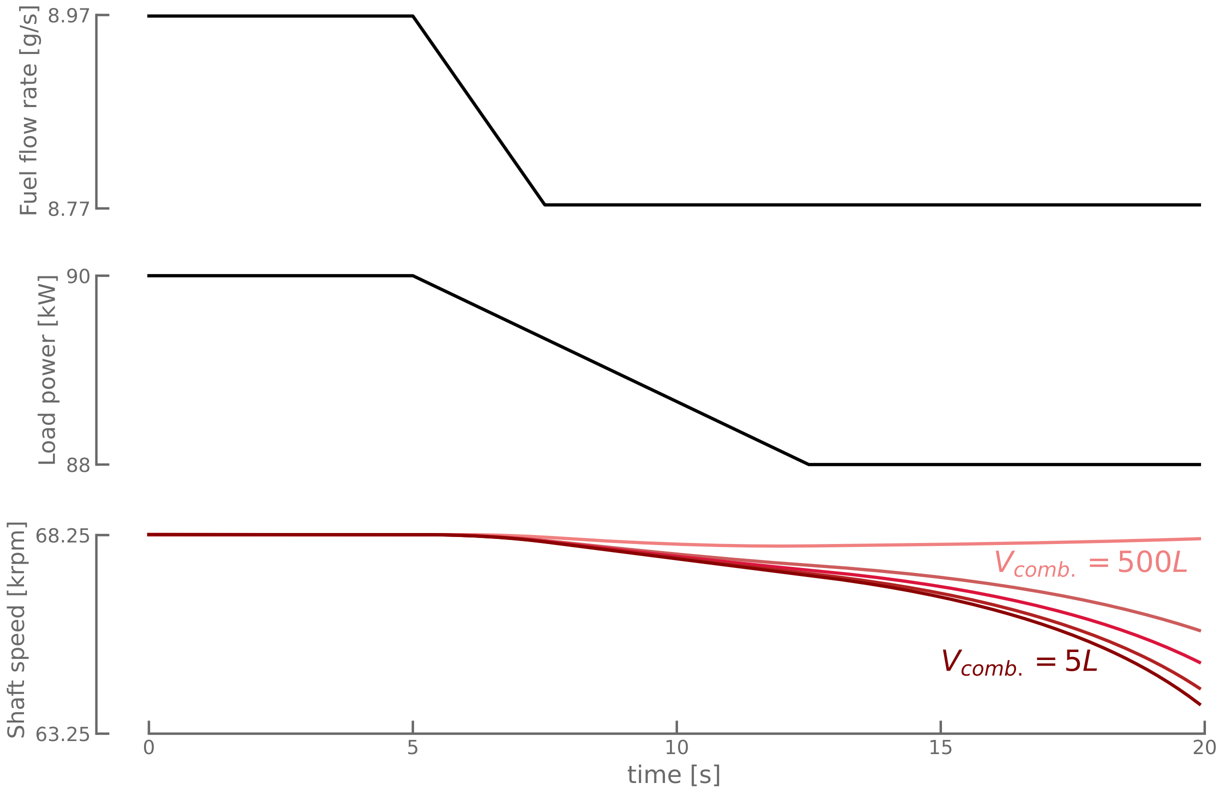

Figure E.7: Shaft speed response to transient in fuel and load power: deceleration. Combustor volume (V_{comb}), *pink* to *dark red*: $500L$, $100L$, $50L$, $20L$, $5L$.

Validation of the thermodynamic tables

The different tests made with the thermodynamic tables are reported in Fig. E.8.

- **Table 1**: thermodynamics tables provided in the thermodynamics class at EPL (LMECA1855 – Thermodynamique et énergétique)
- **Table 2**: derived from Engineering Equation Solver (EES) software developed by S. A. Klein and F. L. Alvarado. The routine used in calculations is the highly accurate Steam_IAPWS, which incorporates the 1995 Formulation for the Thermodynamic Properties of Ordinary Water Substance for General and Scientific Use, issued by The International Association for the Properties of Water and Steam (IAPWS). This formulation is based on the correlations of Saul and Wagner (J. Phys. Chem. Ref. Data, 16, 893, 1987) with modifications to adjust to the International Temperature Scale of 1990. The modifications are described by Wagner and Pruss (J. Phys. Chem. Ref. Data, 22, 783, 1993). The properties of ice are based on Hyland and Wexler, “Formulations for the Thermodynamic Properties of the Saturated Phases of H2O from 173.15 K to 473.15 K,” ASHRAE Trans., Part 2A, Paper 2793, 1983.
- **Table 3**: adapted from Kenneth Wark, Thermodynamics, 4th ed. (New York: McGraw-Hill, 1983), pp. 785–86, table A–5. Originally published in J. H. Keenan and J. Kaye, Gas Tables (New York: John Wiley & Sons, 1948).

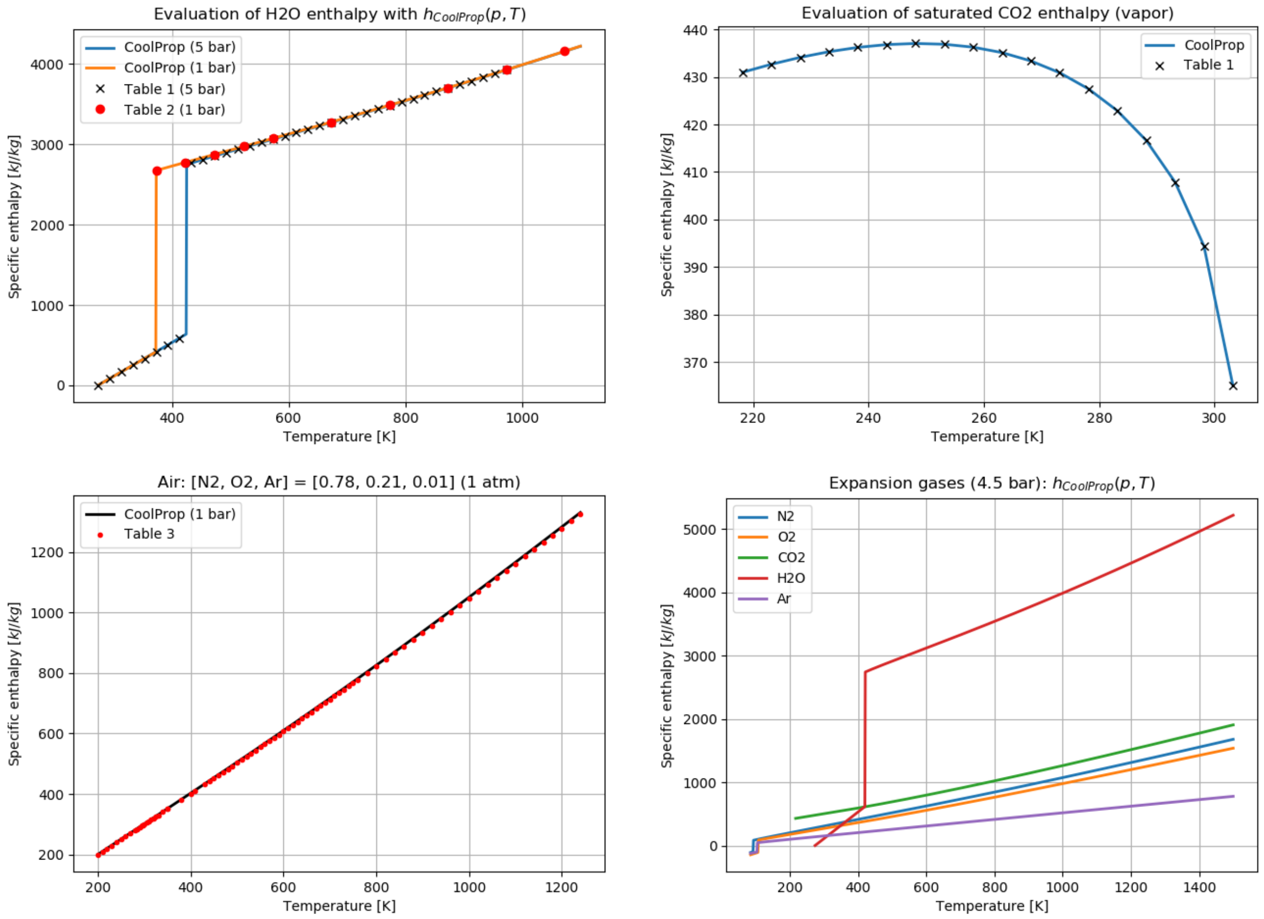

Figure E.8: Validation of the thermodynamic tables.

Additional static simulation results

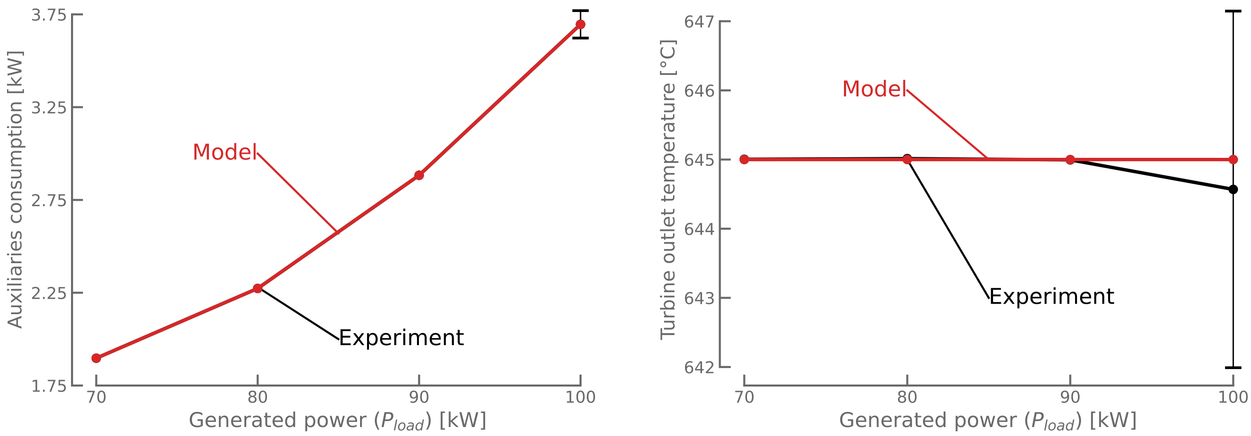

Figure E.9: Measured and simulated static results: additional results.

Additional dynamic simulation results

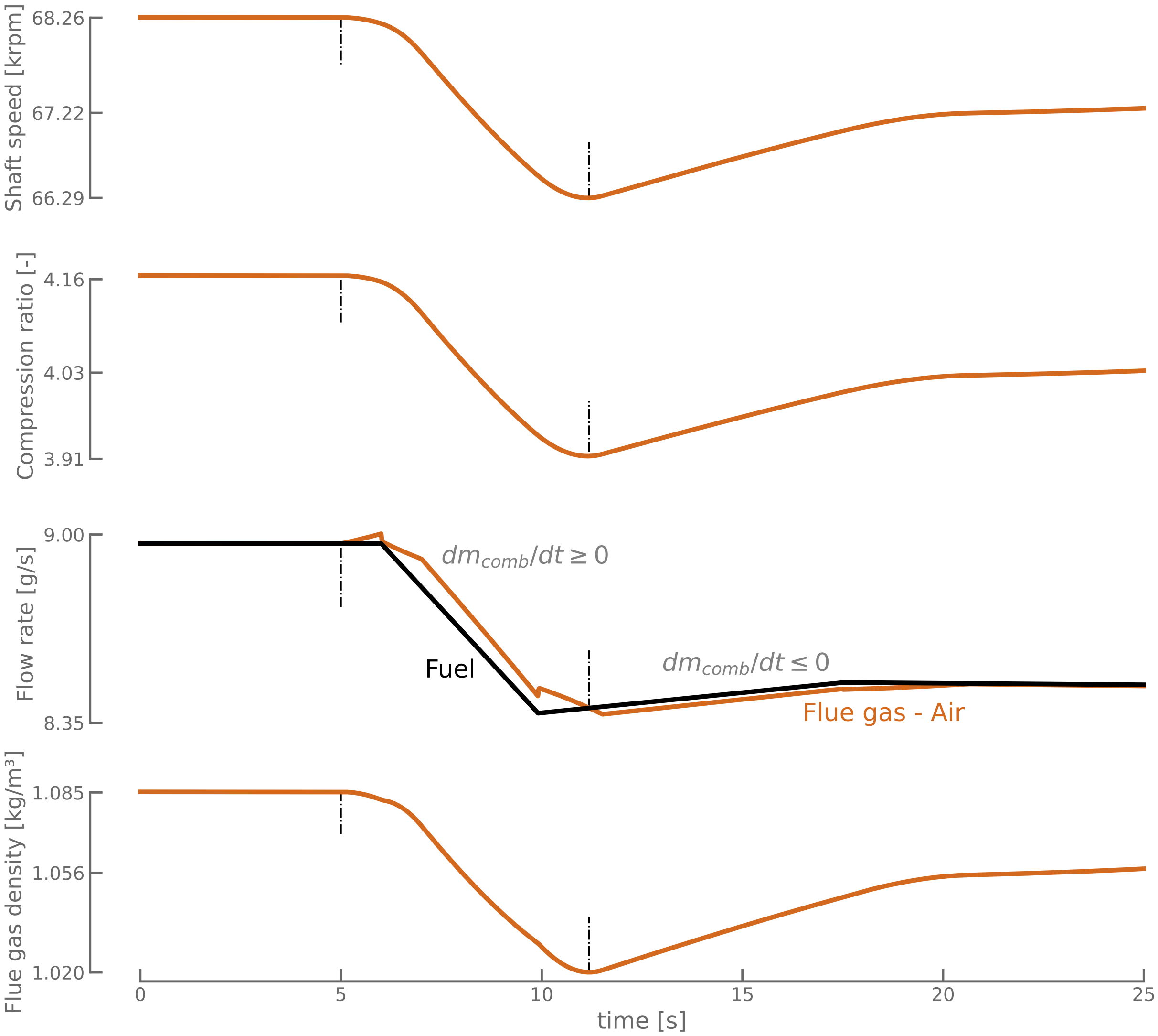

Figure E.10: Mass accumulation in the combustion chamber during the transient maneuver from $90kW$ to $85kW$ (time step for the simulation: $\Delta t = 5ms$).

BIBLIOGRAPHY

[1] W. De Paepe, M. Renzi, M. Montero Carrerro, C. Caligiuri, and F. Contino, "Micro Gas Turbine Cycle Humidification for Increased Flexibility: Numerical and Experimental Validation of Different Steam Injection Models," American Society of Mechanical Engineers Digital Collection, Aug. 2018.

[2] G. Xiao, T. Yang, H. Liu, D. Ni, M. L. Ferrari, M. Li, Z. Luo, K. Cen, and M. Ni, "Recuperators for micro gas turbines: A review," *Applied Energy*, vol. 197, pp. 83–99, July 2017.

[3] F. Caresana, L. Pelagalli, G. Comodi, and M. Renzi, "Microturbogas cogeneration systems for distributed generation: Effects of ambient temperature on global performance and components' behavior," *Applied Energy*, vol. 124, pp. 17–27, July 2014.

[4] R. Calabria, F. Chiariello, P. Massoli, and F. Reale, "Numerical Study of a Micro Gas Turbine Fed by Liquid Fuels: Potentialities and Critical Issues," *Energy Procedia*, vol. 81, pp. 1131–1142, Dec. 2015.

[5] M. Henke, T. Monz, and M. Aigner, "Introduction of a New Numerical Simulation Tool to Analyze Micro Gas Turbine Cycle Dynamics," *Journal of Engineering for Gas Turbines and Power*, vol. 139, p. 042601, Apr. 2017.

[6] M. Henke, N. Klempp, M. Hohloch, T. Monz, and M. Aigner, "Validation of a T100 Micro Gas Turbine Steady-State Simulation Tool," in *Volume 3: Coal, Biomass and Alternative Fuels; Cycle Innovations; Electric Power; Industrial and Cogeneration*, (Montreal, Quebec, Canada), p. V003T06A003, American Society of Mechanical Engineers, June 2015.

[7] B. F. Kolanowski, *Guide to microturbines.* Lilburn, GA : New York: Fairmont Press ; [Distributed by] Marcel Dekker, 2004.

[8] "Next mGT website." `https://nextmgt.com/about-project/`. Accessed: 2021-05-20.

[9] W. De Paepe, M. Montero Carrero, S. Bram, F. Contino, and A. Parente, "Waste heat recovery optimization in micro gas turbine applications using advanced humidified gas turbine cycle concepts," *Applied Energy*, vol. 207, pp. 218–229, Dec. 2017.

[10] G. Comodi, M. Renzi, F. Caresana, and L. Pelagalli, "Enhancing micro gas turbine performance in hot climates through inlet air cooling vapour compression technique," *Applied Energy*, vol. 147, pp. 40–48, June 2015.

[11] M. Montero Carrero, *Decoupling heat and electricity production from micro gas turbines: numerical, experimental and economic analysis of the micro humid air turbine cycle.* PhD thesis, Vrije Universiteit Brussel, Université Libre de Bruxelles, March 2018.

[12] A. di Gaeta, F. Reale, F. Chiariello, and P. Massoli, “A dynamic model of a 100 kW micro gas turbine fuelled with natural gas and hydrogen blends and its application in a hybrid energy grid,” *Energy*, vol. 129, pp. 299–320, June 2017.

[13] M. Montero Carrero, M. L. Ferrari, W. De Paepe, A. Parente, S. Bram, and F. Contino, “Transient Simulations of a T100 Micro Gas Turbine Converted Into a Micro Humid Air Turbine,” American Society of Mechanical Engineers Digital Collection, Aug. 2015.

[14] W. De Paepe, M. M. Carrero, S. Bram, A. Parente, and F. Contino, “Experimental Characterization of a T100 Micro Gas Turbine Converted to Full Humid Air Operation,” *Energy Procedia*, vol. 61, pp. 2083–2088, 2014.

[15] A. Traverso, A. F. Massardo, and R. Scarpellini, “Externally Fired micro-Gas Turbine: Modelling and experimental performance,” *Applied Thermal Engineering*, vol. 26, pp. 1935–1941, Nov. 2006.

[16] A. Traverso, F. Calzolari, and A. Massardo, “Transient Analysis of and Control System for Advanced Cycles Based on Micro Gas Turbine Technology,” *Journal of Engineering for Gas Turbines and Power*, vol. 127, pp. 340–347, Apr. 2005.

[17] M. Renzi, F. Patuzzi, and M. Baratieri, “Syngas feed of micro gas turbines with steam injection: Effects on performance, combustion and pollutants formation,” *Applied Energy*, vol. 206, pp. 697–707, Nov. 2017.

[18] J. Duan, L. Sun, G. Wang, and F. Wu, “Nonlinear modeling of regenerative cycle micro gas turbine,” *Energy*, vol. 91, pp. 168–175, Nov. 2015.

[19] P. Pilavachi, “Mini- and micro-gas turbines for combined heat and power,” *Applied Thermal Engineering*, vol. 22, pp. 2003–2014, Dec. 2002.

[20] “Mitis website.” `https://www.mitis.be/#technology`. Accessed: 2021-05-21.

[21] A. Traverso, “TRANSEO Code for the Dynamic Performance Simulation of Micro Gas Turbine Cycles,” in *Volume 5: Turbo Expo 2005*, (Reno, Nevada, USA), pp. 45–54, ASMEDC, Jan. 2005.

[22] P. Eguia, I. Zamora, E. Torres, J. San Martín, M. Moya, J. Bruno, and A. Coronas, “Modelling and Simulation of a Microturbine during Transient Events,” *Renewable Energy and Power Quality Journal*, vol. 1, pp. 354–359, Apr. 2010.

[23] Ansaldo Energia S.p.A. Sede Legale e Operativa, “AE-T100 Natural Gas Micro Turbine,” tech. rep., 16152 Genoa - Italy -Via Nicola Lorenzi, 8, 2021. [Online].

[24] M. J. Kim, J. H. Kim, and T. S. Kim, “Program development and simulation of dynamic operation of micro gas turbines,” *Applied Thermal Engineering*, vol. 108, pp. 122–130, Sept. 2016.

[25] T. Zornek, T. Monz, and M. Aigner, “Performance analysis of the micro gas turbine Turbec T100 with a new FLOX-combustion system for low calorific fuels,” *Applied Energy*, vol. 159, pp. 276–284, Dec. 2015.

[26] M. Cristina Cameretti and R. Tuccillo, “Combustion features of a bio-fuelled micro-gas turbine,” *Applied Thermal Engineering*, vol. 89, pp. 280–290, Oct. 2015.

[27] Turbec Spa, “T100 microturbine system, Technical description (T100 Natural Gas) [D14127-03 Technical description Ver 3],” tech. rep., December 2009.

[28] R. Govaerts, “Dynamic model of a micro gas turbine,” Master’s thesis, Vrije Universiteit Brussel, 2015.

[29] R. Calabria, F. Chiariello, P. Massoli, and F. Reale, “CFD Analysis of Turbec T100 Combustor at Part Load by Varying Fuels,” in *Volume 8: Microturbines, Turbochargers and Small Turbomachines; Steam Turbines*, (Montreal, Quebec, Canada), p. V008T23A020, American Society of Mechanical Engineers, June 2015.

[30] G. Comodi, M. Renzi, L. Cioccolanti, F. Caresana, and L. Pelagalli, “Hybrid system with micro gas turbine and PV (photovoltaic) plant: Guidelines for sizing and management strategies,” *Energy*, vol. 89, pp. 226–235, Sept. 2015.

[31] C. F. McDonald, “Recuperator considerations for future higher efficiency microturbines,” *Applied Thermal Engineering*, vol. 23, pp. 1463–1487, Aug. 2003.

[32] X.-J. Wu, Q. Huang, and X.-J. Zhu, “Thermal modeling of a solid oxide fuel cell and micro gas turbine hybrid power system based on modified LS-SVM,” *International Journal of Hydrogen Energy*, vol. 36, pp. 885–892, Jan. 2011.

[33] M. Mahmood, A. Martini, A. F. Massardo, and W. De Paepe, “Model Based Diagnostics of AE-T100 Micro Humid Air Turbine Cycle,” American Society of Mechanical Engineers Digital Collection, Aug. 2018.

[34] P. Stathopoulos and C. O. Paschereit, “Retrofitting micro gas turbines for wet operation. A way to increase operational flexibility in distributed CHP plants,” *Applied Energy*, vol. 154, pp. 438–446, Sept. 2015.

[35] E. Bianchi, “Status of biofuelled Turbec microturbines.” Bio-fuelled Micro Gas Turbines in Europe – Market Opportunities and R&D Requirements, September 2004.

[36] G. Lagerström and M. Xie, “High Performance and Cost Effective Recuperator for Micro-Gas Turbines,” in *Volume 1: Turbo Expo 2002*, (Amsterdam, The Netherlands), pp. 1003–1007, ASMEDC, Jan. 2002.

[37] M. L. Ferrari, M. Pascenti, L. Magistri, and A. F. Massardo, “Micro Gas Turbine Recuperator: Steady-State and Transient Experimental Investigation,” *Journal of Engineering for Gas Turbines and Power*, vol. 132, p. 022301, Feb. 2010.

[38] R. L. Zelenskyi, S. V. Yepifanov, and I. Loboda, “Advanced Nonlinear Modeling of Gas Turbine Dynamics,” in *Aerospace Engineering* (G. Dekoulis, ed.), IntechOpen, Nov. 2019.

[39] H. Asgari, X. Chen, and R. Sainudiin, “Considerations in Modelling and Control of Gas Turbines - a Review,” in *The 2nd International Conference on Control, Instrumentation and Automation*, (Shiraz, Iran), pp. 84–89, IEEE, Dec. 2011.

[40] S. M. Camporeale, B. Fortunato, and M. Mastrovito, “A Modular Code for Real Time Dynamic Simulation of Gas Turbines in Simulink,” *Journal of Engineering for Gas Turbines and Power*, vol. 128, pp. 506–517, July 2006.

[41] G. G. Kulikov and H. A. Thompson, *Dynamic modelling of gas turbines: identification, simulation, condition monitoring and optimal control.* London: Springer, 2010. OCLC: 759803397.

[42] W. I. Rowen, “Simplified Mathematical Representations of Heavy-Duty Gas Turbines,” *Journal of Engineering for Power*, vol. 105, pp. 865–869, Oct. 1983. Publisher: American Society of Mechanical Engineers Digital Collection.

[43] A. Hussain and H. Seifi, “Dynamic Modeling of a Single Shaft Gas Turbine,” *IFAC Proceedings Volumes*, vol. 25, pp. 43–48, Mar. 1992.

[44] F. P. de Mello and D. J. Ahner, “Dynamic models for combined cycle plants in power system studies,” *IEEE Transactions on Power Systems (Institute of Electrical and Electronics Engineers); (United States)*, vol. 9:3, Aug. 1994.

[45] N. Chiras, C. Evans, and D. Rees, “Global Nonlinear Modeling of Gas Turbine Dynamics Using NARMAX Structures,” *Journal of Engineering for Gas Turbines and Power*, vol. 124, pp. 817–826, Oct. 2002.

[46] F. Jurado, “Hammerstein-model-based predictive control of micro-turbines,” *International Journal of Energy Research*, vol. 30, pp. 511–521, June 2006.

[47] W. Blotenberg, “A Model for the Dynamic Simulation of a Two-Shaft Industrial Gas Turbine With Dry Low NOx Combustor,” in *Volume 3C: General*, (Cincinnati, Ohio, USA), p. V03CT17A016, American Society of Mechanical Engineers, May 1993.

[48] R. Bettocchi, P. R. Spina, and F. Fabbri, “Dynamic Modeling of Single-Shaft Industrial Gas Turbine,” in *Volume 4: Heat Transfer; Electric Power; Industrial and Cogeneration*, (Birmingham, UK), p. V004T11A007, American Society of Mechanical Engineers, June 1996.

[49] P. Ailer, I. Sánta, G. Szederkényi, and K. Hangos, “Nonlinear model-building of a low-power gas turbine,” *Periodica Polytechnica Series Transportation Engineering*, vol. 29, Jan. 2001.

[50] P. Ailer, G. Szederkényi, and K. Hangos, “MODEL-BASED NONLINEAR CONTROL OF A LOW-POWER GAS TURBINE,” *IFAC Proceedings Volumes*, vol. 35, no. 1, pp. 375–380, 2002.

[51] S. M. Camporeale, B. Fortunato, and A. Dumas, “Dynamic modelling of recuperative gas turbines,” *Proceedings of the Institution of Mechanical Engineers, Part A: Journal of Power and Energy*, vol. 214, pp. 213–225, May 2000.

[52] N. Hadroug, A. Hafaifa, A. Kouzou, and A. Chaibet, “Dynamic model linearization of two shafts gas turbine via their input/output data around the equilibrium points,” *Energy*, vol. 120, pp. 488–497, Feb. 2017.

[53] A. Mehrpanahi, G. Payganeh, and M. Arbabtafti, “Linear Transfer Functions Extraction for a Power Generation Three-Shaft Gas Turbine Based on Actual Specifications,” *Proceedings of the Institution of Mechanical Engineers, Part C: Journal of Mechanical Engineering Science*, vol. 234, pp. 2781–2802, July 2020.

[54] M. Pakmehr, N. Fitzgerald, E. Feron, J. Paduano, and A. Behbahani, “Physics-Based Dynamic Modeling of a Turboshaft Engine Driving a Variable Pitch Propeller,” *Journal of Propulsion and Power*, vol. 32, pp. 646–658, May 2016.

[55] S. Bracco and F. Delfino, “A mathematical model for the dynamic simulation of low size cogeneration gas turbines within smart microgrids,” *Energy*, vol. 119, pp. 710–723, Jan. 2017.

[56] A. Cagnano and E. De Tuglie, “On-line identification of simplified dynamic models: Simulations and experimental tests on the Capstone C30 microturbine,” *Electric Power Systems Research*, vol. 157, pp. 145–156, Apr. 2018.

[57] I. Yazar, E. Kiyak, F. Caliskan, and T. H. Karakoc, “Simulation-based dynamic model and speed controller design of a small-scale turbojet engine,” *Aircraft Engineering and Aerospace Technology*, vol. 90, pp. 351–358, Mar. 2018.

[58] F. Delattin, S. Bram, S. Knoops, and J. De Ruyck, “Effects of steam injection on microturbine efficiency and performance,” *Energy*, vol. 33, pp. 241–247, Feb. 2008.

[59] W. De Paepe, F. Delattin, S. Bram, and J. De Ruyck, “Steam injection experiments in a microturbine – A thermodynamic performance analysis,” *Applied Energy*, vol. 97, pp. 569–576, Sept. 2012.

[60] E. Tsoutsanis, N. Meskin, M. Benammar, and K. Khorasani, “A component map tuning method for performance prediction and diagnostics of gas turbine compressors,” *Applied Energy*, vol. 135, pp. 572–585, Dec. 2014.

[61] G. A. Misté and E. Benini, “Turbojet Engine Performance Tuning With a New Map Adaptation Concept,” *Journal of Engineering for Gas Turbines and Power*, vol. 136, p. 071202, July 2014.

[62] K. Gharaibeh and A. W. Costall, “A Flow and Loading Coefficient-Based Compressor Map Interpolation Technique for Improved Accuracy of Turbocharged Engine Simulations,” SAE Technical Paper 2017-24-0023, SAE International, Warrendale, PA, Sept. 2017. ISSN: 0148-7191, 2688-3627.

[63] Q. Yang, S. Li, and Y. Cao, “A new component map generation method for gas turbine adaptation performance simulation,” *Journal of Mechanical Science and Technology*, vol. 31, pp. 1947–1957, Apr. 2017.

[64] E. Tsoutsanis, N. Meskin, M. Benammar, and K. Khorasani, “Transient Gas Turbine Performance Diagnostics Through Nonlinear Adaptation of Compressor and Turbine Maps,” *Journal of Engineering for Gas Turbines and Power*, vol. 137, p. 091201, Sept. 2015.

[65] J. Kurzke, “How to Get Component Maps for Aircraft Gas Turbine Performance Calculations,” American Society of Mechanical Engineers Digital Collection, June 1996.

[66] G. A. Misté and E. Benini, “Improvements in Off Design Aeroengine Performance Prediction Using Analytic Compressor Map Interpolation,” *Int. J. Turbo Jet-Engines*, vol. 29, Jan. 2012.

[67] G. Jones, P. Pilidis, and B. Curnock, “Extrapolation of Compressor Characteristics to the Low-Speed Region for Sub-Idle Performance Modelling,” in *Volume 2: Turbo Expo 2002, Parts A and B*, (Amsterdam, The Netherlands), pp. 861–867, ASMEDC, Jan. 2002.

[68] C. Kong, J. Ki, and M. Kang, “A New Scaling Method for Component Maps of Gas Turbine Using System Identification,” *Journal of Engineering for Gas Turbines and Power*, vol. 125, pp. 979–985, Nov. 2003.

[69] Y. G. Li, P. Pilidis, and M. A. Newby, "An Adaptation Approach for Gas Turbine Design-Point Performance Simulation," *Journal of Engineering for Gas Turbines and Power*, vol. 128, pp. 789–795, Sept. 2005.

[70] F. K. Moore and E. M. Greitzer, "A Theory of Post-Stall Transients in Axial Compression Systems: Part I—Development of Equations," *Journal of Engineering for Gas Turbines and Power*, vol. 108, pp. 68–76, Jan. 1986.

[71] C. Drummond and C. R. Davison, "Improved Compressor Maps Using Approximate Solutions to the Moore-Greitzer Model," in *Volume 1: Aircraft Engine; Ceramics; Coal, Biomass and Alternative Fuels; Controls, Diagnostics and Instrumentation; Education; Electric Power; Awards and Honors*, (Orlando, Florida, USA), pp. 187–195, ASMEDC, Jan. 2009.

[72] H. Tu and H. Chen, "Modeling of a Compressor's Performance Map by Fitting Function Methodology," *Advanced Materials Research*, vol. 779-780, pp. 1194–1198, Sept. 2013.

[73] Y. Yu, L. Chen, F. Sun, and C. Wu, "Neural-network based analysis and prediction of a compressor's characteristic performance map," *Applied Energy*, vol. 84, pp. 48–55, Jan. 2007.

[74] K. Ghorbanian and M. Gholamrezaei, "An artificial neural network approach to compressor performance prediction," *Applied Energy*, vol. 86, pp. 1210–1221, July 2009.

[75] A. Rohatgi, "Webplotdigitizer: Version 4.4," 2020.

[76] P. Virtanen, R. Gommers, T. E. Oliphant, M. Haberland, T. Reddy, D. Cournapeau, E. Burovski, P. Peterson, W. Weckesser, J. Bright, S. J. van der Walt, M. Brett, J. Wilson, K. J. Millman, N. Mayorov, A. R. J. Nelson, E. Jones, R. Kern, E. Larson, C. J. Carey, İ. Polat, Y. Feng, E. W. Moore, J. VanderPlas, D. Laxalde, J. Perktold, R. Cimrman, I. Henriksen, E. A. Quintero, C. R. Harris, A. M. Archibald, A. H. Ribeiro, F. Pedregosa, P. van Mulbregt, and SciPy 1.0 Contributors, "SciPy 1.0: Fundamental Algorithms for Scientific Computing in Python," *Nature Methods*, vol. 17, pp. 261–272, 2020.

[77] "Caleb Bell and Contributors (2016-2021). Thermo: Chemical properties component of Chemical Engineering Design Library (ChEDL)." `https://github.com/CalebBell/thermo`.

[78] I. H. Bell, J. Wronski, S. Quoilin, and V. Lemort, "Pure and Pseudo-pure Fluid Thermophysical Property Evaluation and the Open-Source Thermophysical Property Library CoolProp," *Industrial & Engineering Chemistry Research*, vol. 53, no. 6, pp. 2498–2508, 2014.

[79] F. Alobaid, N. Mertens, R. Starkloff, T. Lanz, C. Heinze, and B. Epple, "Progress in dynamic simulation of thermal power plants," *Progress in Energy and Combustion Science*, vol. 59, pp. 79–162, Mar. 2017.

[80] "Software Release of the SimuPy Flight Vehicle Toolkit (NASA website)." `https://www.nasa.gov/feature/software-release-of-the-simupy-flight-vehicle-toolkit`, November 2020. Accessed: 2021-05-21.

[81] B. W. L. Margolis, "SimuPy: A Python framework for modeling and simulating dynamical systems," *The Journal of Open Source Software*, vol. 2, p. 396, Sept. 2017.

[82] A. Mehrpanahi, G. Payganeh, and M. Arbabtafti, “Dynamic modeling of an industrial gas turbine in loading and unloading conditions using a gray box method,” *Energy*, vol. 120, pp. 1012–1024, Feb. 2017.

[83] M. Hohloch, J. Zanger, A. Widenhorn, and M. Aigner, “Experimental Characterization of a Micro Gas Turbine Test Rig,” in *Volume 3: Controls, Diagnostics and Instrumentation; Cycle Innovations; Marine*, (Glasgow, UK), pp. 671–681, ASMEDC, Oct. 2010.

[84] I. V. Novosselov and P. C. Malte, “Development and Application of an Eight-Step Global Mechanism for CFD and CRN Simulations of Lean-Premixed Combustors,” in *Volume 2: Turbo Expo 2007*, (Montreal, Canada), pp. 769–779, ASMEDC, Jan. 2007.

[85] A. L. London, F. R. Biancardi, and J. W. Mitchell, “The Transient Response of Gas-Turbine-Plant Heat Exchangers—Regenerators, Intercoolers, Precoolers, and Ducting,” *Journal of Engineering for Power*, vol. 81, pp. 433–448, Oct. 1959.

[86] A. L. London, D. F. Sampsell, and J. G. McGowan, “The Transient Response of Gas Turbine Plant Heat Exchangers—Additional Solutions for Regenerators of the Periodic-Flow and Direct-Transfer Types,” *Journal of Engineering for Power*, vol. 86, pp. 127–135, Apr. 1964.

[87] M. L. Ferrari, A. Sorce, M. Pascenti, and A. F. Massardo, “Recuperator dynamic performance: Experimental investigation with a microgas turbine test rig,” *Applied Energy*, vol. 88, pp. 5090–5096, Dec. 2011.

[88] M. Duponcheel, G. Winckelmans, and P. Billuart, “LMECA 2322 - Heat Exchangers.” 2019.

[89] S. Quoilin, R. Aumann, A. Grill, A. Schuster, V. Lemort, and H. Spliethoff, “Dynamic modeling and optimal control strategy of waste heat recovery Organic Rankine Cycles,” *Applied Energy*, vol. 88, pp. 2183–2190, June 2011.

[90] J. H. Kim, T. S. Kim, and S. J. Moon, “Development of a program for transient behavior simulation of heavy-duty gas turbines,” *Journal of Mechanical Science and Technology*, vol. 30, pp. 5817–5828, Dec. 2016.

[91] K. Hubin, “Stoominjectie bij de microturbine,” Master’s thesis, Vrije Universiteit Brussel, 2008.

[92] T. He, D. Li, Y. Xue, and J. Wang, “START UP AND SHUT DOWN SIMULATION OF MICRO GAS TURBINE BASED ON REINFORCEMENT LEARNING,” p. 4, 2019.

[93] J. Zanger, A. Widenhorn, and M. Aigner, “Experimental Investigations of Pressure Losses on the Performance of a Micro Gas Turbine System,” *Journal of Engineering for Gas Turbines and Power*, vol. 133, p. 082302, Aug. 2011.

UNIVERSITÉ CATHOLIQUE DE LOUVAIN
École polytechnique de Louvain
Rue Archimède, 1 bte L6.11.01, 1348 Louvain-la-Neuve, Belgique | **www.uclouvain.be/epl**